DEVELOPMENT OF AN UPPER ARM PHANTOM FOR BP MEASUREMENT

Mayuresh Kulkarni

Supervisor: Dr Tet Chuan Lee

A thesis submitted to Auckland University of Technology in fulfilment of the requirement of the degree of Master of Engineering

July 2021

School of Engineering

Faculty of Design and Creative Technologies

Auckland University of Technology

Acknowledgement

I want to thank my supervisors, Dr Tet Chuan Lee and Dr Andrew Lowe, for their incessant guidance and support. Their technical expertise, patience, and encouragement motivated me to take up new challenges during the course of this study.

My sincere gratitude to Dr Andrew Lowe for giving me an opportunity to work on this project and be a part of IBTec. His knowledge and humility always inspire me to do better.

I would like to thank my fellow teammate Liam Foley for his assistance in fabricating the phantom test rig. The analytical formulations of the axisymmetric models found in this thesis are derived by Dr Tet Chuan Lee.

I appreciate Parn Jones, Ekta Dahiya, Ragavan Subburaj and everyone at IBTec for enriching this learning experience.

Abstract

Cardiovascular diseases, such as hypertension, is one of the most commonly occurring afflictions throughout the world. Blood pressure (BP) measurement is critical in the diagnostic analysis of cardiovascular health. The cuff-based non-invasive blood pressure (NIBP) measurement devices are marked by inaccuracies in the estimation of BP, attributing to assumptions related to upper arm's geometry, soft tissue mechanical properties, and distribution of uniform cuff pressure (CP).

The research aims to develop upper arm numerical models and a physical phantom to investigate the displacements, stresses, volume changes on the upper arm soft tissue during NIBP measurement. The characterisation of these quantities aids in understanding the cause of BP estimation errors in NIBP measurement devices. Annular concentric finite element (FE) models were developed and verified using the principles of continuum mechanics.

An upper arm model of anatomically accurate geometry was developed. A range of silicone materials was characterised for their mechanical properties to formulate a hyperelastic constitutive model for Finite Element Analysis (FEA) of the upper arm BP simulation. The characterisation aided in selecting the appropriate material to fabricate the anatomical upper arm phantom. A test rig was built for the arm phantom to obtain pressure-volume relationship of the soft tissue components during NIBP measurement. The anatomically accurate FE model was validated with the upper arm phantom for the pressure-volume relationship. The displacement, strain effects of the tissue contact conditions on the soft tissue during NIBP were analysed. It was concluded that the tissue mechanical properties, geometry, and tissue contact conditions of the upper arm plays a crucial role in estimation of BP using NIBP measurement devices.

Table of Contents

List of Figures

List of Tables

Statement of Authorship

“I hereby declare that this submission is my own work and that, to the best of my knowledge and belief, it contains no material previously published or written by another person nor material which to a substantial extent has been accepted for the qualification of any other degree or diploma of a university or other institution of higher learning, except where due acknowledgement is made in the acknowledgements.”

Mayuresh Kulkarni

Signature:

Chapter 1 Introduction

1.1 Background

Blood pressure (BP) is the measure of the pressure exerted by blood on the wall of the arteries present in the human body. During a cardiac cycle, the minimum pressure exerted by blood on arteries is termed Diastolic pressure (DP). The maximum pressure exerted by the blood upon ventricular contraction during a cardiac cycle is termed Systolic pressure (SP). The dynamics of the human body is such that the BP varies at different locations throughout the body. However, in typical clinical diagnosis and treatment, BP refers to the pressure exerted by blood on the brachial artery in the upper arm. The normal SP and DP in a young adult are found to be 120 mmHg and 80 mmHg, respectively (Khurana, 2014). Blood pressures exceeding these normal values are termed as high BP.

1.2 BP measurement

Since BP stands out to be an influential and independent risk factor in assessing cardiovascular diseases (Pickering Tg Fau - Hall et al., 2005), its accurate measurement is critical in clinical diagnosis. In a systematic review of 74 studies comprising of 3073 participants, it was found that only 33% of systolic BP measurements were accurate within 5 mmHg, 59% were accurate within 10 mmHg, and 74% were accurate within 15 mmHg (Picone et al., 2017). American Heart Association classifies BP and corresponding diagnosis in four categories: normal, elevated, stage 1 hypertension, and stage 2 hypertension (Whelton Pk Fau - Carey et al., 2017). The classification is summarised in Table 1.

In the United States alone, inaccuracy of 5 mmHg in BP measurement is gauged to misclassify the BP of 48 million people every year (Picone et al., 2017). An overestimation of DP by 5 mmHg is estimated to double the number of patients diagnosed with hypertension. Similarly, due to underestimation of the BP and subsequent missed diagnosis, the patients do not receive the necessary treatment (Jones et al., 2003). It is estimated that this incorrect diagnosis leading to overtreatment and under-treatment heighten the risk of cardiac arrests and death (Robles et al., 2019). The methods with which the BP is measured vary in accuracy. The BP can be measured invasively and non-invasively.

BP classification	SP (mmHg)	and/or	DP (mmHg)
Normal	<120	and	<80
Elevated	120 – 129	and	<80
Stage 1 hypertension (high BP)	130 – 139	or	80 – 89
Stage 2 hypertension (high BP)	≥140	or	≥90

Table 1 Classification of BP (Whelton Pk Fau - Carey et al., 2017)

1.2.1 Invasive BP measurement

The most accurate form of BP measurement involves the use of catheters (Kesteloot H Fau - Van Houte & Van Houte, 1973). The catheter incorporates a high fidelity pressure transducer connected to a disposable tube inserted in the artery and is thus subjected to the bloodstream. Even though this type of BP measurement has high associated risks, it is commonly regarded as the most accurate.

1.2.2 Non-invasive BP (NIBP) measurement

Auscultatory method incorporating a mercury sphygmomanometer is historically accepted as the gold standard for measuring BP non-invasively (Henry Black, 2012). It involves inflation of a cuff wrapped around the upper arm to a supra-systolic condition leading to occlusion of the brachial artery. The air pressure in the cuff is slowly released. A sound is detected with the help of a stethoscope placed superficially over the brachial artery that determines SP and DP. This determination is according to the five phases of Korotkoff sounds (Douglas Mann, 2014). The accuracy of this method depends on the size of the cuff employed. Studies have demonstrated that soft tissue stiffness affects the BP measurement using this method (Frech et al., 2012) (Blank et al., 2018). The schematic representation of the auscultatory NIBP measurement method is illustrated in Figure 1.

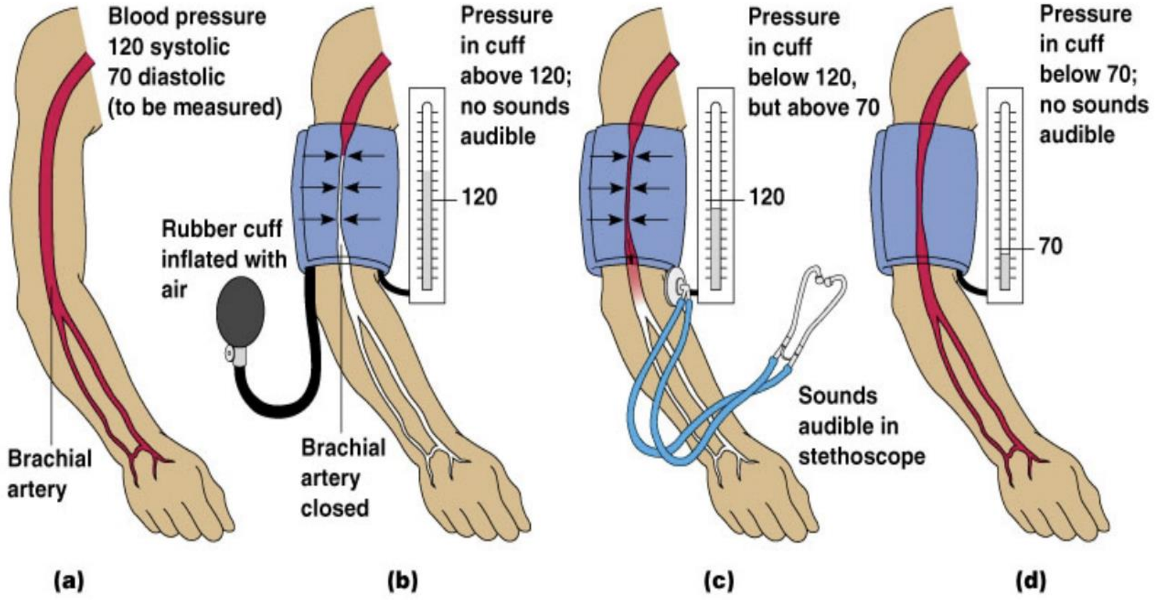

Figure 1 Auscultatory NIBP measurement procedure (Marieb & Keller, 2017).

The oscillometric method is another NIBP measurement technique widely used in automated BP monitors, exhibiting minimal errors. The process of measuring the BP is similar to that of the auscultatory method. A cuff wrapped around the upper arm is inflated to pressure above the SP, resulting in occlusion of the brachial artery. It is then deflated at a controlled rate allowing blood to flow. During the measurement process, the cuff pressure (CP) is monitored and recorded by the measuring device. As blood starts to flow through the brachial artery, the pressure oscillations in the cuff increase gradually until a maximum amplitude near the mean pressure (MP) is attained and then declines towards the end of the measurement. Manufacturer-developed algorithms are used to calculate the SP and DP (Lewis et al., 2019). Automated oscillometric NIBP measurement devices differ in their algorithms, transducers, inflation-deflation rates, cuff sizes, all of which affects the estimation of BP. Apart from the device-related inconsistencies, the method does not compensate for the variations related to the upper arm's geometry and soft tissue properties among individuals (Van Montfrans, 2001). Nevertheless, oscillometric NIBP devices are widely used since operating them does not require expert training, and it facilitates in obtaining reasonable accuracy of BP. A schematic diagram of the oscillometric NIBP measurement procedure is illustrated in Figure 2

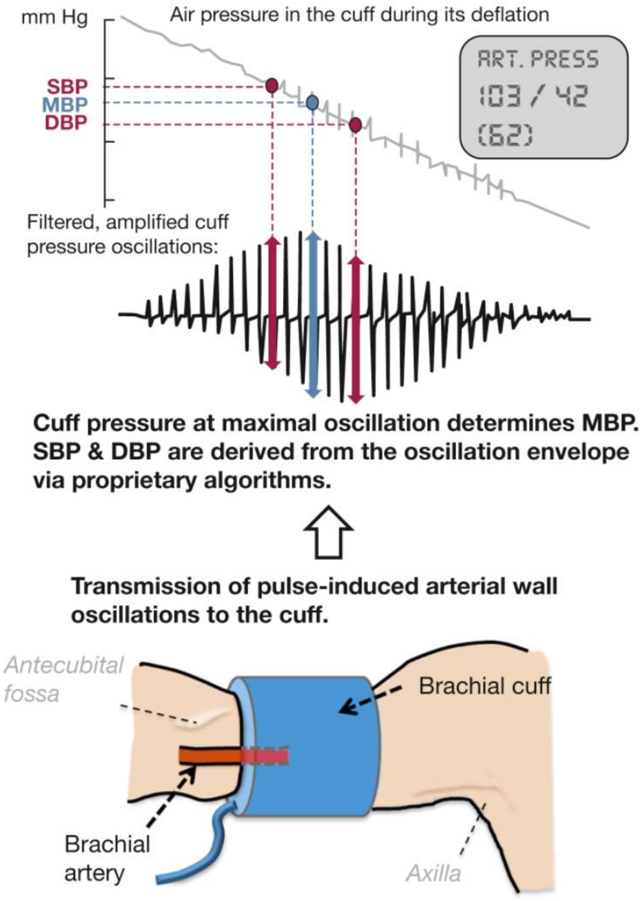

Figure 2 Oscillometric NIBP measurement procedure (Lakhal et al., 2018).

1.3 Aim

The thesis aims to investigate the factors that affect the accuracy of NIBP measurement. The primary investigation area is the effects of the upper arm geometry and the mechanical properties of soft tissues on NIBP measurement. The relationship between cuff pressure (CP), blood pressure (BP) and the resultant displacement on the soft tissue is investigated.

1.4 Overview

A summary of the chapters found in this thesis:

- Chapter 1: Introduction to the BP, popular NIBP measurement methods and motivation of the study.

- Chapter 2: Review of the design requisites and processes to develop upper arm computational and experimental models from the available literature.
- Chapter 3: Numerical formulation of the annular concentric models.
- Chapter 4: Development and verification of finite element models using the concentric analytical models
- Chapter 5: Material testing and characterisation for upper arm phantom fabrication and anatomical finite element model.
- Chapter 6: Design and development of the anatomical geometry. This chapter describes the process of phantom fabrication and testing.
- Chapter 7: Discusses the anatomical model in FEA. Validation of the results obtained from the phantom experimental investigation.
- Chapter 8: Conclusion and future work of the study.

1.5 Scope

The ambit of this project is to study the effects of CP and BP on soft tissues and the brachial artery in the human upper arm using computational models, analytical methods, and experimental investigation.

Chapter 2 Literature Review

As mentioned above, the NIBP measurement methods exhibit undesirable errors in the measurement. The errors result from gross assumptions related to the upper arm geometry and soft tissue mechanical properties, which vary widely amongst individuals (Palatini & Asmar, 2018). The effects of the upper arm geometry and soft tissue mechanical properties during NIBP measurement are investigated with the aid of computational upper arm models and experimental phantom. The computational upper arm models are numerical simulations that emulate the BP measurement process. The aspects of the BP measurement simulation, such as the upper arm geometry, soft tissue mechanical properties, boundary conditions, are elaborated in the following sections. The experimental phantom is the emulation of the BP measurement process in an in vitro setting. The potential methods to fabricate the upper arm phantom using soft-tissue mimicking materials are discussed in the following sections.

2.1 Upper arm

The human body is thoroughly composed of soft tissues. The upper arm is a combination of soft tissues that include skin, muscles, subcutaneous adipose tissue (SAT), fascia, cartilage ligaments that exhibit biomechanical properties (Lan et al., 2011). These soft tissues are supported by the human arm's longest and largest bone, called the humerus. Figure 3 illustrates the anterior view of the upper arm. Ursino and Cristalli (1996) studied the biomechanical factors affecting the BP measurement using some mathematical models. The diameter of the upper arm in this study was assumed to be 104 mm, and the diameter of the humeral head was assumed to be 42 mm. In another study, the shaft of the humerus bone in adults was reported to be 19.7 mm (Spross et al.,

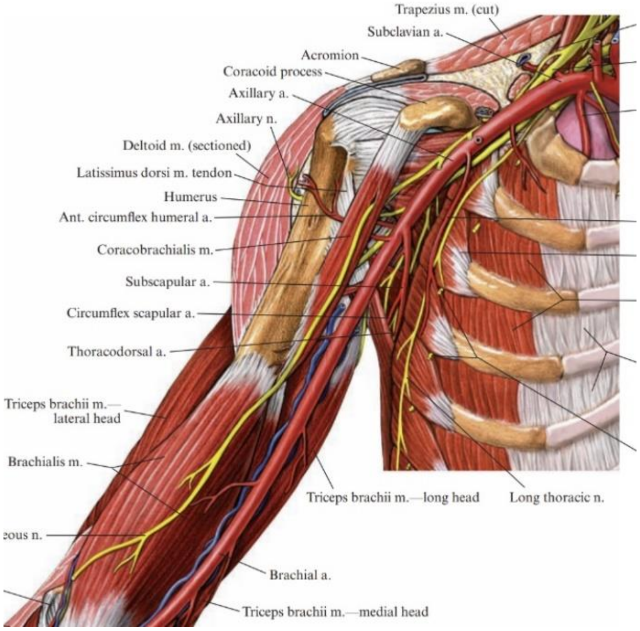

Figure 3 Anterior view of the upper arm (Teaford, 2009)

2015). Bonso et al. (2010) studied the upper arm characteristics of 142 subjects for testing the accuracy of conical cuffs for BP measurement. The mean length of the upper arm was reported to be 223 mm. Uniform with the other bones in the human body, the fundamental function of the humerus is to offer structural support and strength to the upper limb (Mendoza-Muñoz et al., 2017).

The humerus bone is surrounded by a layer of fibrous periosteum which operates as a connecting tissue for ligaments and tendons that binds the humerus and the surrounding muscles (Dwek, 2010). The major muscle groups in the upper arm region are biceps brachii (anterior) and triceps brachii (posterior). Adipose, a loose connective tissue made up of fat, encompasses these muscle groups (Nayak et al., 2008). The upper extremity's most superficial layer is the skin composed of three heterogeneous layers: epidermis, dermis, and hypodermis (Pailler-Mattei et al., 2008). The epidermis is the outer layer of skin, and its function is to protect against dehydration, mechanical stress, and infections, along with acting as a sensory mechanism (Sotiropoulou & Blanpain, 2012). Underlying the epidermis layer is the dermis layer that provides elasticity to the skin and shields the body from stress and strain. Beneath the dermis layer is the hypodermis layer, which

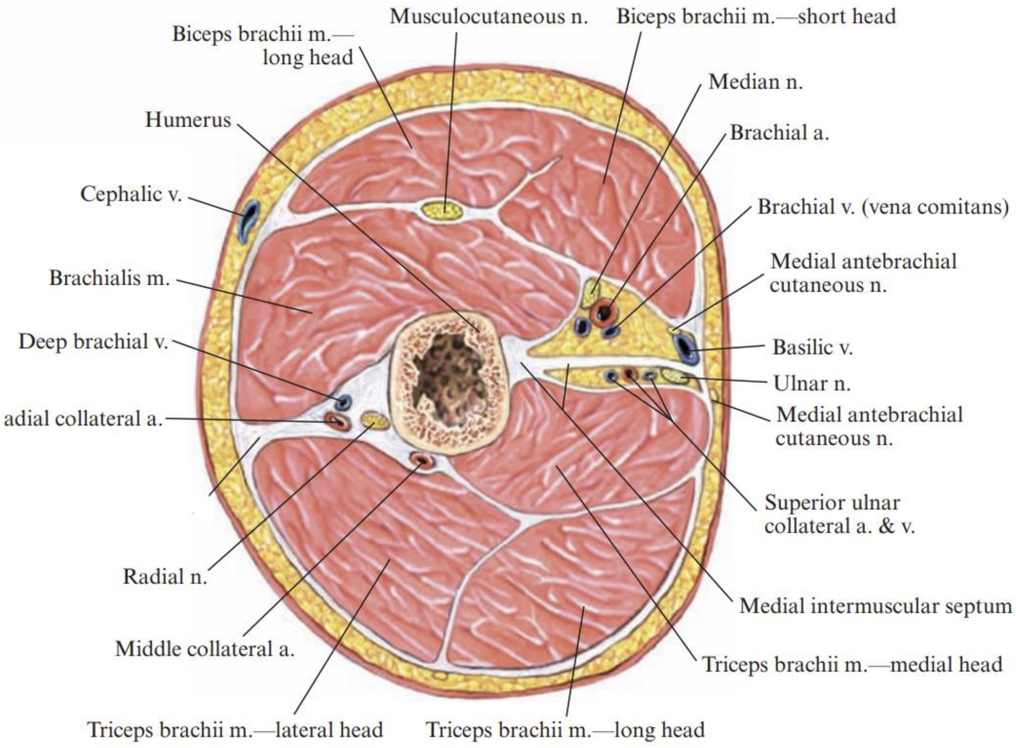

Figure 4 Cross-sectional view of the upper arm (Teaford, 2009).

connects the skin and muscles, absorbs shock from impact on the skin, and acts as a storage for energy (Dąbrowska et al., 2016). The hypodermis is the thickest layer of the skin and is integrated with the arm's adipose tissue surrounding the brachial artery and surrounding veins. Figure 4 illustrates the cross-sectional view of the upper arm.

2.1.1 Brachial artery

The brachial artery is a fundamental blood vessel in the upper arm medial to the humerus bone at the proximal end. It curves anteriorly to the humerus till the midway of the arm (Standring, 2015). It then runs parallel to the humerus and bicep tendon until it reaches the distal end of the arm, which is the cubital fossa. Upon reaching the elbow, the brachial artery is subdivided into two branches: the ulnar artery and the radial artery (Kulkarni, 2007). The arterial wall is composed of well-organised connective tissues that are composed of cells and matrix fibres. Arterial walls are structured with three layers: the intima, media, and adventitia. The composition of these connective tissues is illustrated in Figure 5. The brachial artery region is the most common area for non-invasive blood measurement because the pulse can be felt through the upper arm and its location relative to the heart (Drzewiecki & Pilla, 1998). The brachial artery's arterial wall mechanical properties depend on pulse wave velocity, descending pressure, compliance, distensibility, and other factors. The brachial artery is approximately 3 to 4 mm in diameter in normal conditions for healthy adults (Picone et al., 2015). In a study carried

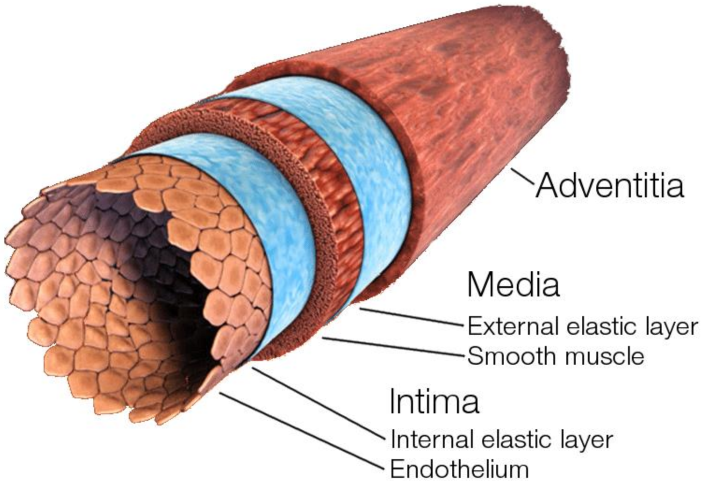

Figure 5 Composition of the brachial artery (Závodszky, 2015).

out by Dammers et al. (2015), the mean diameter of the brachial artery among 16 patients was found to be 4.4 mm, and the thickness of their brachial artery was reported 0.4 mm. Few studies have reported the location of the brachial artery from the surface of the arm. The depth of the brachial artery with respect to the surface of the upper arm was investigated with the acquisition of computational phantoms developed by the ITIS foundation (Hasgall et al., 2018). The methodology of the analysis is as follows:

1) Three anatomical models (Virtual population) were obtained from the ITIS Foundation and imported into Sim4life.

2) The individual models were sliced at three different sections of the upper arm – distal, middle, and proximal. Figure 6 illustrates the cross-sectional view of the computational phantom sliced at the middle of the upper arm.

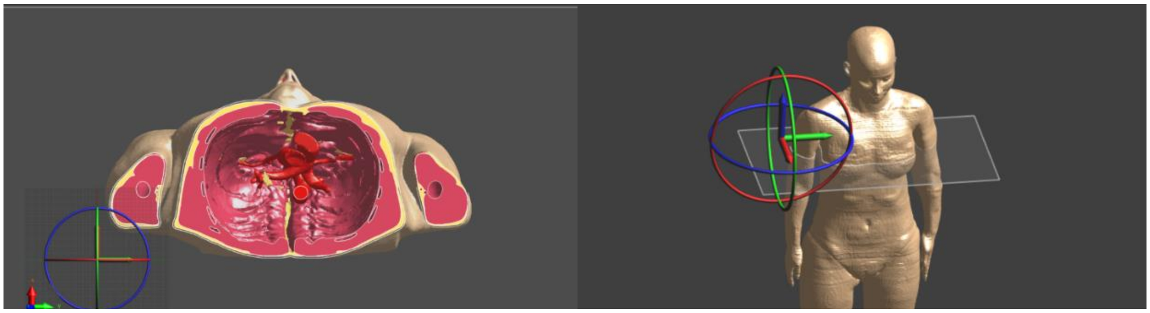

Figure 6 Cross-sectional view sliced at the mid upper arm of the computational phantom (Hasgall et al., 2018).

3) Each slice was composed of brachial artery, muscles, SAT, humerus bone and skin tissues. Figure 7 illustrates the various tissue layers of the phantom.

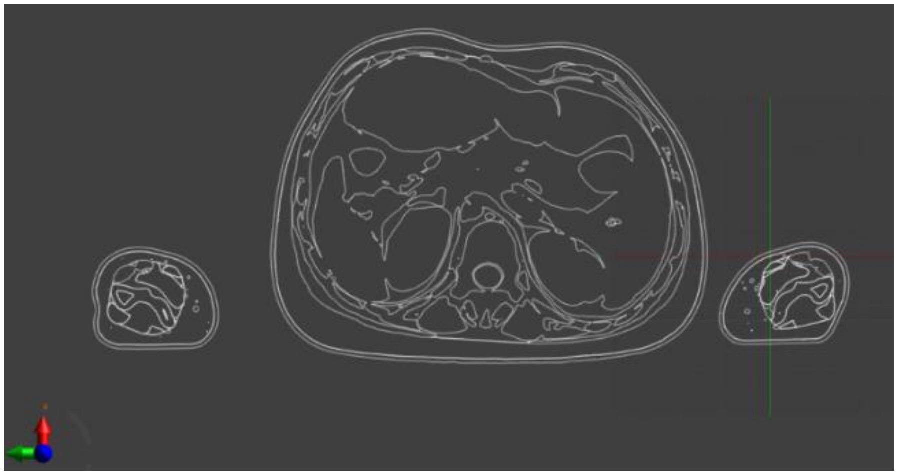

Figure 7 Cross-sectional view of the tissue layers (Hasgall et al., 2018).

4) A new coordinate system was created at the vertex of the brachial artery closest to the skin tissue surface, and the ‘distance’ measurement tool from Sim4life was used to take the measurements at each slice. The vertical distance across the X-axis was measured. The measurement procedure is exemplified in Figure 8.

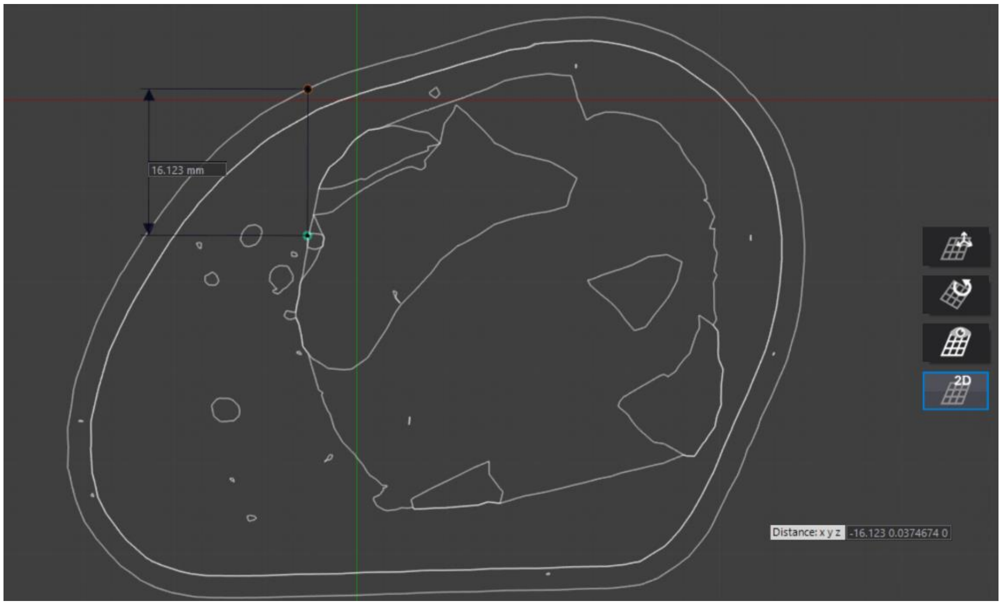

Figure 8 Measurement of the distance of the brachial artery from the skin surface

Each slice was sectioned at a distance of 75 mm from the other. The measurements can be summarised in Table 1 below:

Anatomical Model	**Slice cross-section** (Measured from the lowest point below the fibula)	**Depth of brachial artery (mm)**	
		Left brachial	**Right brachial**
Sex: Female			
Age: 26	Distal: 1190 mm	17.355	16.123
Height: 1.52 m	Middle: 1265 mm	28.382	30.084
Weight: 54.6 kg	Proximal: 1340 mm	38.754	36.117
BMI:23.6			
Sex: Male			
Age: 34	Distal: 1240 mm	34.833	34.467
Height: 1.77 m	Middle: 1315 mm	47.472	45.614
Weight: 70.2 kg	Proximal: 1390 mm	51.869	54.002
BMI:22.4			
Sex: Female			
Age: 26	Distal: 1140 mm	23.935	27.571
Height: 1.63 m	Middle: 1215 mm	32.710	30.969
Weight: 57.3 kg	Proximal: 1290 mm	43.089	38.428
BMI:21.6			
Sex: Male			
Age: 33	Distal: 1210 mm	32.481	32.109
Height: 1.62 m	Middle: 1285 mm	45.067	44.792
Weight: 64.3 kg	Proximal: 1360 mm	50.235	52.341
BMI:24.5			

Table 2 Location of the brachial artery from the surface of the upper arm

2.1.2 Parameters of the upper arm

The anthropometric parameters of the upper arm from the literature mentioned in the sections above are summarised in Table 3.

Parameter	Value(s) (mm)	Reference
Diameter of the humerus bone	19-24	(Ursino and Cristalli 1994), (Spross et al., 2015)
Length of the upper arm	205-260	(Bonso et al., 2010), (Deng & Liang, 2016)
Diameter of the arm	63-127	(Ursino and Cristalli, 1996)
Diameter of the brachial artery	3.7-5.1	(Dammers, Hoeks et al. 2005)
The thickness of the brachial artery	0.335-0.460	(Dammers, Hoeks et al. 2005)
Depth of the artery	Distal Male: 33.472 Distal Female:19.746 Mid Male:46.543 Mid Female:30.536 Proximal Male:52.111 Proximal female:39.097	(Hasgall et al., 2018)

Table 3 Parameters of the upper arm

2.2 Finite Element Analysis

Finite element analysis (FEA) is one of the most comprehensive methods used in engineering analysis, problem-solving and design optimisation. It is widely used to solve the problems of structural analysis and biomechanical performance of complex biological structures—numerical simulations using FEA aids in analysing the mechanical responses of organs in the domain of biomedical engineering. ANSYS, ABAQUS, NASTRAN, LS-DYNA are some of the commercially available FEA software packages. A typical FEA program follows these model development steps: 1) Geometry construction 2) Assigning material properties to the geometry 3) Model meshing 4) Defining boundary and contact conditions 5) Model loading. These steps are discussed in the following sections pertaining to requisites in the upper arm computational phantom development.

2.2.1 Geometric modelling

Establishing a geometry of the model for FEA is the first step in FEA. The data used to construct an anatomical model can be extensive. In previous studies (Maurel et al., 2002) (Fernandez et al., 2004) (Teran et al., 2005), the data was obtained from Magnetic Resonance Imaging (MRI). MRI images rendered in different scales of grey were used to identify the different tissues and their dimensions (Castleman, 1979). The images or obtained dimensions were used to develop a 3-dimensional (3D) geometry using a computer-aided design (CAD) software package. The created geometry is then imported into an FEA software package.

Visible human project (VHP) is a publicly available MRI dataset of a male and a female cadaver. The MRI data were obtained by slicing, photographing, and digitising a female and male's cadavers at an interval of 1mm (Spitzer & Whitlock, 1998). Figure 9 illustrates a sample image sliced at the middle of the upper arm from the VHP dataset. Since it is

Figure 9 Sample image (No.0417) from the VHP dataset (Spitzer & Whitlock, 1998).

open-sourced, it remains a common source for investigators in the domain of biomedical engineering.

Maurel et al. (2002) reconstructed a biomechanical three dimensional (3D) model of the upper arm from the VHP dataset. The line of force model included mechanical properties for the humerus bone, joints, and muscles. This study aimed to construct a detailed human upper limb animation model to represent the dynamic simulation of complex musculoskeletal systems. It also represented the finite element deformation of soft tissues and muscular contraction.

Teran et al. (2005) developed a 3D framework of skeletal muscles from the VHP dataset and simulated 30 collision-coupled muscles in the upper arm. The material properties assigned to the muscles were transversely isotropic, quasi-incompressible, that incorporated muscle fibre fields with active and passive components. It was concluded that the developed model accurately represented the dynamic deformations in the skeletal muscles acquired the VHP dataset to create finite element volume meshes of the musculoskeletal system and other relevant organs for continuum analysis. It was reported that the organ data from VHP does not represent the original state since the MR images were obtained from a cadaver. The 3D model development from MRI data was reported to be not user friendly. However, the objective of the study was accomplished.

Sim4life is an FEA software package developed by Zurich MedTech that focuses explicitly on anatomical and biological phenomena in the human body with specially developed computable human phantoms. These computable phantoms developed by the IT'IS foundation are a set of detailed high-resolution anatomical models constructed from MRI data of volunteers. The images are processed, segmented, and rendered as rectilinear voxel meshes those forms into a 3D computational phantom (Hasgall et al., 2018). The computational models are developed to work in Sim4life and thus, cannot be exported to any other FEA software package. Figure 10 illustrates a few computational phantoms from Sim4life.

Figure 10 Image of the computational phantoms available from Sim4life (Hasgall et al., 2018).

Zygote (2020) develops anatomically accurate 3D human CAD models for biomedical devices, instrumentation, and FEA. The available 3D CAD anatomy is developed from the MRI and CT scans of 50th percentile individuals (the U.S by height and weight). The model is composed of various tissue layers such as SAT, muscle, and organs. Unlike Sim4life, the model can be readily imported to any FEA software package for further analysis. Figure 11 illustrates the complete 3D anatomical models from Zygote (2020). Figure 12 illustrates the anatomical muscle model from Zygote (2020), with upper arm highlighted in green.

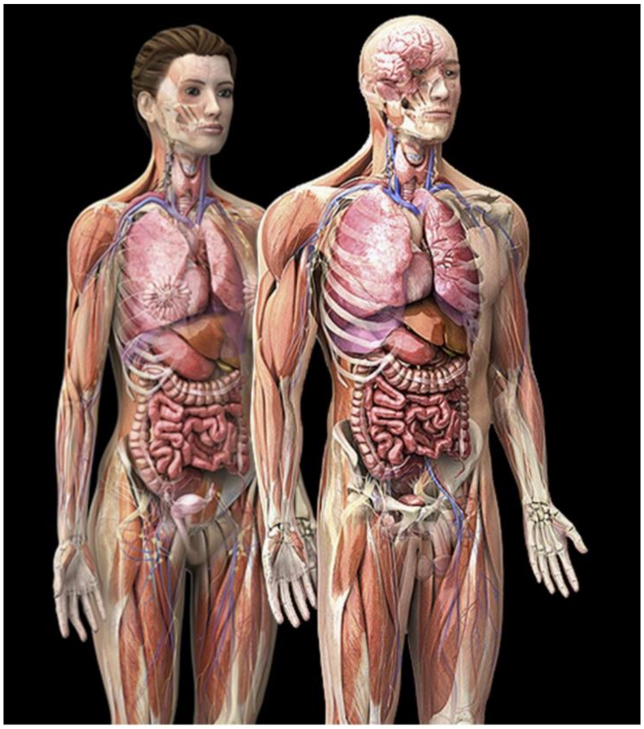

Figure 11 Complete anatomical model available from Zygote (Zygote, 2020).

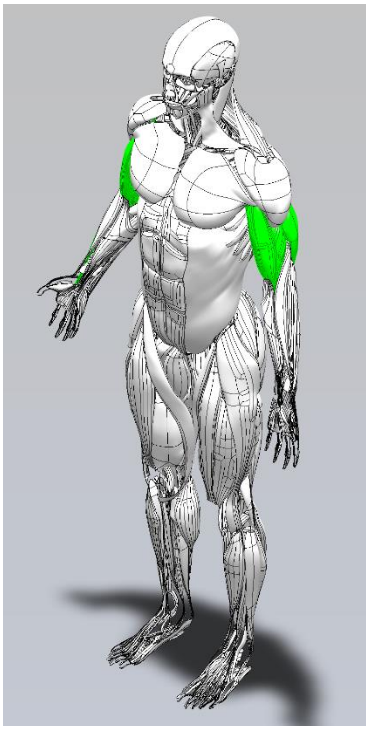

Figure 12 Anatomical muscle model with upper arm highlighted in green colour (Zygote, 2020).

2.2.2 Material modelling

The material property of human tissue is similar to that of a non-linear anisotropic viscoelastic material (Fung, 1993). As mentioned in Section 2.1, the upper arm primarily consists of four types of materials: Subcutaneous Adipose Tissue (SAT) composed of skin and fat, muscles, brachial artery, and the humerus bone. The modulus of elasticity of the bone was found to be in the range of 14099 – 22445 MPa under static loading (Rahmoun et al., 2020). In previous studies (Ursino & Cristalli, 1996) (Heagerty et al., 1993), the humerus bone was assumed rigid because of its high elastic modulus.

SAT is usually considered to be isotropic since it does not have any preferred direction. The elastic modulus of SAT was found to be 44 KPa (Escobar, Wittles et al., 2014). The Poisson's ratio was found to be 0.49, suggesting viscoelasticity (Vannah & Childress, 1993). The muscles are highly fibrous in nature, reflecting their anisotropic properties

(Fung, 1993). The elastic modulus of muscles was reported to be 40 – 100 KPa whereas, the Poisson's ratio was reported 0.45 (Levinson et al., 1995). Clinical experiments have demonstrated that the muscle tissue exhibit linear isotropic properties under 10% strain (Al-Jumaily et al., 2013).

The brachial artery is composed of an intima-media layer and an adventitial layer. Because the fibre directions in these two layers are pretty different, artery material has different properties in the three axes (Fung, 1993), making it an orthotropic material. The elastic modulus of the brachial artery during systole was found to be in the range of 160 KPa – 390 KPa in a previous study (Messas et al., 2013). The mechanical properties of the components of the upper arm for linear and non-linear analyses are summarised in Table 4.

The soft tissues are expected to undergo large deformations due to their highly non-linear nature. In FEA, such a problem is solved as a non-linear analysis using the Newton-Raphson method. In previous investigations, the muscle and skin tissues were formulated using hyperelastic constitutive material models (Sparks et al., 2015), (Mihai et al., 2015). Strain energy density functions define hyperelastic constitutive models. Sparks et al. (2015) investigated the performance of silicone materials to emulate stress distribution in muscle and skin tissues. Ogden 1st order constitutive model was developed from the compression tests of the silicone materials. It was inferred that the formulated constitutive model showed similar indentation type loading, which is exhibited by the soft tissues under compressive loading. Mihai et al. (2015) investigated various hyperelastic constitutive models to simulate SAT and muscle tissues. Based on the experimental evidence of the behaviour of these soft tissues, their mechanical properties such as elastic modulus and shear modulus were characterised. It was reported that the Ogden and Mooney-Rivlin constitutive models were the most accurate to capture the mechanical behaviour of SAT and muscle tissues. Thus, Mooney-Rivlin and Ogden hyperelastic constitutive models are used to simulate soft tissues for non-linear analysis.

However, a linear analysis using isotropic material properties aids in the analytical verification of the FEA model. This simplification of the material model also aids in achieving a balance between accuracy and computational costs.

Component	Linear analysis	Non-linear analysis
	Parameter requisites	**Parameter requisites**
SAT	Elastic modulus = 44 KPa Poisson's ratio = 0.49	Hyperelastic constitutive models: Mooney-Rivlin, Ogden
Muscle	Elastic modulus = 40 – 100 KPa Poisson's ratio = 0.45	Hyperelastic constitutive models: Mooney-Rivlin, Ogden
Brachial artery	Elastic modulus = 160 – 390 KPa Poisson's ratio = 0.45	Hyperelastic constitutive models: Mooney-Rivlin, Ogden
Humerus bone	Elastic modulus = 14 – 22 GPa	Omitted. Applied as a boundary condition

Table 4 Summary of the required mechanical properties of the upper arm components for FEA models

2.2.3 Contact conditions

Johansson et al. (2000) formulated and studied a FE model to simulate the mechanics of muscles in the upper arm. The contact condition between the humerus and muscle of the upper arm was considered to be bonded. The model allowed the simulations of muscle recruitment, determination of stress and strain distributions, and muscle shape prediction. The results of these simulations were verified using the principles of non-continuum mechanics. A similar approach was taken up by Cristalli et al. (1992) to conduct experimental and mathematical research to investigate the NIBP measurement method. There is no relative movement between the humerus bone and the tissues surrounding it. Thus, making the contact condition between them to be bonded. The anatomical arrangement of the brachial artery is such that its top layer is well integrated into the muscles of the upper arm (Fung, 1993). This arrangement leads to the assumption that the contact condition between the artery and muscle is bonded.

2.2.3.1 Sliding element theory of muscle action

The skeletal muscle is composed of muscle fibres. These fibres are arranged in bundles, and the connective tissue fills the voids between them. A layer of fascia surrounds the muscles. The cytoplasm of the fascia is divided into longitudinal threads termed myofibrils. The myofibrils are further split into myofilaments where sliding upon muscle contraction occurs (Fung, 1993). The myofilaments are composed of myosin and actin. The study of actin and myosin movement relative to each other has been of great interest since the 1950s. This phenomenon is also known as the cross-bridge theory. Ishijima et al. (1991) developed a new system for measuring the forces produced by a small number of myosin molecules interacting with a single actin filament. The experimental results concluded that during contraction, the mechanical to chemical coupling ratio between myosin and actin molecules were many to one as opposed to 1:1 without contraction. Various studies (Sutera et al., 1989), (Ma & Zahalak, 1991), (Tözeren, 1985) have verified the occurrence of this sliding through developed mathematical models and experimental investigations.

To conclude, the contact action between muscle and SAT is sliding, inferring the absence of friction.

The contact conditions are summarised in Table 5 below.

Contact group	Contact type
Muscle and humerus bone	Bonded
Brachial artery and muscle	Bonded
SAT and muscle	Frictionless

Table 5 Contact conditions of the tissue layers in the upper arm

2.2.4 Pressure loading conditions

During cuff-based NIBP measurement, the pressures subjected on the upper arm are cuff pressure (CP) on the soft tissue and blood pressure (BP) on the brachial artery. In a previous study, it was reported that the fluid interaction does not affect the NIBP measurement. Fung (1993) reported that the blood flow in the brachial artery is laminar, and the inner surface of the artery is smooth, resulting in negligible friction between the two. Lan et al. (2011) investigated the tissue mechanical properties and their effects on the NIBP measurement. The FE model developed in the study assumed the BP to be uniform along the brachial artery and produced viable results. The distribution of CP was assumed to be uniform across the surface of the upper arm. During NIBP measurement, the CP is increased to a supra systolic pressure up to $30\ \mathrm{mmHg}$. Thus, if the SP is assumed $110\ mmHg$, the CP is $140\ mmHg$.

2.2.5 Discussion

1) The study aims at investigating the effects of the upper arm geometry on NIBP measurement. As mentioned above, various resources are available to develop an upper arm geometry. The VHP dataset has been widely used in previous studies. However, the geometry is specific to one cadaver and does not account for a larger population.
Various computational phantoms are available with the Sim4life software package. The computational models come at a very high cost. Moreover, the computational phantoms cannot be exported to other popular FEA software packages. Learning a new software package entirely can affect the timeline of the project. All these factors reduce the feasibility of using this resource.
The 3D CAD model available from Zygote is developed using MRI scans of a 50th percentile individual (U.S). The model thus accounts for a dataset relevant to the broader population. It is feasible to develop an anatomical model using this dataset since it is available in the form of drawings.

2) Previous studies show that the soft tissues exhibit properties of linear isotropic materials during NIBP measurement, where the strains developed are considerably small. Thus, the assumption of the soft tissues as linear isotropic material is feasible for a primitive analysis. Verification of the simple FEA upper arm models with analytical models is viable for linear deformations. Anatomically, the soft tissues experience large deformations due to their highly non-linear characteristics. It was reported that the non-linear behaviour is accurately captured by Mooney-Rivlin and Ogden hyperelastic constitutive models. These constitutive models are formulated from the stress-strain relationship of the material under various modes of deformation.

3) The interactive conditions between the different components of the upper arm were reviewed. The SAT and muscle layers exhibit a sliding contact between them. This sliding contact is expected to produce different displacements in the soft tissue during cuff-based NIBP measurement.

4) It was reported that there is negligible friction between the blood and the inner surface of the artery. Therefore, the assumption that there is no loss of BP is feasible. It is viable to assume that the BP exerted on the brachial artery is uniform and hydrostatic. The cuff adheres to the upper arm perfectly in an ideal setting such that there is no relative movement between the two. Thus, it is viable to assume that the pressure is exerted on the soft tissue only in the radial direction.

2.3 Arm phantom development

One of the aims of this study is to validate the results obtained from computational phantom simulations with those obtained from the physical phantom experiments. This section reviews the prospective techniques and materials to develop an upper arm phantom.

2.3.1 Lost core casting for arterial phantom

Since the structure of the brachial artery is similar to that of a hollow tube, the lost core casting method suits this application. The inner diameter of the artery is created with a sacrificial male component of the mould, whereas the outer diameter is a resultant of the casting from two female moulds. Since the mould can involve intricate geometries, 3D printing or milling are the most commonly employed methods.

2.3.1.1 Male mould fabrication

Dimensional accuracy and ease of removal are the desired characteristics of a male mould component. Yazdi et al. (2018) critiqued arterial tree phantom development using this method to apply flow measurement. 3D printing using a Poly Vinyl Alcohol (PVA) filament was employed to print the male mould. PVA, being water-soluble, allows for easy removal of the casted component from the mould. Geoghegan et al. (2012) reported that gelatine, chocolate, and wax were vulnerable to shrinking as working materials. Smith et al. (1999) and Hoi et al. (2006) investigated an alloy of low melting point after curing was removed with external heat. Although easily removable, the material left some residue behind, indicating its ineffectiveness when working with intricate geometries.

2.3.1.2 Female mould fabrication

The female mould determines the external geometry of the cast part. It can be designed in a relevant CAD software package and fabricated using additive manufacturing methods like 3D printing. Brunette et al. (2004) used a CNC machine to fabricate female moulds to fabricate a multi-layered coronary artery phantom. The dimensions of the layers were verified using ultrasound imaging. Cao et al. (2013) fabricated male and female moulds using 3D printing and reported the accuracy of the printed moulds within 7 %.

2.3.2 Rotational moulding

Rotational moulding involves pouring working material in a mould mounted on a multi-axial machine that evenly distributes the material as it cures. It is a problematic method to fabricate complex-shaped geometries since the axial speed varies depending on the working material and geometry of the mould.

2.3.3 Dip moulding

This method involves dipping the male mould specimen in the desired material several times. The material is allowed to cure each time it was dipped, ensuring complete coverage and quality control checks. This method requires frequent manual intervention to ensure the dimensional accuracy of the desired phantom. Yip et al. (2011) studied the effect of varying wall thickness in the phantom due to the dip moulding method. It was found that the variations lead to the poor mechanical performance of the phantom. Arcaute and Wicker (2008) employed a dip spinning method to fabricate artery phantoms of complex shapes like the aorta and aortic arch. It was reported that the wall thickness was difficult to control in more minor phantoms. Also, dipping resulted in the use of an excessive amount of silicon than required. Thus, the method was not cost-effective.

2.3.4 Spin coating

Spin coating is a method employed to manufacture uniform tubes of thickness ranging from micrometres to nanometres. The spin coating can be broken down into crucial steps: Deposition, Spin-up, Spin-off, Evaporation (Sahu et al., 2009). These steps of spin coating are illustrated in Figure 13.

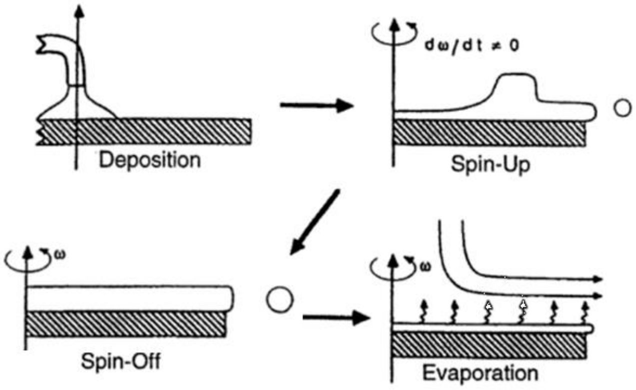

Figure 13 Stages of spin coating (Patil et al., 2016).

Lan (2012) used spin coating to fabricate a brachial artery segment for arm phantom testing. Since the outer diameter of the brachial artery was assumed to be 6.2 mm, the steel bar used in the study was 5 mm in diameter. Due to such small size, the bar underwent sagging and had to be replaced by a more rigid rod of the same diameter. The investigation marked the importance of rigidity and surface finish of the specimen mould around which the phantom is cast.

2.3.5 Extrusion moulding

Extrusion moulding is one of the prime methods used to develop prosthetics, surgical guides and phantoms since the 1990s (Gateno et al., 2003). It has been widely used in previous studies to construct simple cylindrical models of phantoms. However, this technique can be feasibly incorporated in the development of anthropometrically accurate phantoms with moulds generated through additive manufacturing methods like that of 3D printing. Mille et al. (2020) developed an anatomical paediatric torso phantom with thirty separate anatomical regions with a thermoplastic dual nozzle 3D printer. The study concluded that the phantoms could be printed in parts and assembled to develop an anatomically accurate geometry for verification purposes.

Kiarashi et al. (2015)developed an anthropometric breast phantom based on the data obtained from CT imaging. A 3D model was developed using the data and was fabricated using a high-resolution multi-material 3D printing technology. The developed phantoms were characterised visually and quantitatively. It was reported that the multi-material approach led to the formation of air bubbles and air pockets during the filling process. However, another phantom was developed with a single material 3D printing approach that offered accurate anatomy and ease of use, making it prospective to use in virtual clinical trials.

2.4 Material selection

This section delves into available tissue-mimicking materials used in previous studies, their mechanical properties and feasibility.

2.4.1 Poly Vinyl Alcohol

Poly Vinyl Alcohol (PVA) is a semi-crystalline hydrogel material that is widely used in the fabrication of tendon repair, ophthalmology, phantoms, and several biomedical applications (Schmedlen et al., 2002). PVA is manufactured by polymerisation of a hydrolysed poly-vinyl acetate (Reinertsen & Collins, 2006). The degree of polymerisation and hydrolysis determines the physical properties of the water-soluble polymer (Liechty et al., 2010). The mechanical properties of PVA can be altered by altering the polymer concentration. Schmedlen et al. (2002) prepared and tested the mechanical properties of PVA hydrogels with concentrations of 30 and 15 weight % PVA. The tensile test resulted in an elastic modulus of 838 ± 194 KPa and 125 ± 13 KPa for 30 and 15 % weight concentrations.

Some desirable characteristics of PVA which make it suitable for phantom emulation are (a) Inexpensive. (b) Ease of formulation. (c) Ability to tune mechanical properties by varying the concentration (Surry et al., 2004). On the other hand, the limitations of PVA are (a) Rapid drying and mould growth when not stored in water. (b) Limited shelf-life (c)

Cold worked, resulting in water retention and contraction of the final gel, making it smaller than mould.

2.4.2 Styrene Ethylene Butylene Styrene

Styrene Ethylene Butylene Styrene (SEBS) is often used in ballistic Gelatin because of its mechanical properties like elastic modulus, strength, hardness, and yield strength. SEBS is a copolymer and, when introduced to a hydrocarbon oil, acts as a tissue-mimicking material with high temporal stability (Cabrelli et al., 2017). In mineral oil, it is widely used to fabricate phantoms ranging in various grades of stiffness and high resistance to rupturing. Oudry et al. (2009) tested five SEBS gel phantoms that were 8.5 cm in diameter and 7.5 cm in height to study the various properties of the SEBS gel phantom offers compared to other phantom materials. This testing discovered that the elastic modulus of SEBS gel phantoms could range from 2.2 kPa to 150 kPa and keep their mechanical stability over time. Additionally, the SEBS polymer has the ability of thermal reversibility, making it a desirable material for tissue making. In previous studies, SEBS was used to emulate human brain tissue (Charalambos Vlachopoulos et al., 2012) and ligaments (Ciszkiewicz & Milewski, 2019).

The advantages of using SEBS are (a) a Flexible range of mechanical properties, (b) Stable elasticity, (c) Recyclable (d) Inexpensive. Some limitations of SEBS are: (a) Unstable during annealing (b) Requires heat to be cured.

2.4.3 Gelatin

Gelatin is a gel producing polysaccharide with a sugar galactose skeleton that forms a gel network during the gelling in an aqueous solution. Gelatin is a jelly-like substance that is derived from red algae, and it is often used to provide a growth medium for microorganisms. (Pavan et al., 2010). Gelatin is an incomplete protein found in both humans and animals derived from collagen. Depending on the concentration, Gelatin can produce a material with low stiffness. Because of this, Gelatin is often used in combination with agar to promote flexibility (Chen et al., 2004). Whereas a high concentration of agar is used in combination with Gelatin to promote material stiffness and higher elastic moduli, due to its brittleness, agar can only withstand a limited amount of force before it breaks (Chen & Shih, 2013). Formaldehyde is often used with these two materials to act as a cross-linking agent to stabilise the gel. Gelatin is widely used to develop phantoms because of its tissue-like properties, low cost, and ease of fabrication. The advantages of Gelatin are: (a) Inexpensive. (b) Safe to use. (c) Vivid range of properties as per the molecular weight. However, the disadvantages are (a) Susceptible to mould growth. (b) The requirement of antibiotics (c) Antiseptic compounds to prevent mould growth. (d) Short shelf life

2.4.4 Silicone

Silicone is used for tissue-mimicking because it is inexpensive, mouldable, flexible, and optically transparent (Zhang et al., 2013). Silicone compounds are available in two parts; one contains an elastomer base, and the other contains a curing agent and is cured in an oven, UV machine, or at room temperature. This two-part assembly allows Silicone access to a wide range of mechanical properties and makes it useful for numerous applications (Chikkaveeraiah et al., 2009). In a study using silicone materials to simulate tissue biomechanics related to deep tissue injury, Sparks et al. (2015) tested three materials for their viability. The three materials tested were from ‘Smooth-On’s’ range of material Dragon skin, Eco flex 0030 and Eco flex 0010. Compression tests on each material are observed in Figure 14. From the stress and strain curve, we can identify the elastic moduli of the three materials, 230 kPa, 100 kPa and 50 kPa for Ecoflex 0030 and Ecoflex 0010, respectively.

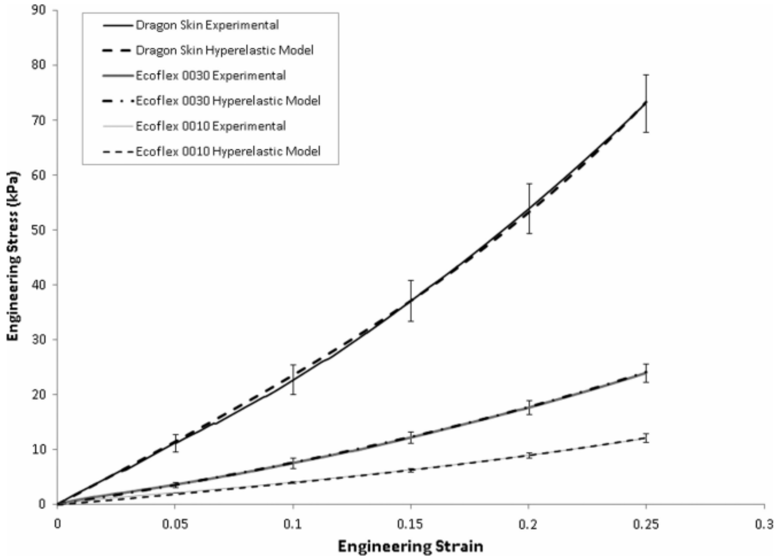

Figure 14 Stress-Strain relationship of Smooth-On’s range of materials under compression (Sparks et al., 2015).

Heo et al. (2020) investigated commercial Silicone for its mechanical characteristics to emulate grasping objects by human palm. The silicone materials tested were Ecoflex of various shore hardness to characterise their mechanical behaviour. The materials were subjected to three different testing methods: uniaxial tensile, planar tension, and uniaxial compression. The stress-strain relationship of the materials for the given tests are illustrated in Figure 15. The uniaxial tests aid in determining Young's modulus, maximum elongation, and Poisson's ratio. The planar test was conducted to observe the material's response to shear deformation.

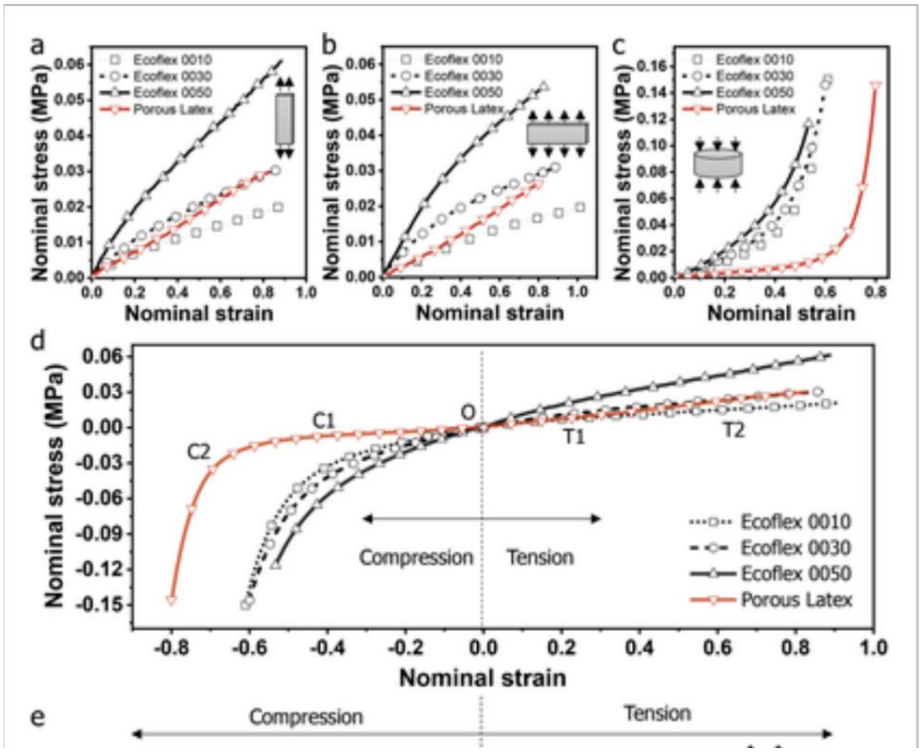

Figure 15 Stress-Strain curves of Ecoflex 0010, Ecoflex 0020, Ecoflex 0030, Porous latex under tensile, compression and pure shear loading (Heo et al., 2020)

The advantages of using Silicone are: (a) Rapid curing time, (b) Quick preparation, (c) Shelf life is moderate. The disadvantages of using Silicone are: (a) Expensive since it uses platinum-based enzyme in curing (b) It is stiffer than natural tissue (c) Susceptible to air bubble entrapment.

2.5 Previous upper arm models

In the past, various physical and mathematical arm models have been contrived to understand and analyse the relationship between blood pressure and corresponding NIBP devices.

2.5.1 Mathematical arm models

Cristalli et al. (1992) developed a simple mathematical model that emphasises the influence of tissue elastic properties like Poisson's ratio and Young's modulus on the pressure profile of the upper arm upon cuff occlusion. An axisymmetric cylindrical model containing soft tissue and bone were used to develop a mathematical model. The brachial artery was omitted in this model.

Ursino and Cristalli (1996) developed a complete upper arm model that included a brachial artery and a more accurate description of the arterial pressure-volume characteristics. The geometry of the formulated model is illustrated in Figure 16. The artery deformation under the cuff was calculated using the tube law. The mathematical model inferred that the alterations in the mechanical properties of the soft tissues affect the accuracy of the BP measurement.

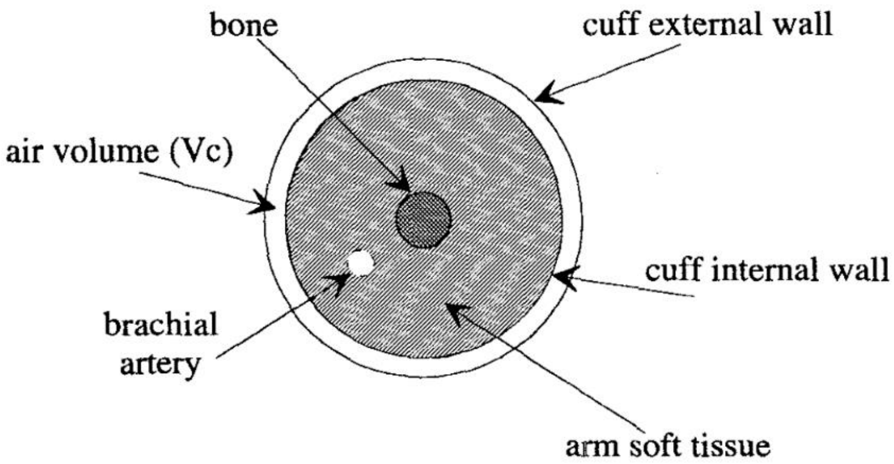

Figure 16 Arm model developed by Ursino and Cristalli (1996)

Lan (2012) developed an anatomically accurate 3D FEA model from the VHP dataset that mimics the oscillometric NIBP measurement method. The geometry of the model is illustrated in Figure 17. The study emphasised the importance of the nonlinearity of the brachial artery in the measurement of BP using the oscillometric method. A Neo-Hookean hyperelastic material model was assigned to the brachial artery. Surface strain distributions for various arm motions were studied from the FEA model. However, the anatomically accurate FEA model was validated against a simple cylindrical arm phantom.

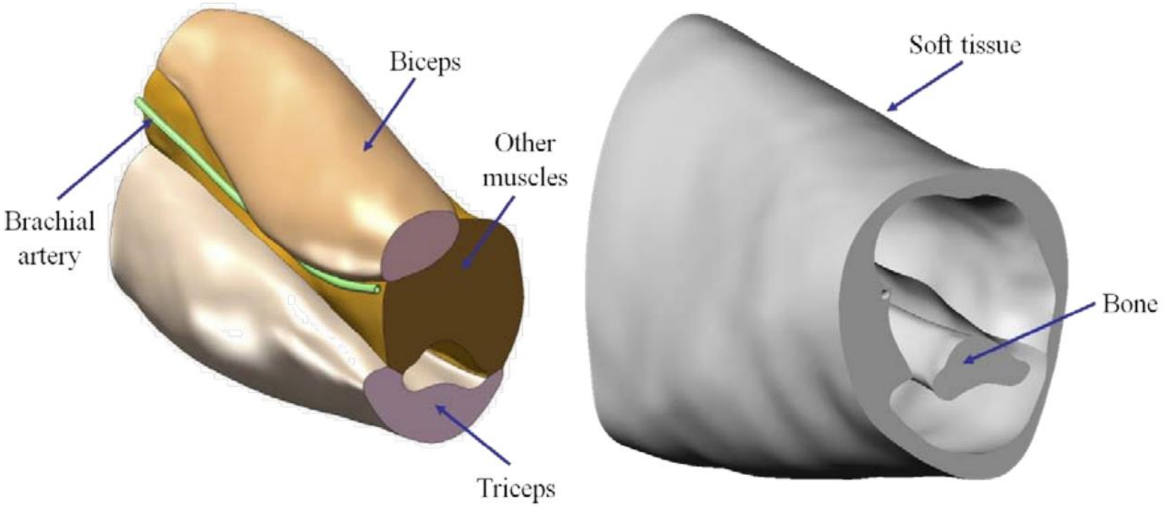

Figure 17 The anatomically accurate upper arm model develop from VHP dataset (Lan, 2012)

Deng and Liang (2016) created FEA models to analyse the stresses generated in the upper arm during BP measurement by cuff compression. Two models were built to quantify these stresses: a cylindrical model and an anatomical model constructed from CT images of the upper arm. The simple cylindrical model was verified with a previous study carried out by Lan (2012). The developed models are illustrated in Figure 18. A Neo-Hookean hyperelastic material model with Poisson's ratio of 0.45 was used to emulate the non-linear elastic properties of the soft tissues. It was reported that the stresses developed on the soft tissues were sensitive to cuff pressure distribution and contact status between muscle and the humerus bone. The magnitude of the CP and variations in the soft tissue elastic properties had a minor influence on the efficiency of pressure transmission on soft tissues. A dense SAT layer in obese patients exhibited a reduced pressure transmission from the cuff to the soft tissue, potentially inferring the overestimation of BP among obese people using NIBP measurement devices.

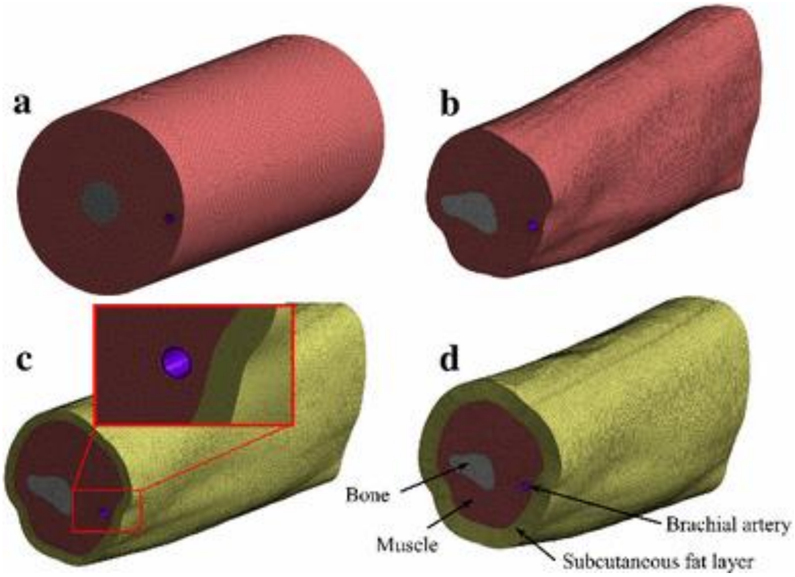

Figure 18 (a) Upper arm simple cylindrical model (b) Anatomical shape developed using CT images (c) A SAT layer is introduced to simulate an obese model (d) Severely obese model is generated (Deng & Liang, 2016)

2.5.2 Upper arm physical phantoms

Anderson-Jackson (2016) fabricated a simple cylindrical upper arm phantom to calibrate and estimate the performance of NIBP monitors. The arm phantom did not constitute a separate brachial artery. A hollow cylindrical void of the same geometry schematised the brachial artery. The arm phantom was developed using SEBS gel having a weight concentration of 10 %. However, SEBS gel samples of 10%, 15% and 20% were characterised for their mechanical properties. It was concluded that 15% SEBS gel was the optimum formulation to achieve the desired tissue mechanical properties for the upper arm phantom. The image of the developed phantom is illustrated in Figure 19. The arm phantom fabricated using a 10% SEBS material formulation did not undergo occlusion at the brachial artery under normal BP measurement conditions. Due to this, the BP could not be measured from the constructed phantom. Also, it could not be connected to a cardiovascular circulatory loop system, which was another objective of the study. It was concluded that 15% SEBS gel material was a feasible formulation for emulating upper arm soft tissue properties.

Figure 19 Simple cylindrical arm phantom fabricated using 15% SEBS gel (Anderson-Jackson, 2016)

Lan (2012) developed an upper arm phantom to represent the BP measurement process, investigate the relationship between BP pulse in the brachial artery and pressure oscillation in the inflatable cuff, and validate the developed mathematical models. The brachial artery was represented with a cylindrical void in the cylindrical soft tissue. The humerus bone was represented with a cylindrical aluminium rod at the centre of the phantom. The mould used to cast this upper arm phantom is illustrated in Figure 20. The Silicone used to emulate soft tissue was Proskin which is made of a two-part mixture. It was reported that the elastic modulus of Proskin could be tweaked by adding a silicone diluent. Accordingly, Proskin with 15% diluent was used to fabricate soft tissue for the phantom. The brachial artery closure process under external cuff pressure was determined using an ultrasound device.

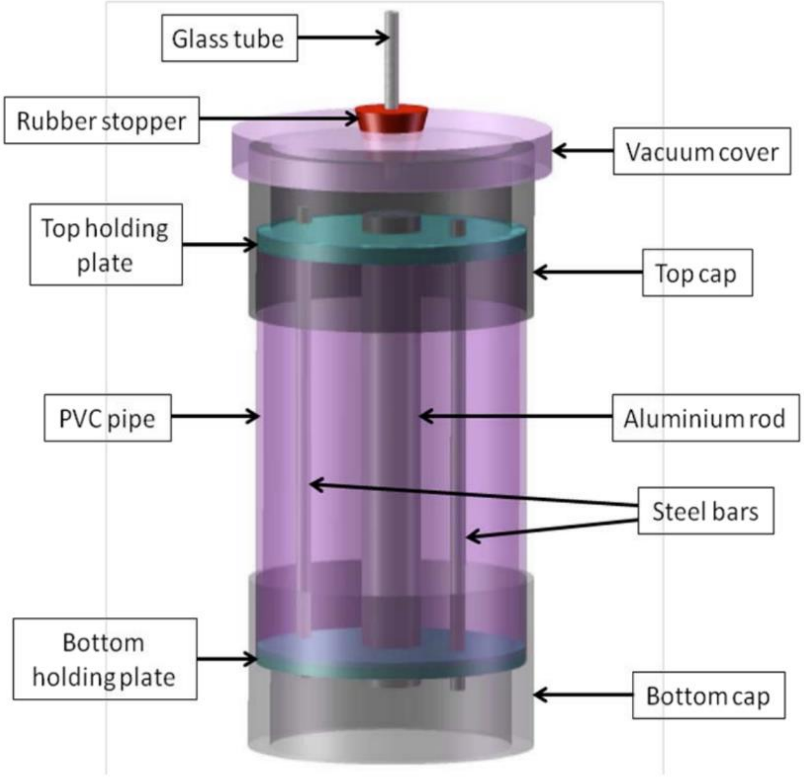

Figure 20 Schematic diagram of the mould used to cast the cylindrical upper arm phantom (Lan, 2012).

Figure 21 Cylindrical arm phantom with a separate arterial wall developed using Platsil-00 (Subburaj, 2020).

Subburaj (2020) fabricated an upper arm phantom of simple cylindrical geometry. The brachial artery was schematised as a separate component fabricated from Platsil-00 silicone. A wood of cylindrical shape represented humerus bone. The soft tissue of the phantom was cast around the brachial artery with Platsil-00. A picture of the phantom is illustrated in Figure 21. To get rid of the air bubbles, degassing was done in a vacuum chamber. This process required the working time of Silicone to be increased, which was achieved by adding retarder71 to the mixture. It was reported that the adhesion between the two was firm, being fabricated from the same material. Arterial deformations at various pressure loads were determined using ultrasound imaging. The ultrasound imaging was conducted by immersing the phantom underwater. However, it was reported that the repetitive testing of the phantom led to the separation of the brachial artery from the soft tissue in certain areas.

2.6 Conclusion

This chapter provides a comprehensive review and discussion on the previous methodologies and analysis to develop computational and physical upper arm phantoms. The following points are weakly treated in the available models:

1. The axisymmetric cylindrical FEA models previously developed were verified, assuming that the soft tissue undergoes linear deformation during BP measurement. However, it is inferred from the literature that the soft tissue exhibits large deformations.

2. The anatomically accurate computational phantoms developed from CT or MRI data did not represent a large population sample. VHP takes just one individual's dataset into account. An anatomical model based on a larger population is likely to improve the relevance of the results in terms of BP estimation.

3. The current mathematical models were not developed to study the combined effects of blood pressure and cuff pressure on the brachial artery and its surrounding soft tissue.

4. It can be inferred from the literature that material characterisation plays a critical role in the mathematical modelling of soft tissues that deforms nonlinearly. The current material models did not account for a thorough stress-strain relationship determination of the available materials.

5. The physical upper arm phantoms developed so far are limited to cylindrical geometries. The moulding approaches for these phantoms have remained similar. Anatomically accurate phantoms have not been developed and studied.

6. Estimation of the mechanical properties of the hyperelastic materials like Young's modulus from material testing is weakly inferred.

2.7 Objectives

Following are the objectives of this thesis to overcome the shortcomings of the current models and literature:

1. Develop a simple axisymmetric FEA and an analytical model based on the principles of solid mechanics to understand, analyse, and verify the displacements and volume changes on the upper arm components during NIBP measurement.

2. Develop an accurate FEA model adhering to a realistic geometry and solve it as a non-linear model exhibiting large deformations to investigate displacements and volume changes during NIBP measurement.

3. Material selection and characterisation to develop an accurate material model to develop an anatomically accurate computational phantom as an FEA model.

4. Employ the characterised material to fabricate an anatomically accurate physical phantom

5. Construct a test rig to validate the established FEA model.

An outline of the required steps to meet the objectives of this study is illustrated in Figure 22.

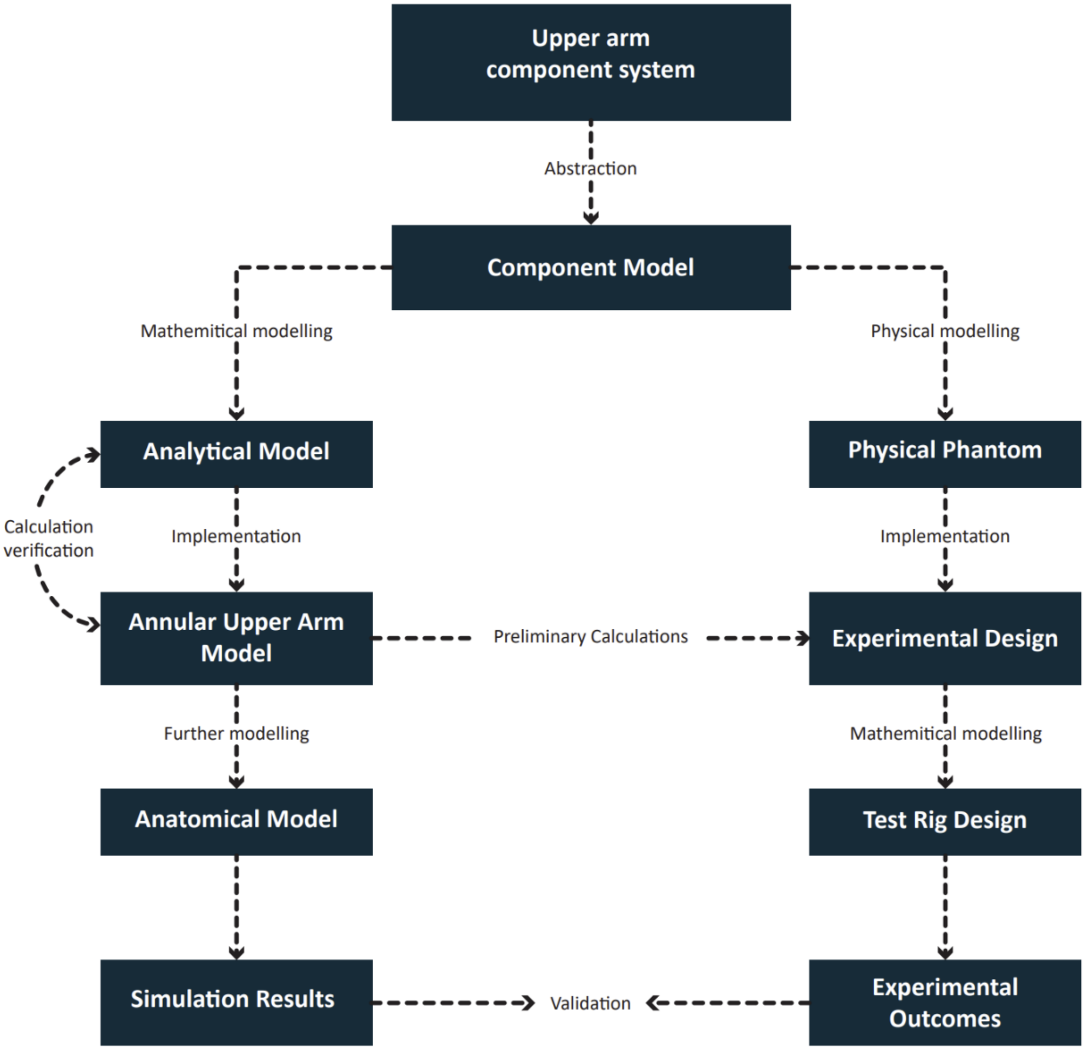

Figure 22 Road map of the study

Chapter 3 Model conceptualisation

3.1 Introduction

This section intends to dictate the process of upper arm computational model progression from an annular concentric geometry to an anatomical geometry. In the annular model, the brachial artery is assumed as a cylindrical void at the centre of the soft tissue, omitting the humerus bone (Refer Figure 22). The simple formulation of the annular model allows for a detailed analysis of the mechanical effects on soft tissue and the brachial artery during NIBP measurement. It also allows for the analytical verification of the model using principles of continuum mechanics.

In succession to the annular model, a simple cylindrical model is developed where the humerus bone is introduced at the centre of the upper arm soft tissue, and the brachial artery is moved to a distant location near the end of the upper arm. The simple cylindrical model is illustrated in Figure 24. The geometric parameters are chosen from Table 3. The improved location of the brachial artery pertaining to the anatomical setting allows for an NIBP measurement analysis that closely resembles the actual phenomenon.

The geometry of the anatomical model is developed as a combination of the upper arm MRI data obtained from Zygote (2020) model and the reviewed parameters from Table 3. A SAT layer is introduced on the top of the muscle layer, allowing to study the mechanical effects on the soft tissues arising from the interactive tissue conditions during NIBP measurement. A schematic diagram of the anatomical model is illustrated in Figure 25.

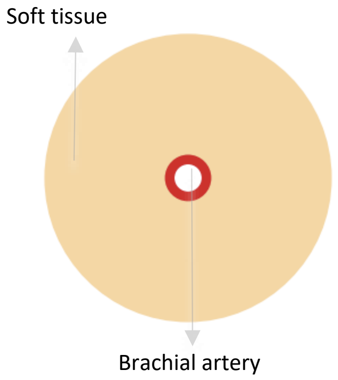

Figure 23 Annular concentric model illustration

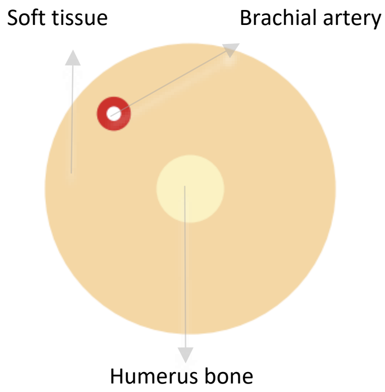

Figure 24 Simple Cylindrical model illustration

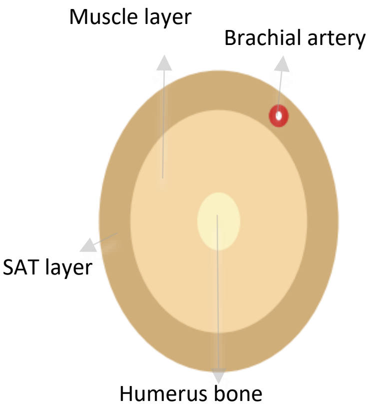

Figure 25 Anatomical model illustration

3.2 Linear Annular concentric model

The annular concentric model aids in establishing the mathematical model solved in ANSYS with the analytical model formulated using the governing equations of linear elastostatics. The fundamental assumptions of linear elastic models are Infinitesimal strains and conformance to Hooke's law. The material model used in this formulation is a linear isotropic material.

3.2.1 Formulation

The geometry of the upper arm is assumed to be a perfect circle of radius 'R_o'. The brachial artery is assumed to be a circular void of radius 'R_I' at the centre of the arm with no arterial wall. The arm is composed of soft tissue that is assigned a linear isotropic material. The behaviour of the material is such that the stress-induced is directly proportional to the strain and independent of the orientation of the material body conforming to Hooke's law of elasticity. The material is defined by Young's modulus 'E' and Poisson's ratio 'ν'. The brachial artery is subjected to a pressure P_I. The soft tissue is subjected to pressure P_O representing the cuff pressure.

The boundary conditions for stress 'τ' in polar coordinates are:

$$\tau_{rr} = -P_I, \qquad \tau_{r\theta} = 0 \qquad \text{on} \quad r = R_I,$$

$$\tau_{rr} = -P_O, \qquad \tau_{r\theta} = 0 \qquad \text{on} \quad r = R_O.$$

This 2D annular concentric model essentially forms an axisymmetric plane problem where two cases arise: Plane strain condition and Plane stress condition. According to the governing equations of linear elastostatics, where time derivate is insignificant, the following solutions were obtained. The equations below are derived by Dr Tet Chuan Lee.

3.2.1.1 Axisymmetric plane strain condition

In this case, the annular concentric model is constrained in the axial plane, allowing it to be displaced in the (r, θ) plane only. Therefore, the displacements are independent of z and take the following form:

Displacement in radial plane 'u_r' is given by:

$$\boldsymbol{u_r = C_1 r + C_2 \frac{1}{r}}, \tag{3.1}$$

The strains $'e'$ are given by:

$$\boldsymbol{e_{rr} = C_1 - C_2 \frac{1}{r^2}}, \tag{3.2}$$

$$\boldsymbol{e_{\theta\theta} = C_1 + C_2 \frac{1}{r^2}}, \tag{3.3}$$

All other strains $(e_{zz} = e_{r\theta} = e_{rz} = e_{\theta z} = 0)$ in this condition are zero.

The stresses $'\tau'$ are given by:

$$\boldsymbol{\tau_{rr} = \frac{E}{(1+\nu)(1-2\nu)} C_1 - \frac{E}{(1+\nu)} C_2 \frac{1}{r^2}}, \tag{3.4}$$

$$\boldsymbol{\tau_{\theta\theta} = \frac{E}{(1+\nu)(1-2\nu)} C_1 + \frac{E}{(1+\nu)} C_2 \frac{1}{r^2}}, \tag{3.5}$$

$$\boldsymbol{\tau_{zz} = \frac{2E\nu}{(1+\nu)(1-2\nu)} C_1}, \tag{3.6}$$

The volume change at the outer surface of the upper arm is found to be given by:

$$\boldsymbol{\Delta V_O = 2\pi Z\left(C_1 {R_O}^2 + C_2\right)}. \tag{3.7}$$

Where, Z is the length of the arm.

The volume change at the inner surface of the arm was found out similarly, except the outward unit normal being negative. It gives:

$$\boldsymbol{\Delta V_I = -2\pi Z\left(C_1 {R_I}^2 + C_2\right).} \qquad (\mathbf{3.8})$$

The strain energy density is given by:

$$\boldsymbol{s = \frac{E}{(1+\nu)(1-2\nu)} {C_1}^2 + \frac{E}{(1+\nu)} {C_2}^2 \frac{1}{r^4}.} \qquad (\mathbf{3.9})$$

The total strain energy in the system is found to be given by:

$$\boldsymbol{U = 2\pi Z \frac{E}{2(1+\nu)} \left[{R_O}^2 - {R_I}^2\right] \left\{ \frac{1}{(1-2\nu)} {C_1}^2 + {C_2}^2 \left[\frac{1}{{R_I}^2 {R_O}^2} \right] \right\}.} \qquad (\mathbf{3.10})$$

In the equations (3.1 – 3.10) above, the elastic constants C1 and C2 are given by:

$$C_2 = \frac{(1+\nu)}{E} \frac{(P_I - P_O){R_I}^2 {R_O}^2}{{R_O}^2 - {R_I}^2},$$

$$C_1 = \frac{(1+\nu)(1-2\nu)}{E} \left[\frac{P_I {R_I}^2 - P_O {R_O}^2}{{R_O}^2 - {R_I}^2} \right]$$

$$x = rcos\theta, y = rsin\theta$$

$$r = sqrt(x^2 + y^2), \theta = \arctan\left(\frac{y}{x}\right)\ (Cartesian\ to\ cylindrical\ coordinates)$$

3.2.1.2 Axisymmetric plane stress condition

In this case, there is a non-zero strain in the zz direction but zero stress, $\tau_{zz} = 0$. It can be inferred that if the strain is constant in z plane, then e_{zz} is constant as well. Thus, the solution for displacement u_r is of the same form as obtained in the plane strain case with a different expression for C_1.

The displacements are given by:

$$\boldsymbol{u_r = C_1 r + C_2 \frac{1}{r},} \tag{3.10}$$

$$\boldsymbol{u_z = -\frac{2\nu}{(1-\nu)} C_1 Z} \tag{3.11}$$

As displacement u_r has the same form, strains 'e_{rr}' and '$e_{\theta\theta}$' also have the same form and with the additional non-zero e_{zz} term. Thus, the strains are given by:

$$\boldsymbol{e_{rr} = C_1 - C_2 \frac{1}{r^2}} \tag{3.12}$$

$$\boldsymbol{e_{\theta\theta} = C_1 + C_2 \frac{1}{r^2}} \tag{3.13}$$

$$\boldsymbol{e_{zz} = -\frac{2\nu}{(1-\nu)} C_1} \tag{3.14}$$

As stress τ_{zz} is zero, the other two stresses are given by:

$$\boldsymbol{\tau_{rr} = \frac{E}{(1-\nu)} C_1 - \frac{E}{(1+\nu)} C_2 \frac{1}{r^2},} \tag{3.15}$$

$$\boldsymbol{\tau_{\theta\theta} = \frac{E}{(1-\nu)} C_1 + \frac{E}{(1+\nu)} C_2 \frac{1}{r^2},} \tag{3.16}$$

It is evident that equations 3.15 and 3.16 are similar to equations 3.4 and 3.5 from the plane strain condition but with different elastic constants C1 and C2.

Since the displacement remains unchanged for the plane strain condition, the volume change remains unchanged as well except for the elastic constant C2.

The volume change for the outer surface of the arm is given by:

$$\boldsymbol{\Delta V_O = 2\pi Z\left(C_1 {R_O}^2 + C_2\right),} \tag{3.17}$$

Volume change for the inner surface of the arm, which is assumed to be the brachial artery, is given by:

$$\boldsymbol{\Delta V_I = -2\pi Z\left(C_1 {R_I}^2 + C_2\right)} \tag{3.18}$$

The strain energy density, in this case, is given by:

$$\boldsymbol{s = \frac{E}{(1-\nu)} {C_1}^2 + \frac{E}{(1+\nu)} {C_2}^2 \frac{1}{r^4}} \tag{3.19}$$

The total strain energy in this system is given by:

$$\boldsymbol{U = 2\pi Z\left\{\frac{E}{2(1-\nu)} {C_1}^2\left[{R_O}^2 - {R_I}^2\right] + \frac{E}{2(1+\nu)} {C_2}^2\left[\frac{{R_O}^2 - {R_I}^2}{{R_I}^2 {R_O}^2}\right]\right\}} \tag{3.20}$$

In the equations (3.10 – 3.20) above, the elastic constants C1 and C2 are given by:

$$C_2 = \frac{(1+\nu)}{E} \frac{(P_I - P_O){R_I}^2 {R_O}^2}{{R_O}^2 - {R_I}^2},$$

$$C_1 = \frac{(1-\nu)}{E}\left[\frac{P_I {R_I}^2 - P_O {R_O}^2}{{R_O}^2 - {R_I}^2}\right].$$

3.3 Non-linear Annular concentric model

The linear case of the annular concentric assumed the soft tissue material to be an isotropic material conforming to the small deflection theory. However, in a physiological phenomenon, the soft tissues undergo large strains (Fung, 1993). This section explains the modelling approach of the annular concentric model using the principles of non-linear elastostatics.

3.3.1 Analytical formulation

In this case, the annular concentric model is formulated in conformance to the large deflection theory while still keeping the material model to be linear isotropic. The linear isotropic model is also known as St. Venant-Kirchoff, which is based on a constitutive equation:

$$\boldsymbol{S} = \lambda \operatorname{tr}(\boldsymbol{E})\, \boldsymbol{I} + 2\mu \boldsymbol{E},$$

where $\boldsymbol{S}$ is the second Piola-Kirchoff stress tensor, $\boldsymbol{E}$ is the Green-Lagrange strain tensor, λ and μ are the Lame constants. The first Piola-Kirchoff stress tensor can be written in the second as

$$\boldsymbol{P} = \boldsymbol{F}\boldsymbol{S}$$

where $\boldsymbol{F}$ is the deformation gradient tensor which can be expressed in terms of the displacement as

$$\boldsymbol{F} = \nabla \boldsymbol{U} + \boldsymbol{I}$$

Hence

$$\boldsymbol{P} = \boldsymbol{F}[\lambda \operatorname{tr}(\boldsymbol{E})\, \boldsymbol{I} + 2\mu \boldsymbol{E}]$$

3.3.1.2 Plane strain condition

The analytical equations were derived for the plane strain case of the axisymmetric models since it emulates the boundary conditions imposed on the upper arm during NIBP measurement. The derived analytical equations are found in the appendix of this thesis. The model conforms to the theory of large deformations.

3.4 Finite Element Method

This section delves into understanding the formulation of the problems solved in ANSYS Mechanical using the Finite Element Method (FEM). A ‘static structural’ component is used to solve the structural problems to obtain the response of a structure under static loading.

The general equation of motion in mechanics is as follows:

$$[M][x] + [C][x] + [K][x] = F(t)$$

Where, $[M]$ is the mass matrix, $[C]$ is the damping matrix, $[K]$ is the global stiffness matrix, $[x]$ is the unknown displacement vector, $[F]$ is the known force vector.

Since time derivative is insignificant in the problem analysis, the time-dependent terms from the above equation are eliminated to obtain the following equation:

$$[K][x] = [F]$$

The equation above, $[K]$, is essentially a constant stiffness matrix wherein the material behaviour is linear elastic. The theory of small deflection is used to solve the equation. The known force vector $[F]$ is applied in a static manner where time-varying forces are dropped. Inertial effects such as damping are not considered.

In ANSYS, the non-linearities arise out of geometric non-linearities, material non-linearities, and contact non-linearities.

3.5 Discussion

In this chapter, the analytical models based on the well-established principles of continuum mechanics were introduced. Axisymmetric models pertaining to the upper arm's parameters, material properties, and boundary conditions were formulated. The formulation of these analytical models allows for establishing and verifying the Finite element method (FEM) to further solve complex numerical models of the upper arm during the NIBP measurement procedure.

Non-linearities in the soft tissue arising from the geometry are formulated using the principles of non-linear elastostatics while still treating the soft tissue as a linear isotropic material. The analytical models do not account for non-linearities related to the upper arm's material properties and interactive tissue conditions. The process of developing models for a FE analysis is discussed in Chapter 4. The axisymmetric FE models are solved and verified. Upon verification of the FE models with the analytical models, the geometry of the upper arm is improved and evolved into an anatomically accurate geometry for further investigation.

4. Finite Element Models

This chapter takes through the process of establishing the linear annular model in ANSYS using the FEM. The solution of this FEM model is verified with the analytical solution formulated in Chapter 3. A non-linear case of the annular model is developed, solved, and verified using the large deflection theory. Furthermore, a simple cylindrical model with the humerus bone, brachial artery, and soft tissue is simulated. The arterial deformation is compared and analysed with an arm phantom of similar geometry.

4.1 Linear Annular model

The annular model is a cylindrical geometry consisting of just linear soft tissue. The brachial artery is essentially a cylindrical void at the centre of the arm. As formulated in Chapter 3, the parameters required to formulate the annular model are: Radius of the upper arm (R_O), length of the upper arm (Z), the radius of the brachial artery (R_I), Young's modulus $'E'$ and Poisson's ratio 'ν'' of the soft tissue, Cuff pressure (P_O) and Arterial pressure (P_I). These parameters are drawn from the literature review in Chapter 2 as follows:

a. The radius of the upper arm is assumed 52 mm .

b. The radius of the brachial artery is assumed 2.2 mm (Dammers et al., 2015).

c. The length of the upper arm is assumed 223 mm (Bonso et al., 2010).

d. Being a linear analysis, the material model chosen for this problem is a linear elastic material defined by Young's modulus and Poisson's ratio. The Young's modulus and Poisson's ratio of the soft tissue are assumed to be 47.5 KPa and 0.45, respectively (Fung, 1993), .

Using the parameters mentioned above, the geometry of the axisymmetric model was constructed in SolidWorks. The geometry was then imported to ANSYS. The boundary conditions imposed on the model defines the case of the axisymmetric model it simulates. The boundary conditions differ for axisymmetric plane strain and plane stress conditions.

4.1.2 Annular plane strain model

In order to simulate this condition, the model is constrained at both ends such that it can only deform in the radial and circumferential plane. The annular plane strain model is illustrated in Figure 26. The boundary conditions in ANSYS were defined as described in the following section.

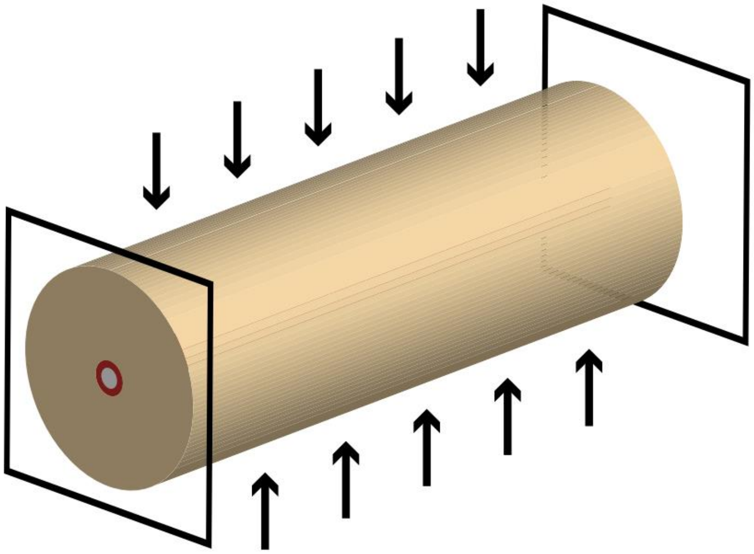

Figure 26 Axisymmetric plane strain model

4.1.2.1 Boundary conditions

a) In ANSYS, the end surfaces of the model were constrained using the 'Fixed support' boundary condition. Although this constrained the model axially, it constrained the surfaces to which the support was applied in the circumferential plane. Since it did not allow the surfaces to deform as desired, it did not create the accurate formulation as per the plane strain model. The imposed boundary condition is illustrated in Figure 27.

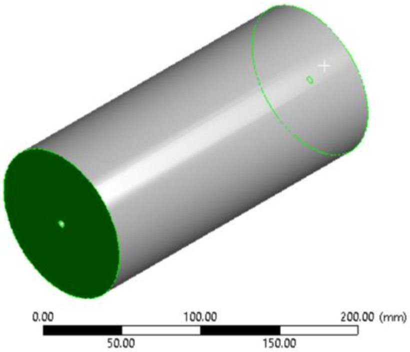

Figure 27 'Fixed support' boundary condition imposition in ANSYS, highlighted in green colour

b) In order to fix this, ‘Frictionless support’ constraints were applied instead of ‘Fixed support’. It allowed the model to be deformed in radial and circumferential planes only, constraining it in the axial plane as desired. However, in ANSYS, the model experienced rigid body motion in the azimuthal direction. Upon application of the pressure loads, the model failed to simulate since the ‘Frictionless support’ boundary condition was not enough to constrain the model in the space accurately. The imposed boundary condition is illustrated in Figure 28.

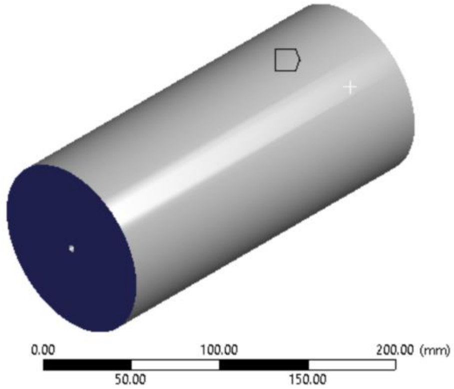

Figure 28 ‘Frictionless support’ imposition in ANSYS, highlighted in purple.

c) In order to prevent the rigid body and thereby the translatory motion experience by the model, the model was required to be constrained and defined precisely. Along with Frictionless support, a remote displacement boundary condition was applied on the edges of the surface on which Frictionless support was applied. In ANSYS, the remote displacement boundary condition is used to guide the displacement and rotation of a face or edge of a structure from a remote point. A deformation behaviour can be added to the assigned entities. Pertaining to the model, the displacements and rotations of the selected edges were set to zero, and the behaviour of these edges was set to ‘deformable’. The combination of these components to implement necessary boundary conditions on the model is illustrated in Figure 29.

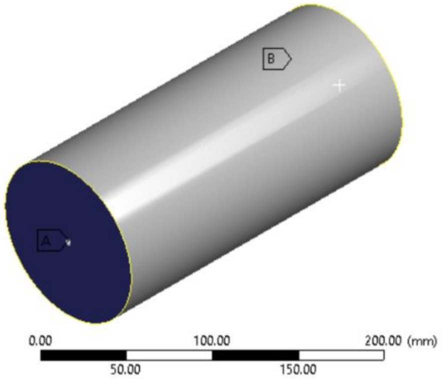

Figure 29 Boundary conditions on the model imposed as a combination. ‘Frictionless support’ is highlighted in purple. ‘Remote displacement’ is highlighted in yellow along the edges on both ends.

d) The combination of Frictionless support and Remote displacement boundary condition allowed the model to simulate without errors.

4.1.2.2 Element and Meshing

The element type used in this analysis is a higher-order 3D 20-node element that exhibits quadratic displacement behaviour. This element is defined by 20 nodes having three degrees of freedom per node: translations in the nodal x, y, and z directions. The shape of the element and its nodes are illustrated in Figure 30. The element supports hyperelasticity, large deflection, and large strain capabilities. It has a mixed formulation capability for simulating deformations of nearly incompressible and fully incompressible hyperelastic materials. In ANSYS, this element is referred to as HEX20 SOLID186.

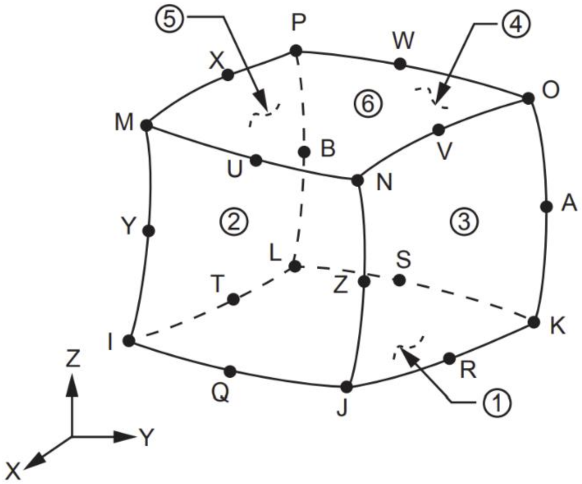

Figure 30 a HEX20 SOLID186 element in ANSYS

It is known that in FEM, a finer element size typically generates more accurate results. However, a finer mesh results in increased computational time. A mesh convergence study shown in Figure 31 was carried out on the model to achieve a balance between accuracy and computational time. The solution results were analysed for coarse (refer to Figure 32) to finer meshes (refer to Figure 33) until no significant improvement was achieved. The solution obtained using ANSYS was compared to the one obtained from the analytical model developed in Chapter 3. The model was simulated for cuff pressure $P_O = 150\ mmHg$ and $P_I = 110\ mmHg$. Using the equation (3.1), the displacement u_r = -0.493 mm at r = 2.2 mm. The negative magnitude suggests that the model experiences compression from the applied pressure loads.

The mesh that generates 2386992 elements corresponds to the element size of 1 mm.

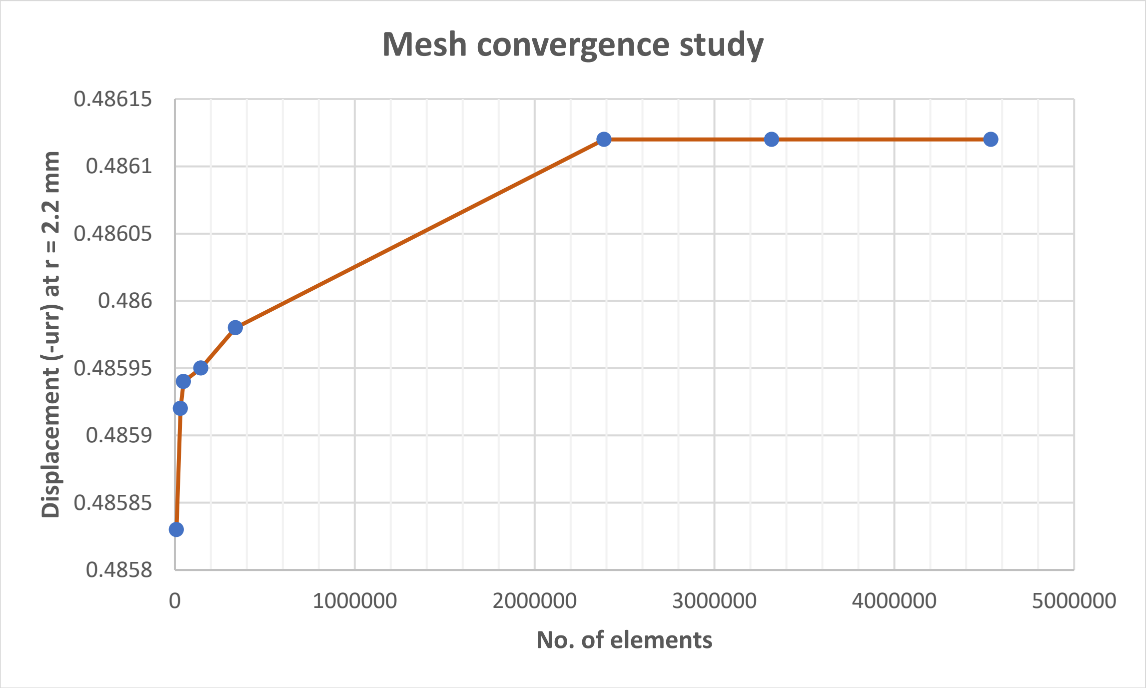

Figure 31 Displacement of the soft tissue ($-u_{rr}$) *vs Number of elements*

Thus, from the mesh convergence study, a fine mesh is suitable to obtain accurate results and is efficient in the computational time taken by the solver.

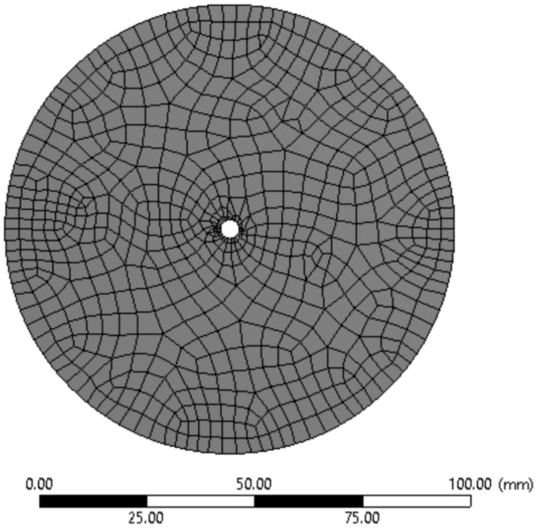

Figure 32 A coarse mesh of element size 5 mm.

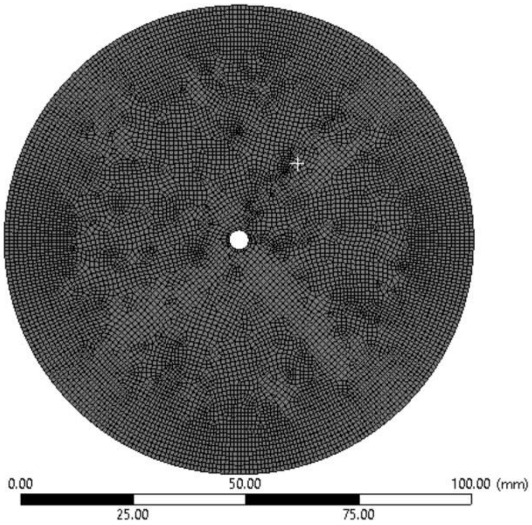

Figure 33 A finer mesh of element size 1mm

4.1.2.3 Results verification

The FE plane strain model was verified against the analytical model for the pressure loads of $P_O = 150\ mmHg, P_I = 110\ mmHg.$

The strain energy density for the given pressure loads was found to be 2.290 J

a) The displacement of the soft tissue at the given pressure loads across the radii of the arm is shown in

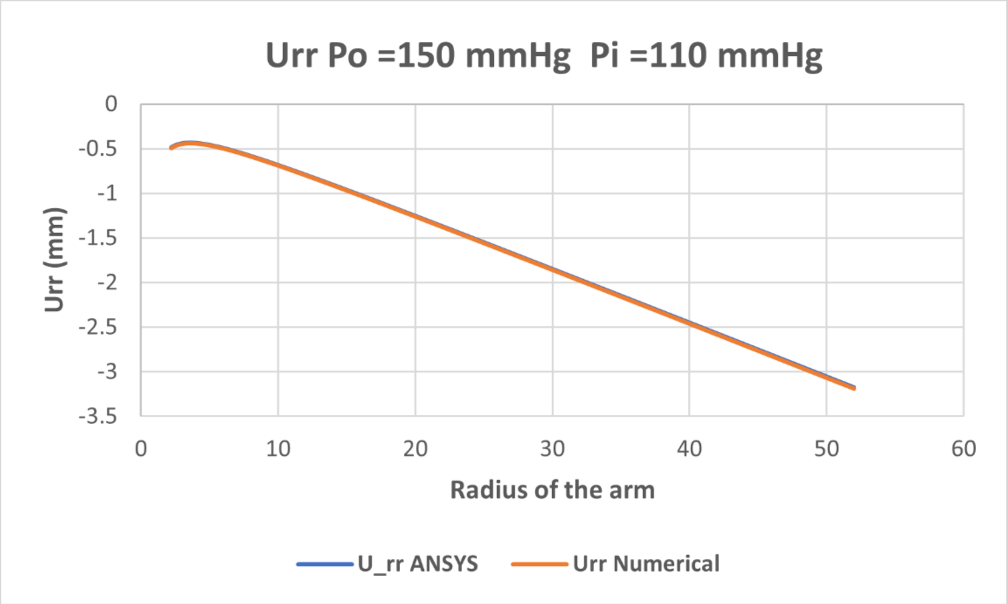

Figure 34 Displacement (u_{rr}) vs. Radius of the arm (axisymmetric plane strain model)

b) The strain $'e'$ on the soft tissue in the radial $'rr'$ and circumferential $'\theta\theta'$ plane at the given pressure loads across the radii of the arm is shown in Figure 35 and Figure 36, respectively.

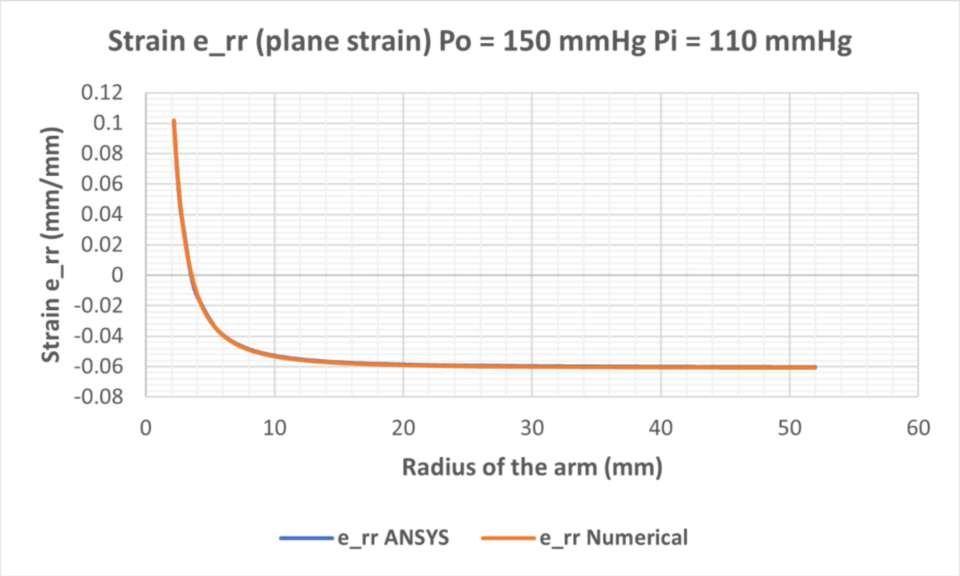

Figure 35 Strain err vs. Radius of the arm (axisymmetric plane strain model)

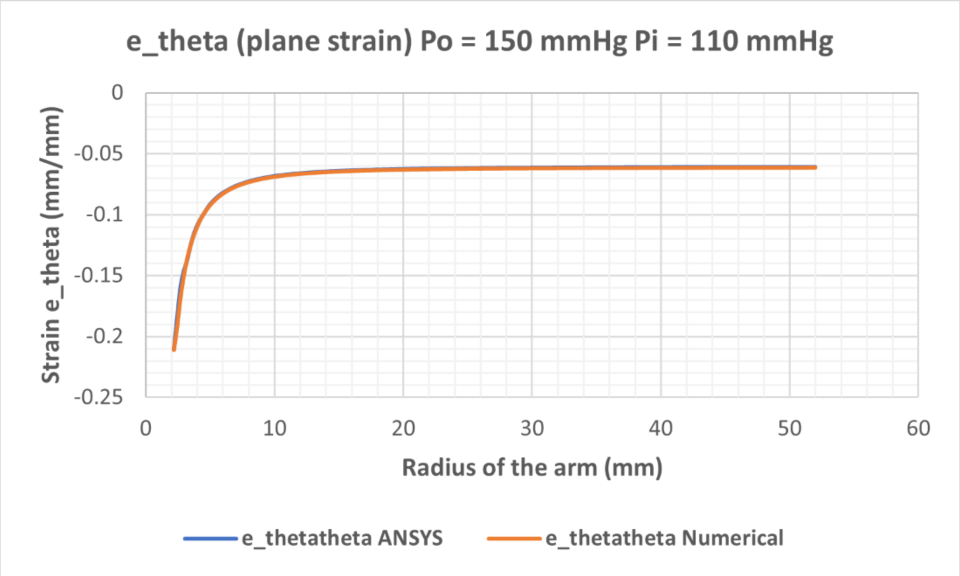

Figure 36 Strain $e\theta\theta$ vs. Radius of the arm (axisymmetric plane strain model)

c) The stresses $\tau_{rr}, \tau_{\theta\theta,}\ \tau_{zz}$ across the radii of the arm are shown in Figure 37, Figure 38 and, Figure 39, respectively.

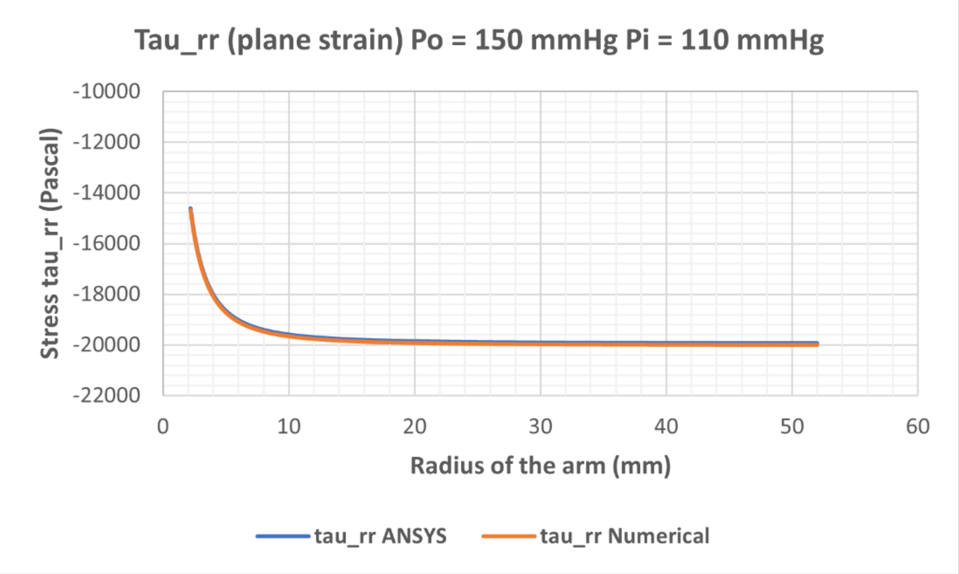

Figure 37 Stress τ_{rr} vs. Radius of the arm (axisymmetric plane strain model)

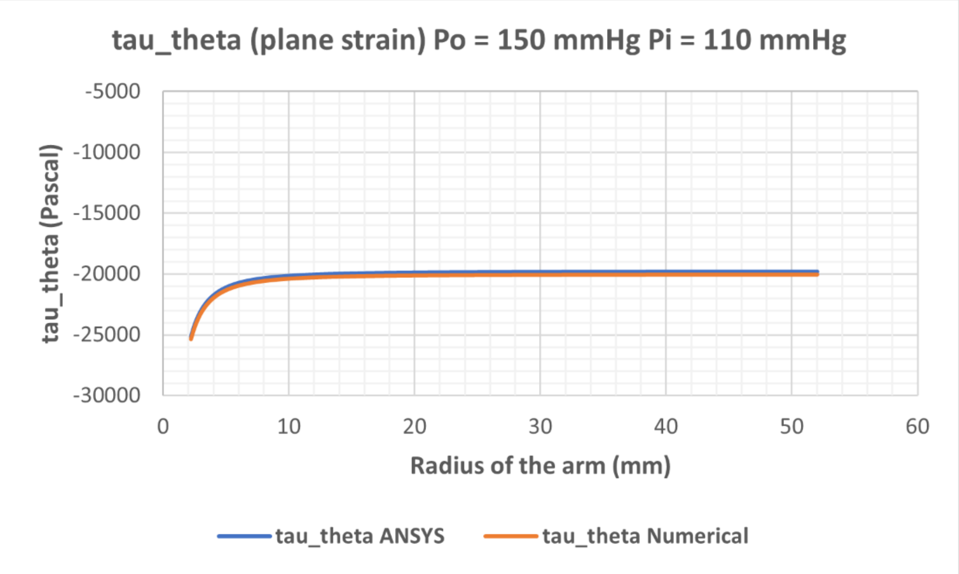

Figure 38 Stress $\tau_{\theta\theta}$ vs. Radius of the arm ((axisymmetric plane strain model)

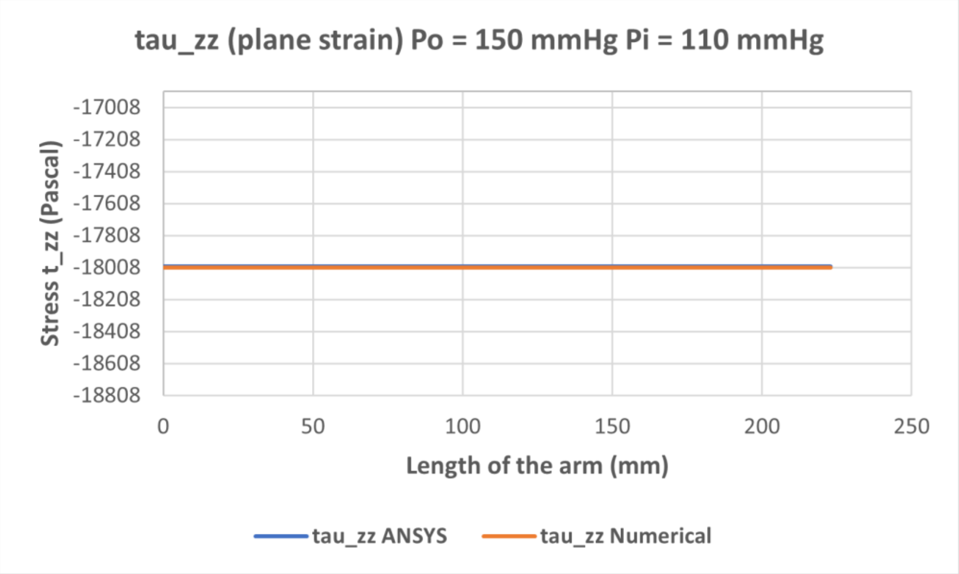

Figure 39 Stress τ_{zz} vs. Radius of the arm (axisymmetric plane strain model)

The volume changes are illustrated in Table 6.

Volume (mm3)	Undeformed	ANSYS	Numerical solution
Soft tissue	1.891E006	1.67E006	1.65E006
Brachial artery	3.39E-006	2.03E-006	1.87E-006

Table 6 Volume changes in the soft tissue and the brachial artery

4.1.3 Annular plane stress model

In this instance of the axisymmetric model, the upper arm is allowed to deform in the axial plane, as illustrated in Figure 40. Since the model is allowed to deform in the axial plane z, there is a non-zero strain in the zz direction but stress, $\tau_{zz} = 0$. Apart from the boundary conditions, other attributes such as the material model, mesh element size pertaining to the plane strain model are used to solve this plane stress model using ANSYS.

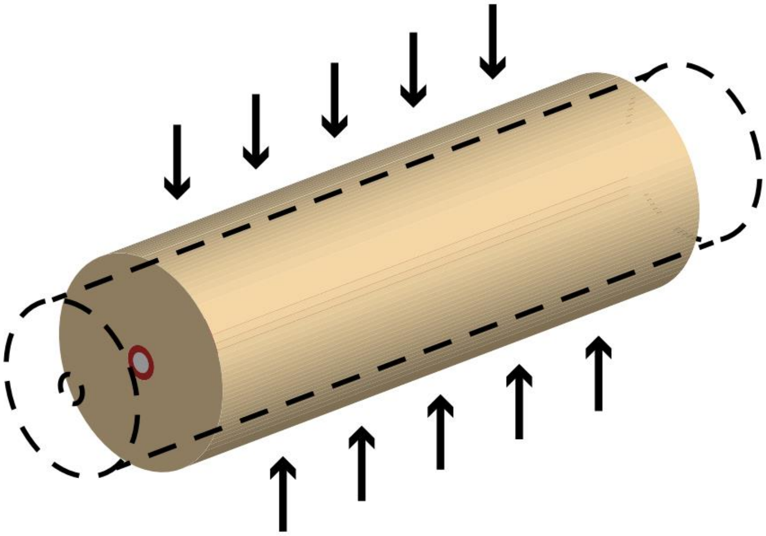

Figure 40 Illustration of the axisymmetric plane stress model

4.1.4 Results verification

The FE plane stress model was verified against the analytical model for the pressure loads of $P_O = 150\ mmHg$, $P_I = 110\ mmHg$.

a) The displacement 'u_r 'across the radii of the arm is shown in Figure 41.

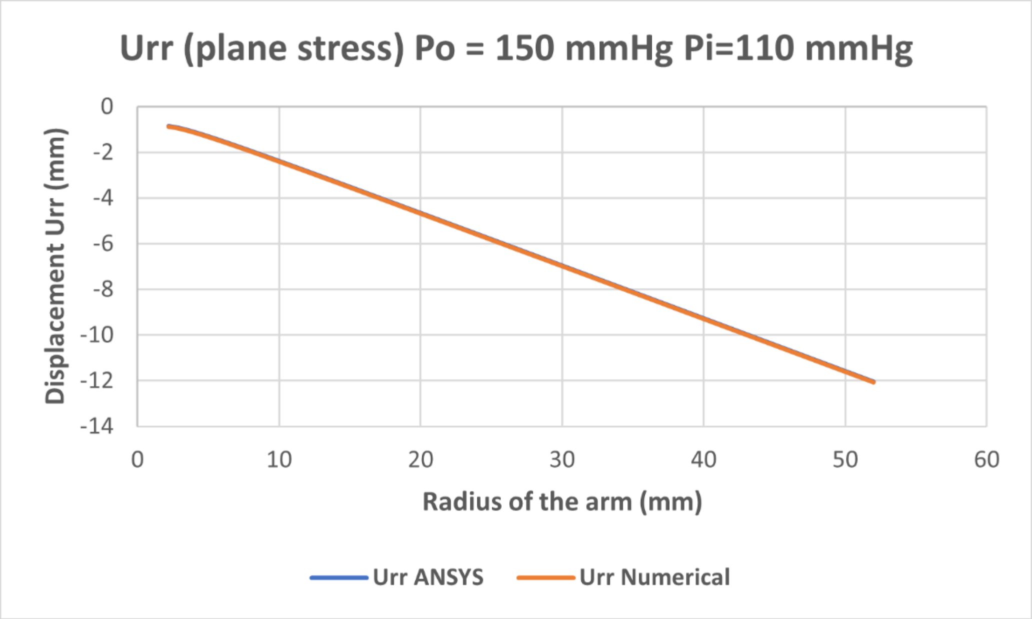

Figure 41 Displacement u_r vs radius of the arm (axisymmetric plane stress model)

b) The strains across the radii and length of the arm are shown in Figure 42, Figure 43, Figure 44.

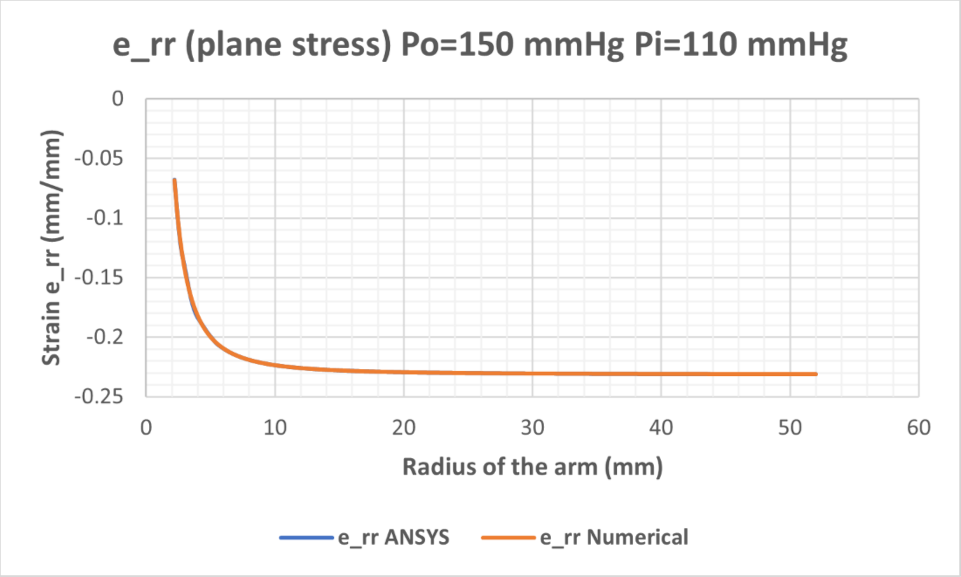

Figure 42 Strain e_{rr} vs radius of the arm (axisymmetric plane stress model)

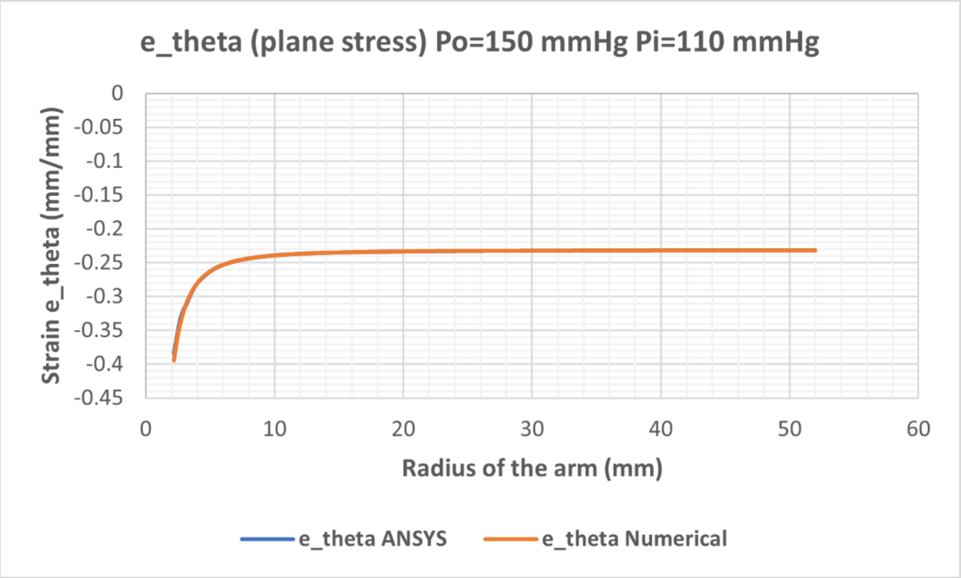

Figure 43 Strain $e_{\theta\theta}$ vs radius of the arm (axisymmetric plane stress model)

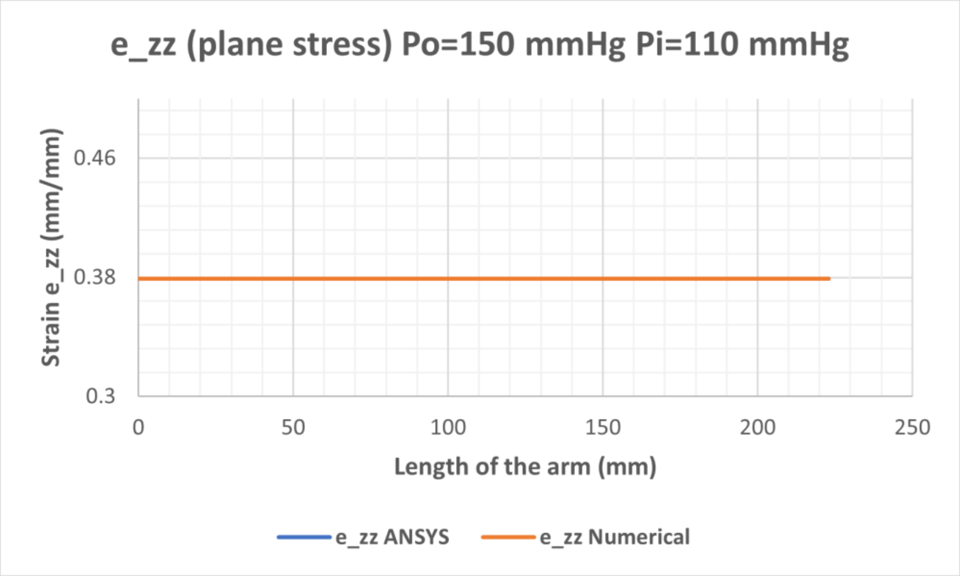

Figure 44 Strain e_{zz} *vs radius of the arm (axisymmetric plane stress model)*

c) The stresses across the radii of the arm are shown in Figure 45, Figure 46.

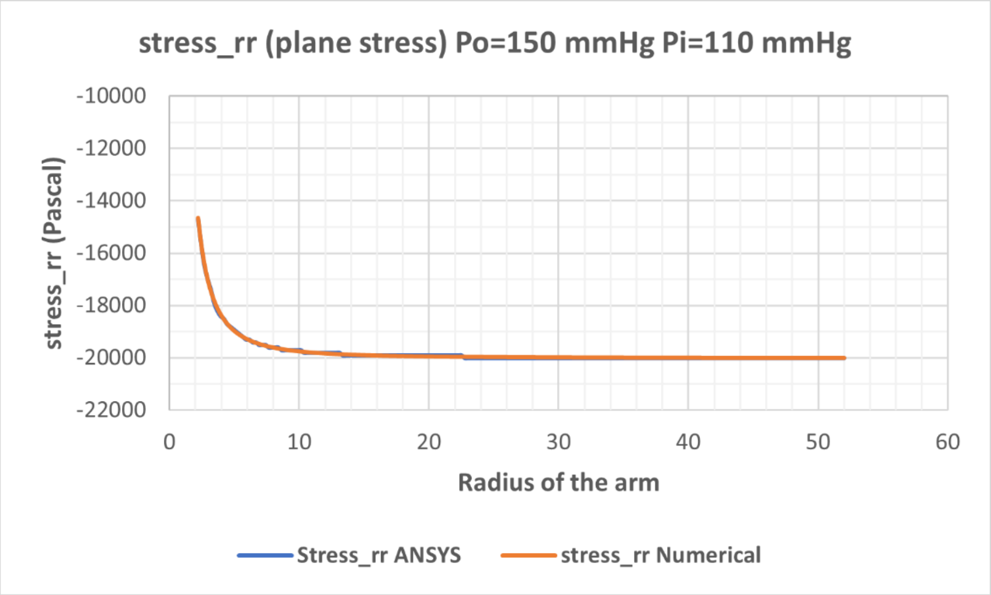

Figure 45 Stress τ_{rr} *vs radius of the arm (axisymmetric plane stress model)*

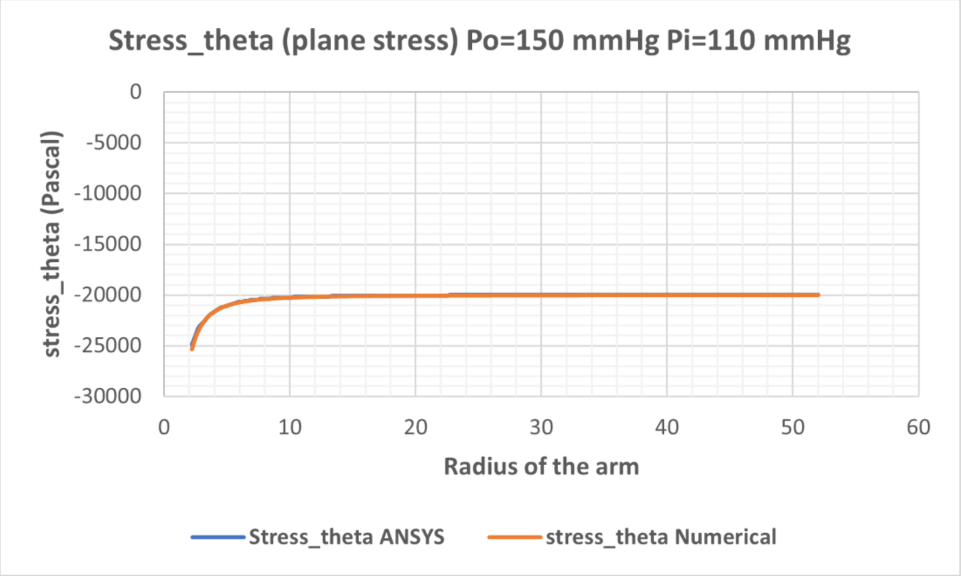

Figure 46 Stress $\tau_{\theta\theta}$ vs radius of the arm (axisymmetric plane stress model)

4.2 Non-linear annular model

In this non-linear analysis, the annular concentric model is solved, conforming to the theory of large deformations. The geometry and the model's material remain the same as assumed in the linear analysis of the annular concentric model, discussed in Section 4.1. The model was simulated in ANSYS with 'large deflection' turned ON for non-linear analysis. The analytical model was solved using a linear isotropic material defined by Young's modulus and Poisson's ratio, as discussed in Section 3.3.1. The model was solved for the plane strain case of the axisymmetric model as it imposes similar boundary conditions on the upper arm model as observed during the BP measurement process. The model's results solved using the FEM in ANSYS are compared with the numerically solved model formulated on the principles of non-linear continuum mechanics in the following section.

4.2.1 Results verification

The non-linear plane strain model was verified against the analytical model for the pressure loads of $P_O = 70\ mmHg, P_I = 50\ mmHg$.

Here, $P_O =$ Cuff pressure, $P_I =$ Blood pressure in the brachial artery.

The displacement u_{rr} is shown in Figure 47.

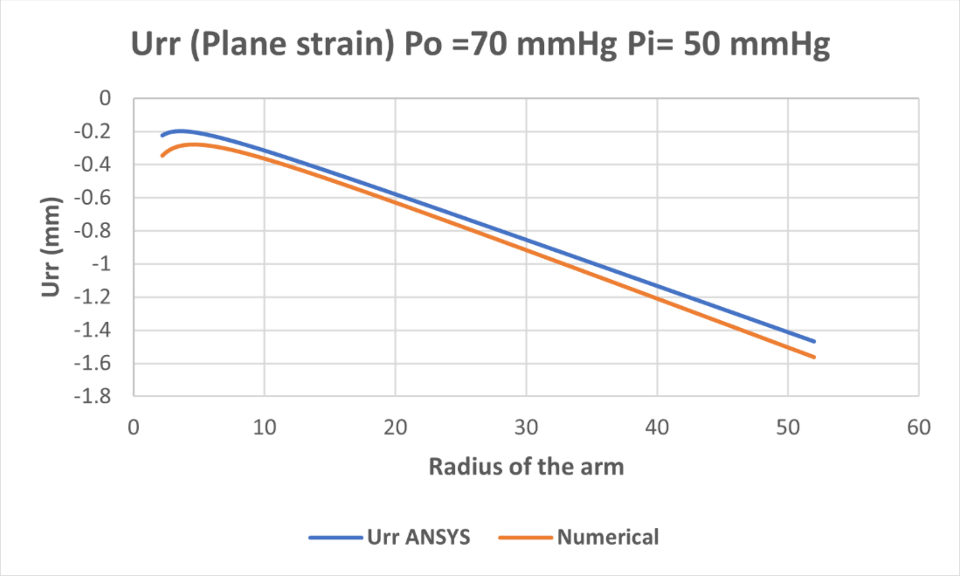

Figure 47 Displacement (u_{rr}) vs. Radius of the arm (non-linear axisymmetric plane strain model)

The strain $'e'$ on the soft tissue in the radial $'rr'$ and circumferential $'\theta\theta'$ Figure 48 and Figure 49, respectively

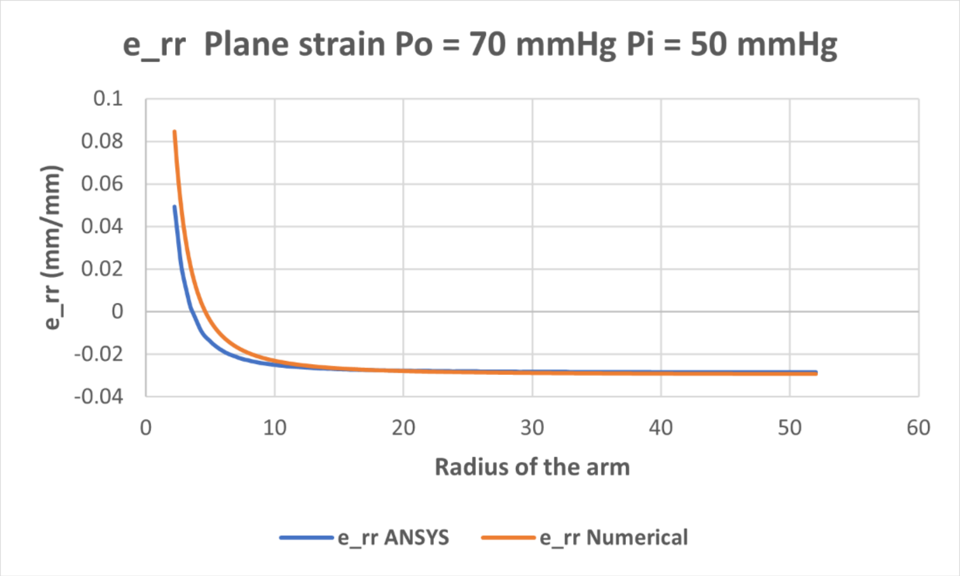

Figure 48 Strain err vs. Radius of the arm (non-linear axisymmetric plane strain model)

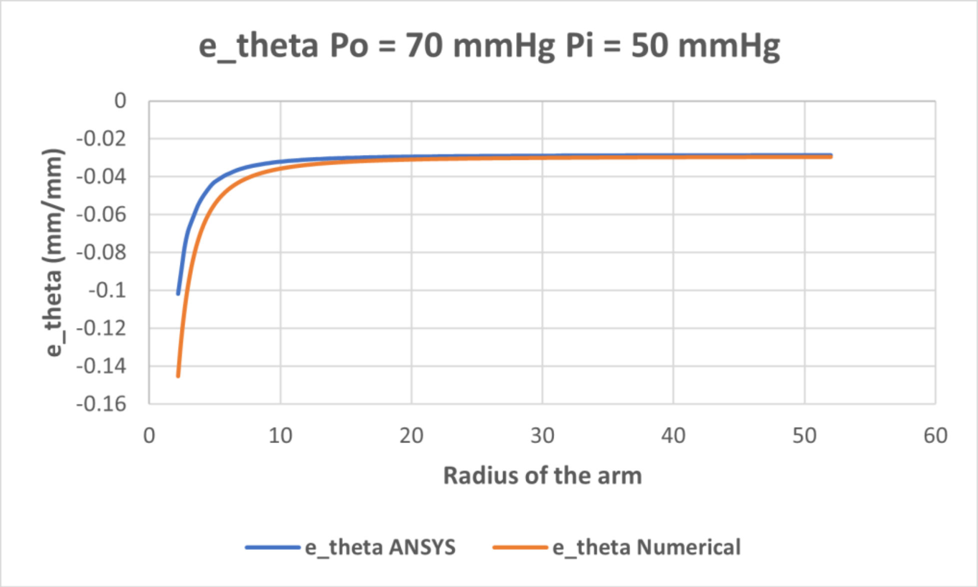

Figure 49 Strain $e\theta\theta$ vs. Radius of the arm (axisymmetric plane strain model)

Th The stresses $\tau_{rr}, \tau_{\theta\theta}$ across the radii of the arm are shown in Figure 50 and Figure 51.

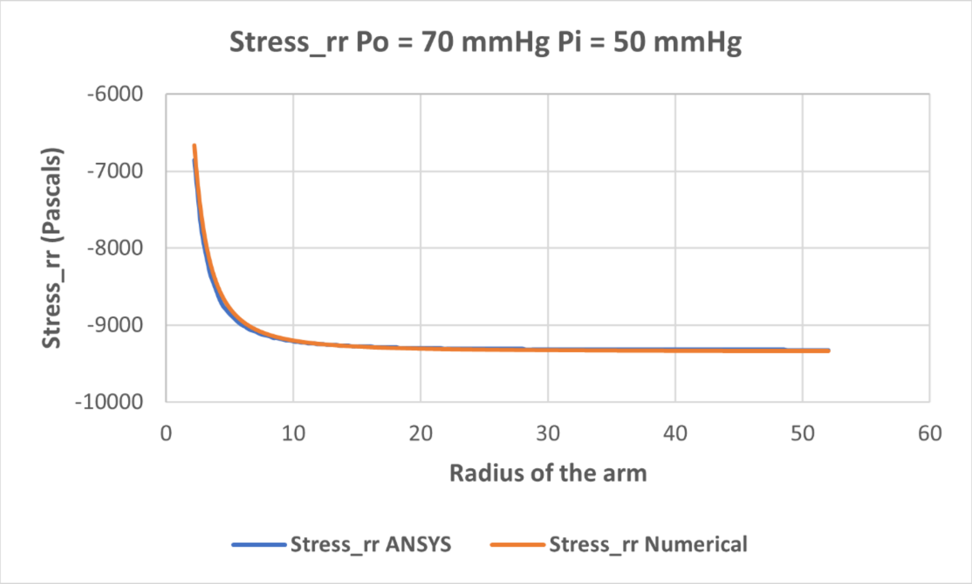

Figure 50 Stress τ_{rr} vs. Radius of the arm (non-linear axisymmetric plane strain model)

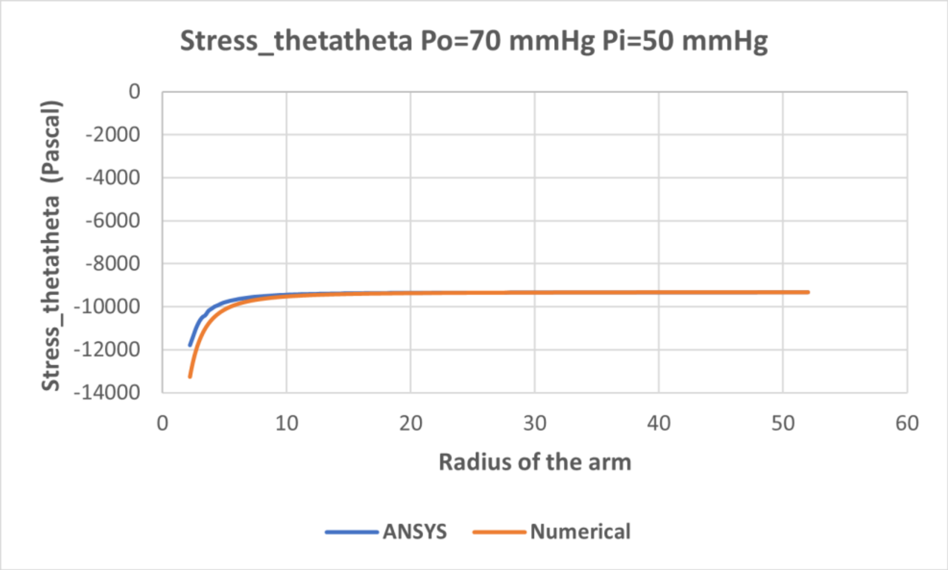

Figure 51 Stress $\tau_{\theta\theta}$ vs. Radius of the arm (axisymmetric plane strain model)

4.2.2 Results Discussion

The non-linear axisymmetric plane strain model is an extension of the axisymmetric plane strain model solved using the theory of large deformations. It accounts for the geometric nonlinearities of the model using a linear isotropic material. This material, also known as the St. Venant-Kirchoff material, fails to solve the model when pressure higher than $70\ mmHg$ is exerted either as BP or CP on the upper arm model. This limitation arises as the volume change for the St. Venant-Kirchoff is not treated appropriately. For small deflections, the volume change is proportional to the strain energy function. The model does not respond suitably to large deformations as the volume shrinks (Hjelmstad, 1996). It is thus essential to account for material non-linearities along with the geometrical non-linearity. A non-linear material defined by hyperelastic constitutive models is suitable for non-linear analysis.

From the results shown above, it can be inferred that the displacement and strains observed in the analytical model and FE model for large deflections are not identical in their magnitudes at the centre of the arm. The results start to match when scoped away from the centre of the arm. The displacements do not match in magnitude but illustrate a similar trend along the radius of the arm. In the analytical model, the displacements of soft tissue for linear and non-linear analyses match well. Moreover, this analysis suggests that the linear isotropic material is incapable of simulating the pressure loads applied during BP measurement with large deflections. Along with geometrical non-linearity, it is critical to model material non-linearity for an analysis using the theory of large deformations.

4.3 Simple cylindrical model

The annular axisymmetric model is further evolved into a simple cylindrical model by introducing the humerus bone and anatomical location of the brachial artery to its geometry. This geometry has been widely used in previous investigations to study the cuff-based NIBP measurement methods (Cristalli et al., 1992), (Ursino & Cristalli, 1996), (Lan et al., 2011). The location of the brachial artery in this study is improved using the data obtained from the Sim4life computational phantoms mentioned summarised in Table 2. Therefore, the simplified geometry is developed to attain equilibrium between accuracy and computational expense. The results obtained using this model are compared to an upper phantom developed by Subburaj (2020) that exhibits the same geometry.

4.3.1 Material model

The upper arm model comprises the brachial artery, soft tissue, and humerus bone. The brachial artery is treated as a cylindrical void with no arterial wall. The SAT layer exhibits invariance concerning its direction suggesting isotropic properties. The muscle and artery tissues exhibit anisotropic properties owing to their fibrous nature (Fung, 1993). Clinical experiments have demonstrated that the muscle tissue exhibit linear isotropic properties under 10% strain (Al-Jumaily et al., 2013). During NIBP measurements, the strain exhibited by the upper arm was shown to be less than 10% (Ursino & Cristalli, 1995). Collectively, the SAT and muscle layers are assumed as one component identified as soft tissue.

A linear isotropic material defined by Young's modulus and Poisson's ratio is used to simulate the soft tissue, as formulated in the annular model. The Young's modulus of the soft tissue is assumed to be 47.5 KPa. Since the upper arm tissues are composed of 75% water, they are assumed nearly incompressible with Poisson's ratio $\nu = 0.45$ (Fung, 1993). The Young's modulus of the bone was reported to be 14-22 GPa (Rahmoun et al., 2020), which is far greater than that of the soft tissue. Hence, the bone is defined by a rigid undeformable material.

4.3.2 Geometry of the model

During cuff-based NIBP measurement, the upper arm is surrounded by a uniform external pressure. The application of this uniform external pressure deforms the upper arm into a cylindrical geometry. Hence, the soft tissue is assumed to be a simple cylinder for a primitive analysis. The upper arm parameters used to formulate the axisymmetric model (refer to Section 4.1) are pursued to formulate this geometry. Anatomically, the shaft of the humerus bone exhibits a cylindrical geometry. Therefore, the humerus bone is assumed to be a simple cylinder. The diameter of the humerus bone is assumed to be 24 mm. The geometry of the model is illustrated in Figure 52.

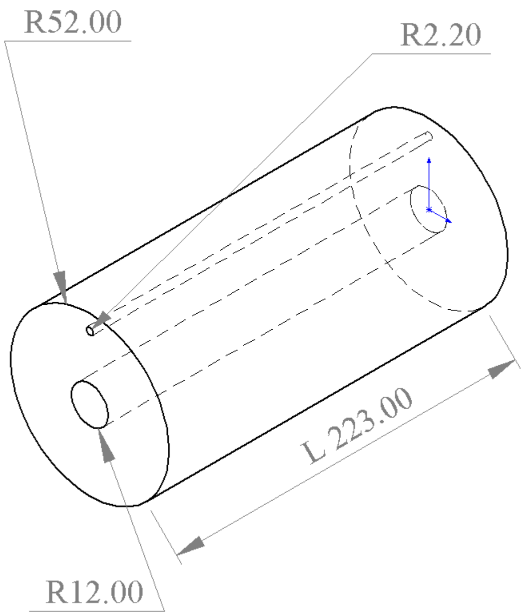

Figure 52 Geometry of the simple cylindrical model in an isometric view

Since there is no relative movement between the humerus bone and muscles, the contact condition is assigned as fixed.

4.3.3 Boundary conditions

The following boundary conditions are imposed on the model:

a) During the BP measurement, the subject's upper arm is duly supported to reduce any potential motion. Thus, the humerus bone is fixed at both ends in a space. Since the soft tissue is bonded to the rigid humerus bone, the bone is excluded from the simulations. Consequently, a fixed boundary condition is applied on the inner surface of the soft tissue.

b) It is assumed that there is no relative movement between the cuff and the upper arm during BP measurement. Thus, the external pressure subjected to the soft tissue deforms it only in the radial plane.

c) The soft tissue is limited at the shoulder and elbow near the proximal and distal ends of the upper arm, respectively. During the BP measurement, the upper arm is amply supported to be constrained in the axial plane. Hence, a frictionless boundary condition is imposed on both ends of the soft tissue during the BP measurement simulation. This boundary condition allows the soft tissue to deform in the radial-circumferential plane only.

4.3.4 Pressure loading

Standard cuff-based NIBP measurement devices exhibit cuff pressure (CP) and internal blood pressure (BP) on the upper arm. In this study, the pressures exerted on the upper arm are assumed to be hydrostatic. There is no pressure loss leading to the application of constant BP. It is assumed that the cuff adheres to the upper arm such that there is no relative motion between the two. Thus, the CP is uniformly distributed on the surface of the arm. Similarly, the BP is applied uniformly on the internal surface of the brachial artery.

4.4 Model mesh

The model was meshed using the same mesh settings and element type used for the axisymmetric models mentioned in Section 4.1.2.2. According to the mesh convergence study (refer to Figure 31), the element size used to mesh the model was 2 mm. The cross-sectional view of the model upon meshing is illustrated in Figure 53. The mesh resulted in a total of 620, 124 elements and 2538634 nodes.

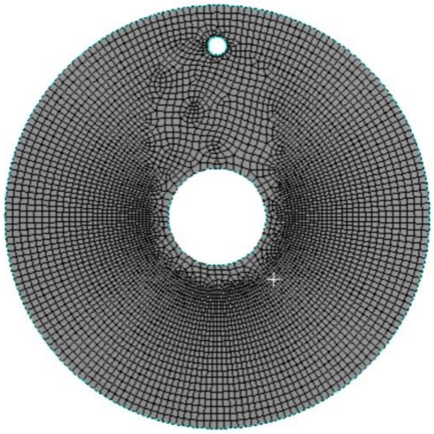

Figure 53 Cross-sectional view of the meshed model.

4.5 BP simulation and analysis for linear deformations

The model was simulated for a CP of 130 $mmHg$ and BP of 80 $mmHg$.

1) Figure 54 illustrates displacement field plot on the soft tissue in radial ‘rr’ plane. A maximum displacement of 1.618 mm in the soft tissue region surrounding the brachial artery. As a result, the diameter of the brachial artery is decreased to 3.1 mm from 4.4 mm. Decreased diameter also suggests shrinkage in volume.

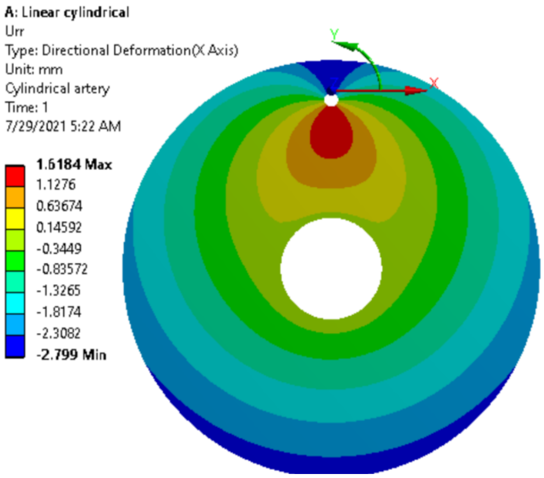

Figure 54 2D displacement field plot on the soft tissue in radial plane

2) Figure 55 shows a 2D strain field plot on the soft tissue in the radial ‘rr’ plane. The maximum strain of 16% occurs at the edges of the brachial artery. As illustrated in Figure, the soft tissue undergoes stretching of 10% near the humerus bone.

3) Figure 56 illustrates a 2D stress field plot on soft tissue in $tangential$ plane. It is evident from the colour scheme that except for the brachial artery region, the soft tissue experiences $CP = 130\ mmHg = 0.01733\ MPa$. The result validates the pressure loading assumption that the CP is exerted radially.

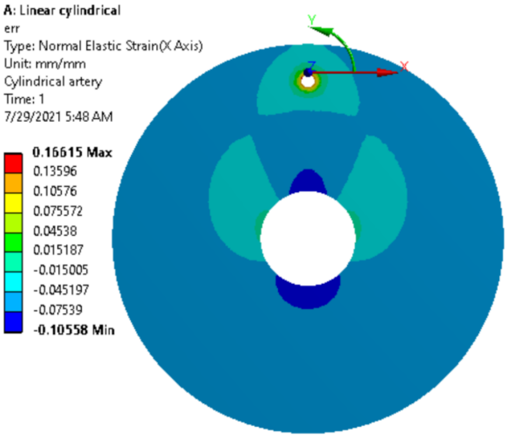

Figure 55 2D strain field plot on soft tissue in radial plane

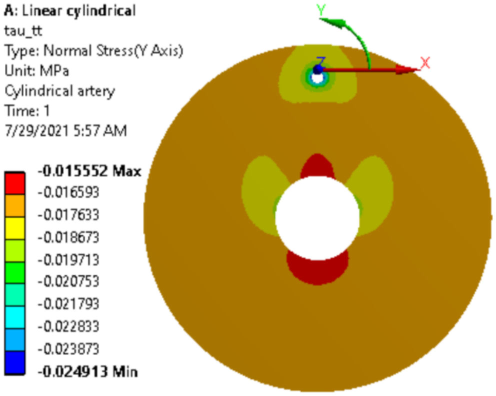

Figure 56 2D stress field plot of soft tissue in tangential plane

To study the effects of a range of loading conditions soft tissue, BP was kept constant at $80\ mmHg$, and CP was applied ranging from $0\ mmHg$ to $140\ mmHg$ at intervals of $20\ mmHg$. The difference between CP and BP is known as Transmural Pressure (TP). The displacements, stresses and, strains for different TP are illustrated below.

1) The maximum and minimum displacements (rr-plane) in the soft tissue for a given range of pressures is shown in Figure 57. The displacements exhibit a similar trend over a range of TP, as illustrated in Figure 54. When the TP is 0, the displacements in the radial plane around the artery are equal and opposite in magnitude. The brachial artery experiences a maximum displacement of 1.3 mm.

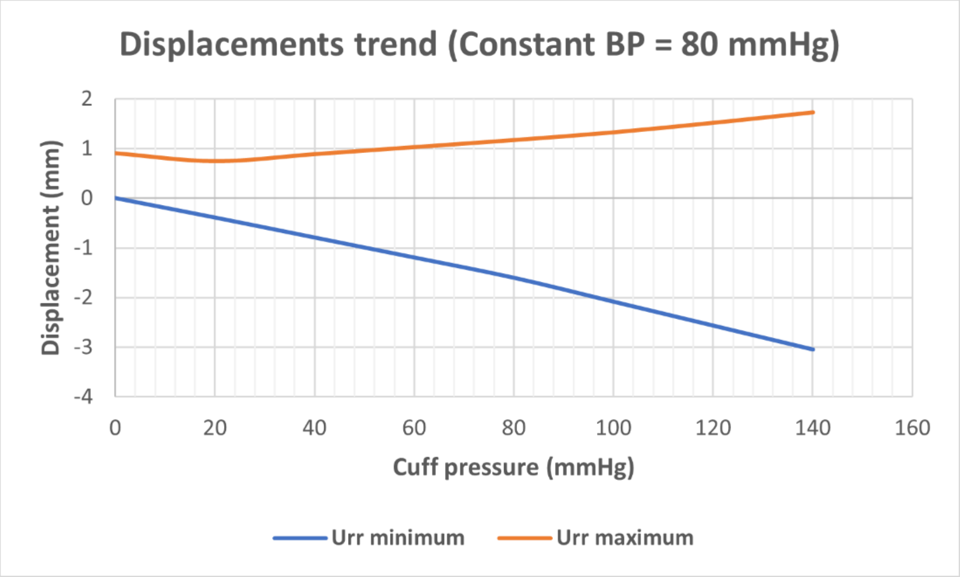

Figure 57 Displacement (Urr) vs CP over a constant BP 80 mmHg

2) The maximum and minimum (here, compression) stresses (rr-plane) induced during pressure loading is illustrated in Figure 58. The trend shows that when CP < BP, the brachial artery experiences negligible compression. As the TP reaches a positive magnitude (Here, > 80 mmHg), the brachial artery undergoes compression. It can be inferred that as the TP increases, the diameter of the brachial artery and thus its volume decreases.

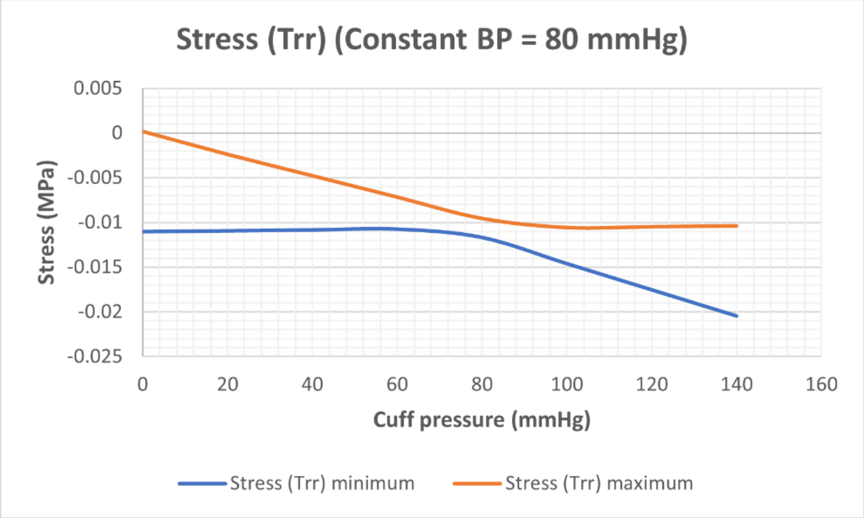

Figure 58 Stresses (Trr) vs CP over a constant BP. 'Stress(Trr)' minimum suggests stress as a result of compression

3) The maximum and minimum strains exerted on the soft tissue due to pressure loading are illustrated in Figure 59. Here, the maximum strain occurs on the brachial artery (refer

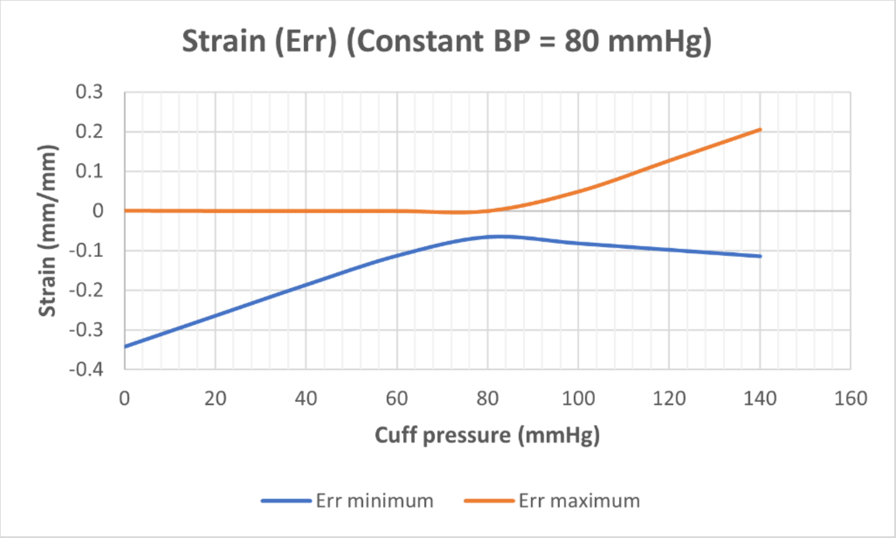

Figure 59 Strain (Err) vs CP over a constant BP.

to Figure 55). When BP > CP, the brachial artery is not subjected to strains in $radial$ plane. The strains show a linear trend with respect to the increasing TP.

The strain energy on the upper arm is illustrated in Figure 60. For this linear analysis, the strain energy during NIBP measurement increases irrespective of the TP. As TP starts to increase, the soft tissue compresses more. Thus, increase in the total strain energy in the soft tissue.

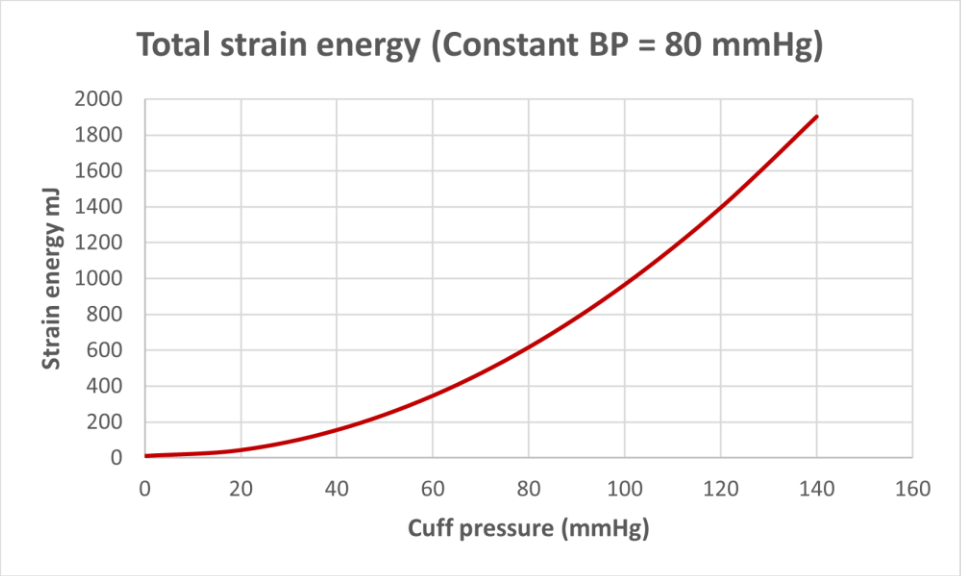

Figure 60 Strain energy vs CP over constant BP 80 mmHg

4.6 Validation

The simple cylindrical model was validated with an upper arm phantom of the same geometry using ultrasound measurements fabricated by Subburaj (2020). The phantom was cast using Platsil-00 gel. The diameter of the brachial artery in the arm phantom was 3.5 mm. In order to validate the model, the diameter of the brachial artery was changed to 3.5 mm in the simulation as well. The ultrasound imaging test to determine the diameter changes of the brachial artery for BP ranging from 20-160 mmHg at intervals of 20 mmHg. A cuff was not imposed on the phantom during the experiment. The Platsil-00 material was not characterised. Hence, Young's modulus was assumed to be 46 KPa. As discussed in Section

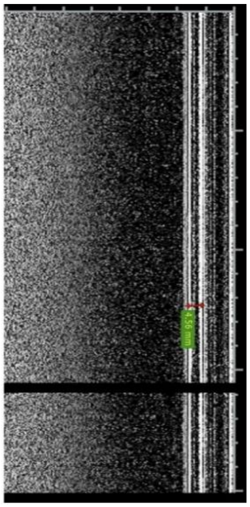

Figure 61 Ultrasound image of the brachial artery

4.2.2, the linear isotropic model fails to solve in a ‘large deflection’ setting for pressures above 70 mmHg. Hence the model was solved assuming small deflections.

The diameter change of the brachial artery using ultrasound imaging and FEA simulation is shown in Figure 61

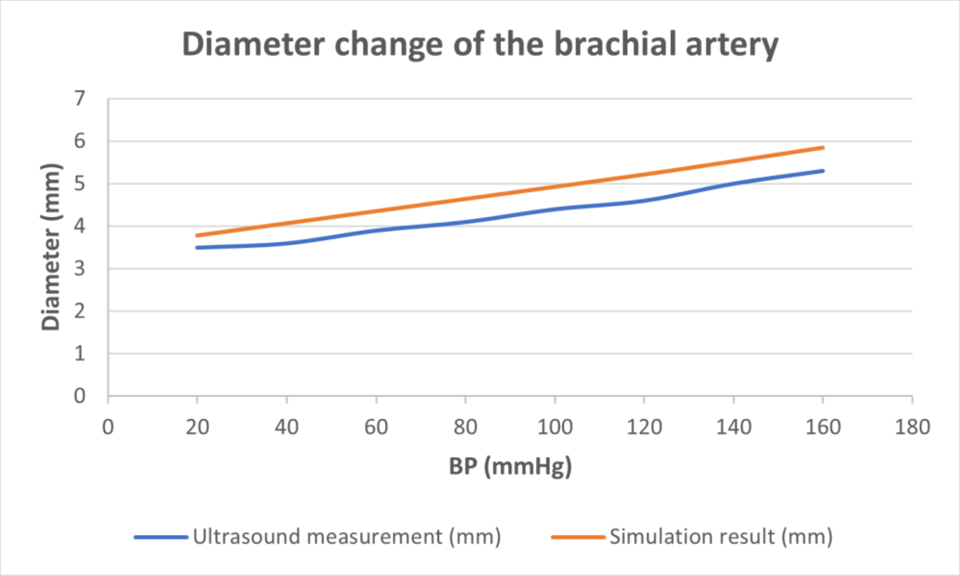

Figure 62 Brachial artery deformation comparison

It is evident from Figure 62 that the deformations of the brachial artery do not match in terms of their magnitude. However, the trend at which the diameter changes for the given pressures is similar. The non-matching magnitudes can be attributed to the isotropic material and the linear analysis to simulate the experiment.

The Platsil-00 material was not available to characterise. It was assumed that Ecoflex-0020 characterised in Chapter 5, has similar mechanical properties as that of Platsil-00. The phantom model was simulated in ANSYS using a Mooney-Rivlin 3 parameter hyperelastic model formulated from the Ecoflex-0020 tensile and compression tests (refer to Section 5.2, Section 5.4, Section 7.1). The model was solved as a non-linear analysis.

Figure 63 illustrates the comparison of the diameter change in the brachial artery using the formulated hyperelastic model. It is evident from Figure 63 that the brachial does not deform linearly as the BP increases. The accuracy of the simulation results was within 6.2% of those of the experimental results. Even though the materials chosen for analysis were different, the results aid in the validation of the cylindrical model

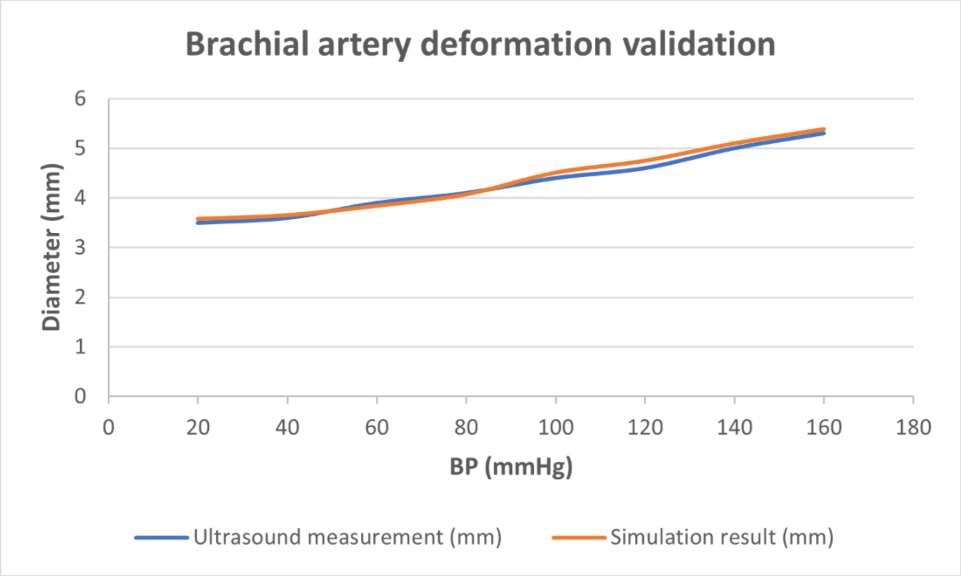

Figure 63 Validation test for the brachial artery deformation

4.7 BP simulation and discussion for non-linear deformations

The hyperelastic material model mentioned above was used to simulate the loading conditions described in Section 4.5 using a non-linear analysis conforming to the theory of large deformations. BP was kept constant at $80\ mmHg$, and CP was applied ranging from $0\ mmHg$ to $140\ mmHg$ at intervals of $20\ mmHg$. The resultant deformations, stresses, and strains produced were analysed.

1) The maximum and minimum displacements (rr-plane) in the soft tissue for a given range of pressures is shown in Fig. The 2D displacement field plot in rr plane in Figure 64 is illustrated for BP $= 80\ mmHg$ and CP $= 130\ mmHg$. It can be inferred that the brachial artery experiences a maximum displacement of 0.3mm as opposed to 1.6 mm seen for the linear analysis. At TP = 0 mmHg, there is no deformation of the soft tissue.

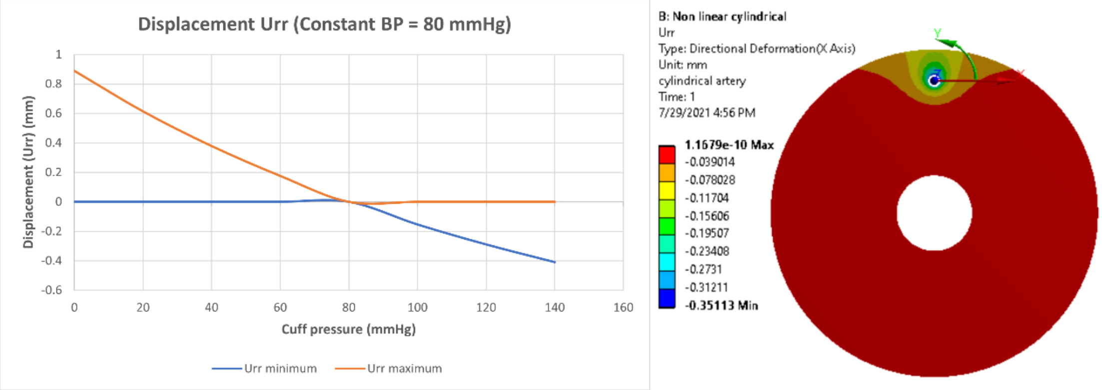

Figure 64 Displacement vs Cuff pressure at constant BP. A 2D displacement field plot for CP = 130 mmHg and BP = 80 mmHg

The displacement of the soft varies near the location of the brachial artery that exerts a BP. Rest of the soft tissue region experiences CP, meaning no deformations. This can be attributed to the incompressibility of the hyperelastic material, of which the Poisson's ratio is close to 0.49. The Poisson's ratio used to formulate the linear isotropic material model is 0.45, which is compressible. Therefore, the deformations vary significantly between the models with linear and non-linear analysis.

2) A similar trend is observed for the stresses and strains induced on the soft tissue since these tensor quantities are derived from displacements. The stress and strain distributions in the radial plane and their 2D field plots are illustrated in Figure 65 and Figure 66, respectively.

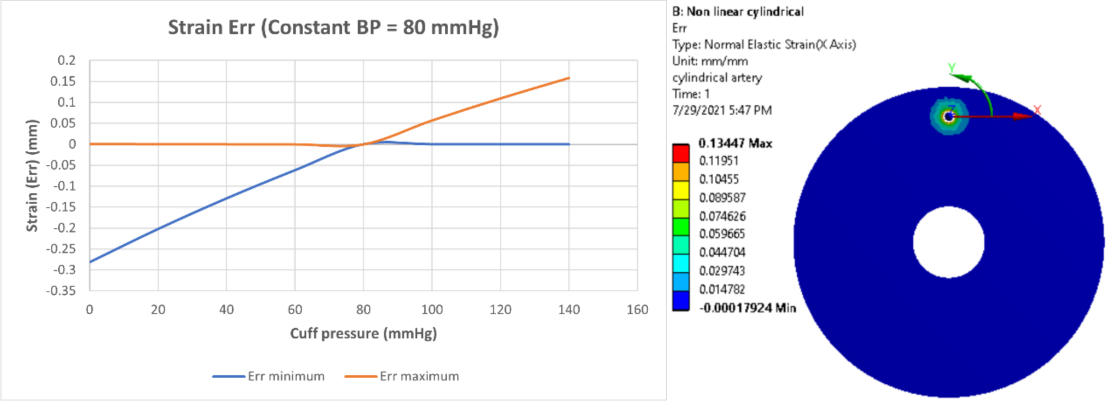

Figure 65 Strain (Err) vs Cuff pressure at constant BP 80 = mmHg. A 2D strain field plot at CP = 130 mmHg

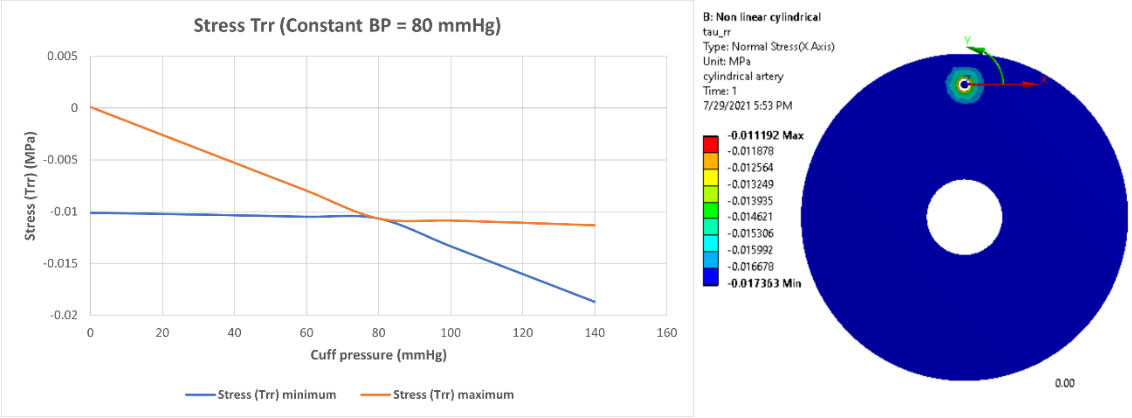

Figure 66 Stress (Trr) vs Cuff pressure at constant BP 80 = mmHg. A 2D stress field plot at CP = 130 mmHg

3) The total strain energy in the upper arm for constant BP over a range of cuff pressures is shown in Figure 67. This analysis's strain energy distribution is different from what was obtained for the linear analysis (refer to Figure 59). The magnitude of the strain energy is much lower as well. This can be attributed to the incompressibility of the hyperelastic material model. With the CP = BP and TP = 0, hydrostatic pressure is created on the system to not be compressed. Hence, the strain energy at this point is 0 mJ.

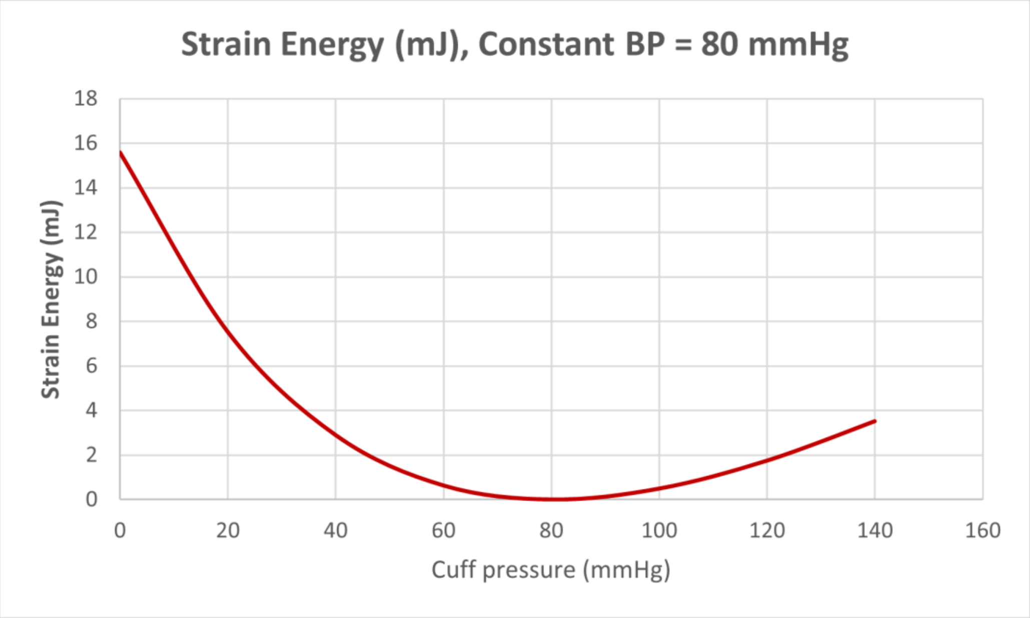

Figure 67 Strain energy vs CP for constant BP 80 mmHg

4.8 Summary

The finite element models were verified using the concentric analytical models derived in Chapter 3. The annular models aided in a primitive understanding of the displacements, stresses, strains, and volume changes on the soft tissue in the polar coordinate system. The concentric models formulated using a linear isotropic material did not solve the geometric nonlinearities of the upper arm concentric models conforming to the large deformation theory. Therefore, the characterisation of materials to emulate the soft tissue is critical. The upper arm model with a simple cylindrical geometry was validated against a phantom of the same geometry. It was observed that the displacement of the brachial artery did not match with the FE simulations attributing to the linear analysis

A Mooney-Rivlin 3 parameter hyperelastic model was formulated from the uniaxial tests of Ecoflex-0020 (Chapter 5). The formulated material model was used to simulate the soft tissue in the simple cylindrical model. The analysis was solved with ‘large deflections’ active in ANSYS. The displacement of the brachial artery obtained using this model matched well with phantom experiments thereby, validating the established upper arm FE model. Furthermore, this upper arm model was simulated for a linear and a non-linear analysis with a wide range of CP, keeping the BP constant. The distribution and magnitude of the displacements, stresses, and strains among these models vary significantly. The strain energy in the soft tissues exhibits a significantly different trend over the range of given pressures. These indifferences can be attributed to the compressibility of the materials used to model the soft tissue. For a linear analysis using the linear isotropic material, Poisson’s ratio is assumed 0.45. In contrast, the formulated hyperelastic model is nearly incompressible, with Poisson’s ratio close to 0.49. It can be inferred that the compressibility of the soft tissue plays a critical role in the estimation of BP using NIBP monitors.

Chapter 5 Material characterisation

This chapter aims to dictate the process of characterisation of materials to develop an upper arm phantom and create a material model for the anatomical FE model. The established material properties serve in the validation of the experimental phantom with the computational phantom. Several materials and their varied compositions were tested, analysed for their mechanical properties. The process of achieving this is discussed in detail in this chapter.

5.1 Potential materials

Based on the literature review in Chapter 2, it is understood that Young's modulus of the soft tissue ranges from 40 KPa – 100 KPa. Apart from the mechanical properties, curing time, feasibility, shelf life, and availability were considered before selecting various materials to determine their suitability in fabricating the upper arm phantom.

From the literature, Silicone proves out to satisfy the conditions required to fabricate the desired phantom. The commercially available Silicone material identified for testing was Smooth-On Ecoflex-0010 and Smooth-On Ecoflex-0020. (Heo et al., 2020) conducted tensile and compression tests on Ecoflex-0010, Ecoflex-0020, Ecoflex-0030. The study focused on creating a fully-defined hyperelastic model from these materials based on the uniaxial, biaxial and shear tests. Based on the tensile tests, it was identified that the Elastic modulus of Ecoflex-0010 and Ecoflex-0020 ranges from 30 – 60 KPa. The shore hardness (0010, 0020, 0030) of the Ecoflex material indicates its stiffness. Higher shore hardness reflects higher stiffness of the material. The Ecoflex material is available as a two-part mixture. The supplier recommendation is a 1:1 mixture of both parts to obtain a final product for moulding.

The materials were characterised for their mechanical properties using 'TA. XT+ Texture Analyser – Stable Micro Systems' and Exponent software version 6.1.4.0. Tensile ring tests conforming to ISO 37 standard for rubbers were adopted to determine the stress-strain relationship of the materials under tension. Compression tests conforming to ISO 7743 standard for rubbers were adopted to determine the stress-strain relationship of the materials under compression.

5.2 Preliminary tensile ring test

As per the guidelines provided by ISO 37:2017 (2017), type A rings and their standard pulleys were fabricated using the 3D printing technique as per ISO 23529:2016 (2016) . The dimensions for the pulleys are:

$$d_1 = 25.5\,mm \quad d_2 = 29\,mm$$

$$L = 30\,mm \quad A = 5.6\,mm$$

The standard type A ring test sample has an internal diameter of 44.6 mm. The axial thickness and radial width of the test sample are 4mm. Figure 68 represents the arrangement of the pulleys for the tensile ring tests. Moulds for casting the rings and pulleys were 3D printed, as shown in Figure 69 and Figure 70, respectively. As per the guidelines, three test pieces of the materials were tested.

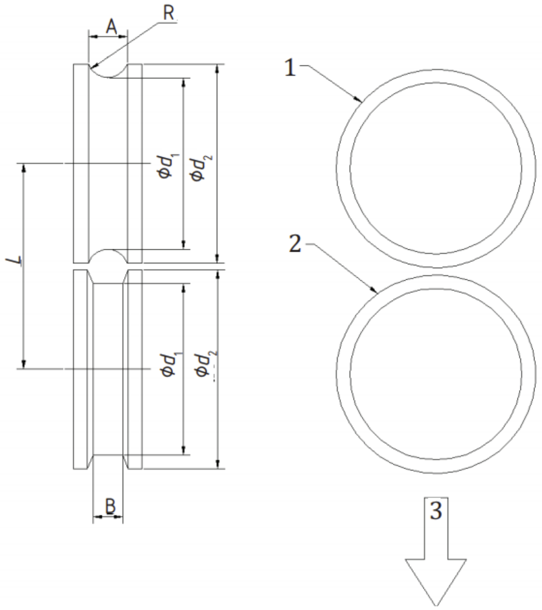

Figure 68 Illustration of Pulley dimensions. 1: Fixed pulley. 2: Rotating pulley. 3: Direction of extension (ISO 37:2017, 2017)

Figure 69 3D printed Moulds for ring specimens

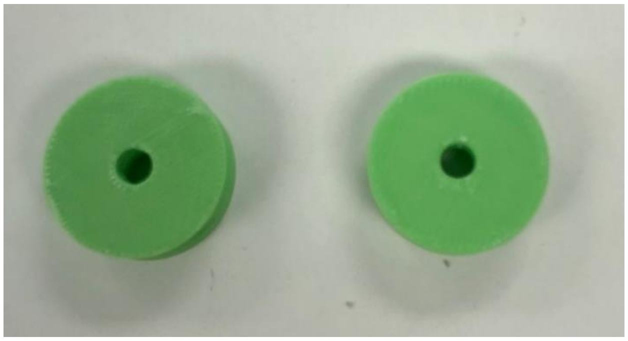

Figure 70 3D printed pulleys as per ISO 7743:2017 (2017)guidelines

Before setting up the test rig, the Texture Analyser was calibrated for forces and height as per the guidelines. To calibrate the force on the machine, a load cell of 730 grams was located at the top of the calibration ring, and the weight of the load cell was set using the Exponent software, as illustrated in Figure 71

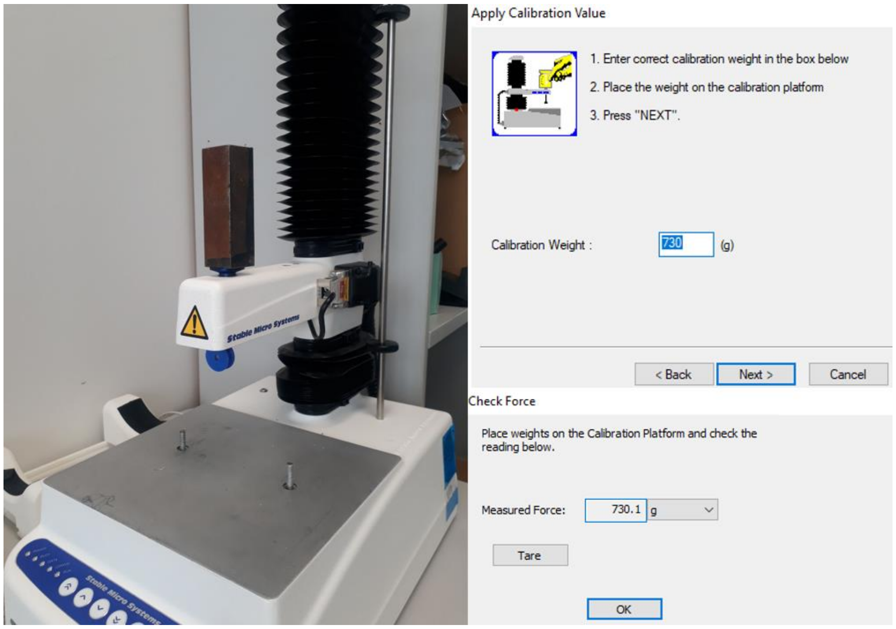

Apply Calibration Value

1. Enter correct calibration weight in the box below
2. Place the weight on the calibration platform
3. Press "NEXT".

Calibration Weight : 730 (g)

Check Force

Place weights on the Calibration Platform and check the reading below.

Measured Force: 730.1 g

Figure 71 Force calibration of Texture Analyser

Upon calibration, the test rig was set up on the Texture Analyser, as shown in the Figure. The tensile ring test was first performed on Ecoflex 0020, as shown in Figure 72. The test was conducted on three different samples. The test samples were cast from the same pour of the mixture to achieve consistent results. The mixture was thoroughly mixed and vacuumed to eliminate potential air bubbles before pouring it into the mould. Before recording the actual tests, the samples were loaded cyclically to eliminate unwanted viscoelastic effects like hysteresis.

The test was conducted on three samples in the same calibration setting of the machine. The test incorporated cyclic loading of the samples 3 times for a distance of 100 mm. These test results were averaged, and the Force vs Distance data (see Figure 73) was converted into Stress vs Strain relationship using the following formulae outlined in the ISO 37:2017 (2017) handbook.

The tensile stress, δ_y (MPa) is calculated using the equation:

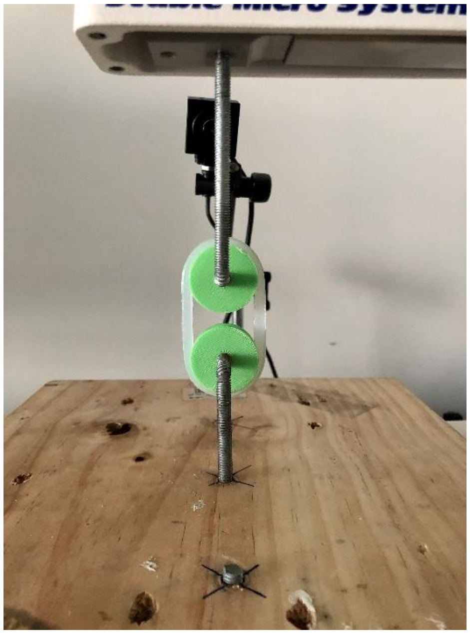

Figure 72 Tensile test setup on Texture Analyser

$$\boldsymbol{\delta_y = \frac{F_y}{2Wt}} \qquad (\mathbf{5.1})$$

Here, F_y is the force, W is the width of the ring sample, t is the thickness of the ring sample.

The elongation ε_y, which is essentially the strain (%) is calculated using:

$$\boldsymbol{\varepsilon_y = \frac{100(\pi d_1 + 2L_y - C_i)}{C_m}} \qquad (5.2)$$

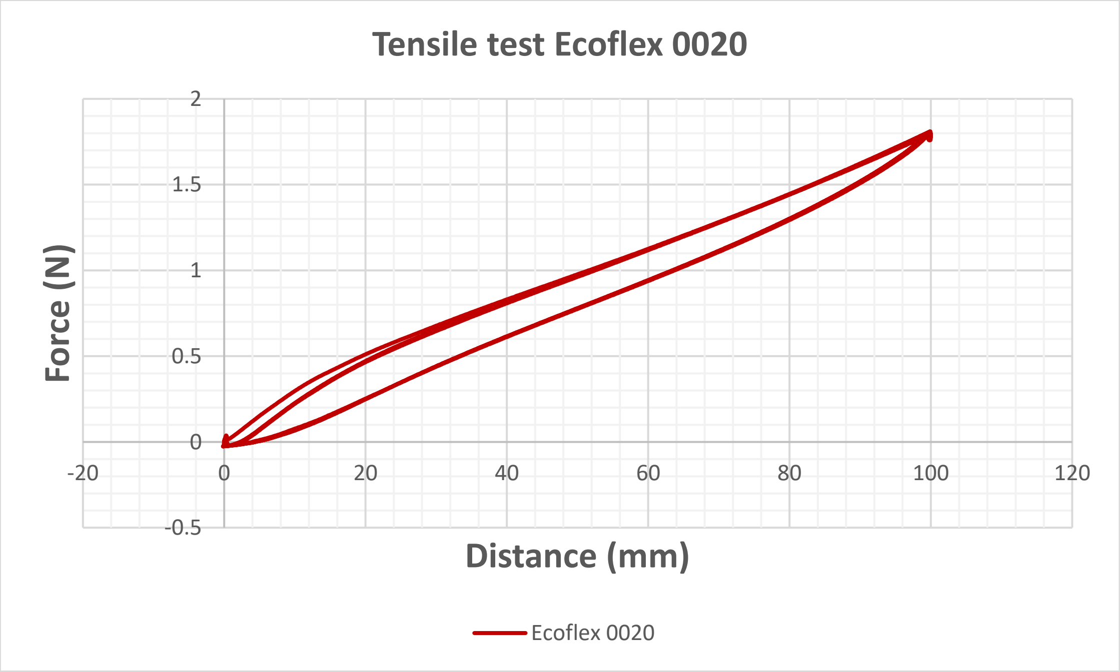

Figure 73 Tensile test of Ecoflex-0020

Where, L_y is the distance between the pullies at yield, C_i is the internal circumference of the ring, C_m is the mean circumference of the ring, d_1 is the diameter of the pulley.

Using the equations (5.1 and 5.2), the tensile stress-strain relationship was obtained for Ecoflex-0020. The Young's modulus $E, in\ this\ case$, is given by:

$$\boldsymbol{E = \frac{\delta_y}{\varepsilon_y}} \tag{5.3}$$

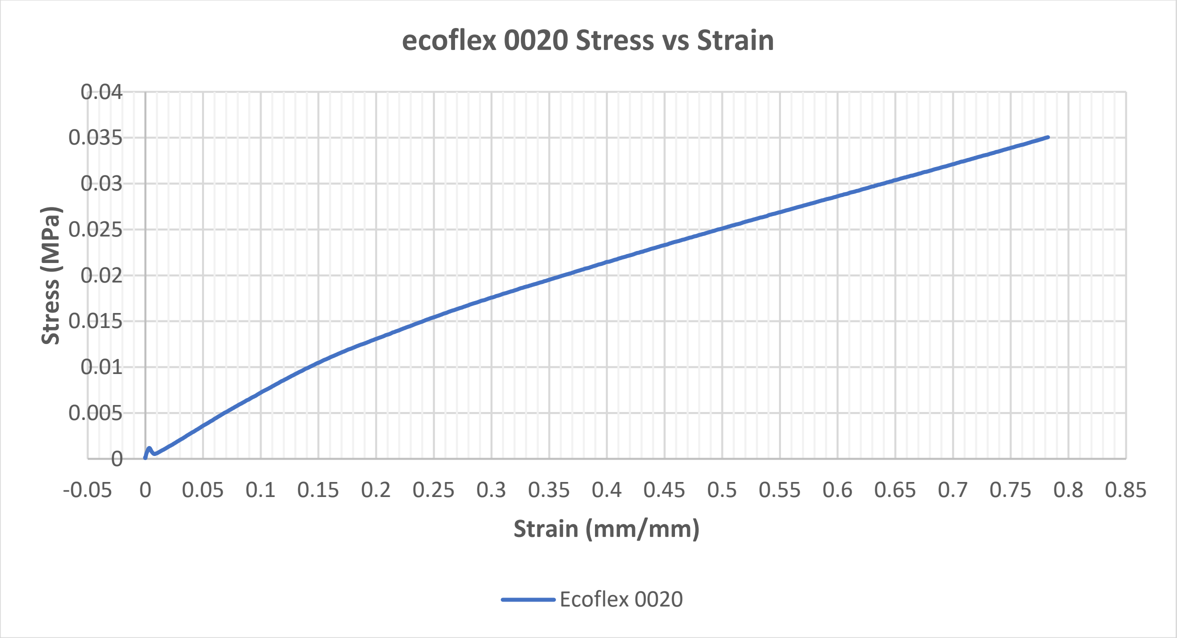

Figure 74 Stress vs Strain curve of Ecoflex-0020 under tensile loading

Young's modulus is valid for materials that have linear stress–stress relationship. The tested materials are hyperelastic. To calculate Young's modulus, the stress-strain relationship was analysed at the beginning of the trend at which the material behaves linearly. A previous study reported that the strain exerted on the upper arm soft tissues during NIBP measurement is under 10% (Al-Jumaily et al., 2013). Thus, Young's modulus for Ecoflex-0020 under 10 % strain is 72 KPa (refer to Figure 74).

5.2.1 Discussion

The elastic modulus obtained from the tensile test of Ecoflex-0020 stands out as a valid reference point in determining the mechanical characteristics. However, the material is hyperelastic, meaning the stress-strain relationship is non-linear. This non-linear behaviour of the material can be observed at the beginning of the graph in Figure 74. The loading-unloading curve of the material exhibits hysteresis owing to its hyperelasticity and subsequent loss of energy. Similar tensile testing on a range of materials is required to be conducted to establish a reference point for their mechanical properties.

5.3 Tensile tests of Ecoflex range

The Young's modulus of Ecoflex-0020 under a 10% strain range is close to 72 KPa. It is desirable to explore softer materials that exhibit Young's modulus close to 47.5 KPa, as used to model the isotropic soft tissue material. Throughout Ecoflex's range of materials, the supplier recommendation of the mixture is 1:1. In a quest of exploring various materials, the recommended mixing ratio of Ecoflex-0020 was tuned. Ring samples of Ecoflex-0020 with a varied ratio of the mixture were cast. The cast samples were cured homogenously despite being composed of different mixing ratios. It was observed that the Part A mixture of Ecoflex is the stiffening component. Along with the 1:1 (Part A: Part B) ratio, samples of 1A:2B and 1A:3B were tested using the same procedure and specifications as mentioned in section 5.2. The Force – Distance graph is represented in Figure 75.

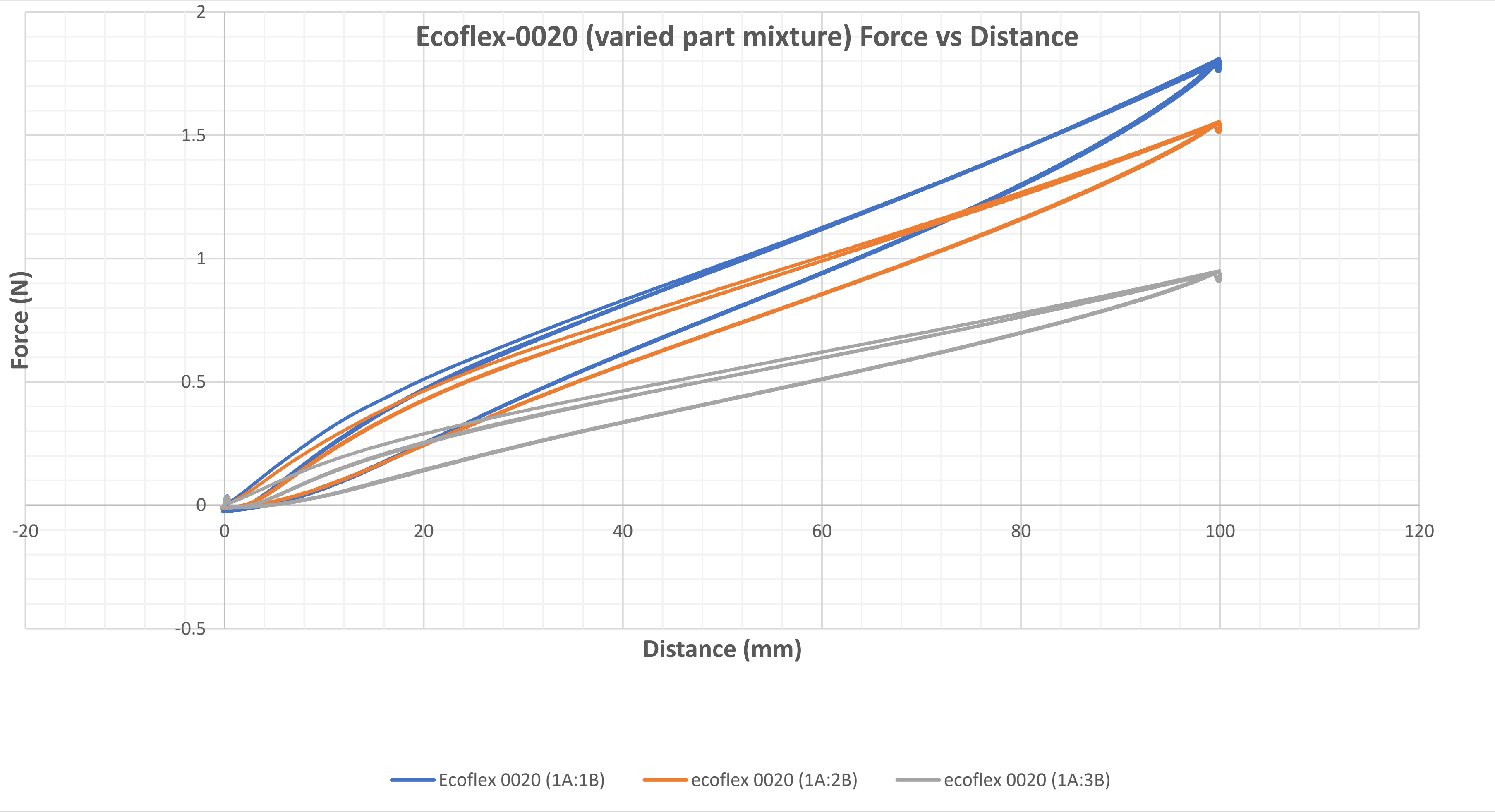

Figure 75 Tensile tests of Ecoflex-0020 (1A:1B), Ecoflex-0020 (1A:2B), Ecoflex-0020 (1A:3B)

From the conducted tests illustrated in Figure 76, it is evident that the elastic response of the material is different when its composition is changed. As the Part B mixture increases, the force required to pull the ring sample for the given distance reduces. From the obtained Force – Distance data, the Stress-Strain relationship and the subsequent Elastic modulus was derived using equations (5.1, 5.2, 5.3).

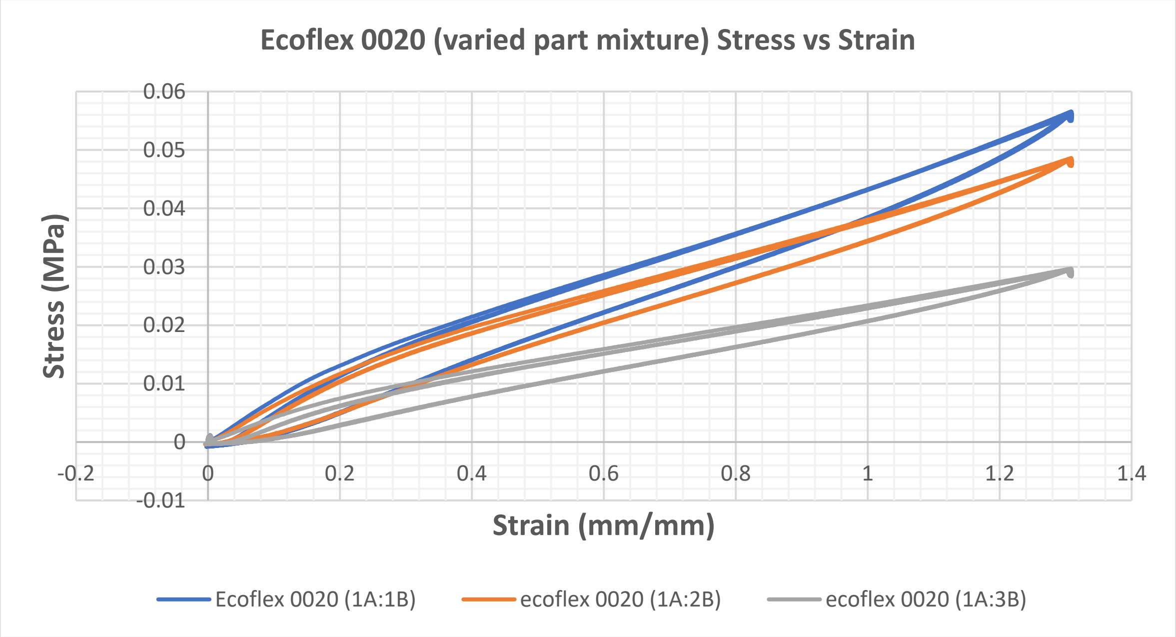

Figure 76 Stress vs Strain curves of Ecoflex-0020 (1A:1B), Ecoflex-0020 (1A:2B), Ecoflex-0020 (1A:3B) under tensile loading

The linear portion and the working strain range was analysed to determine Young's modulus of the tested mixtures. It is illustrated in Figure 77.

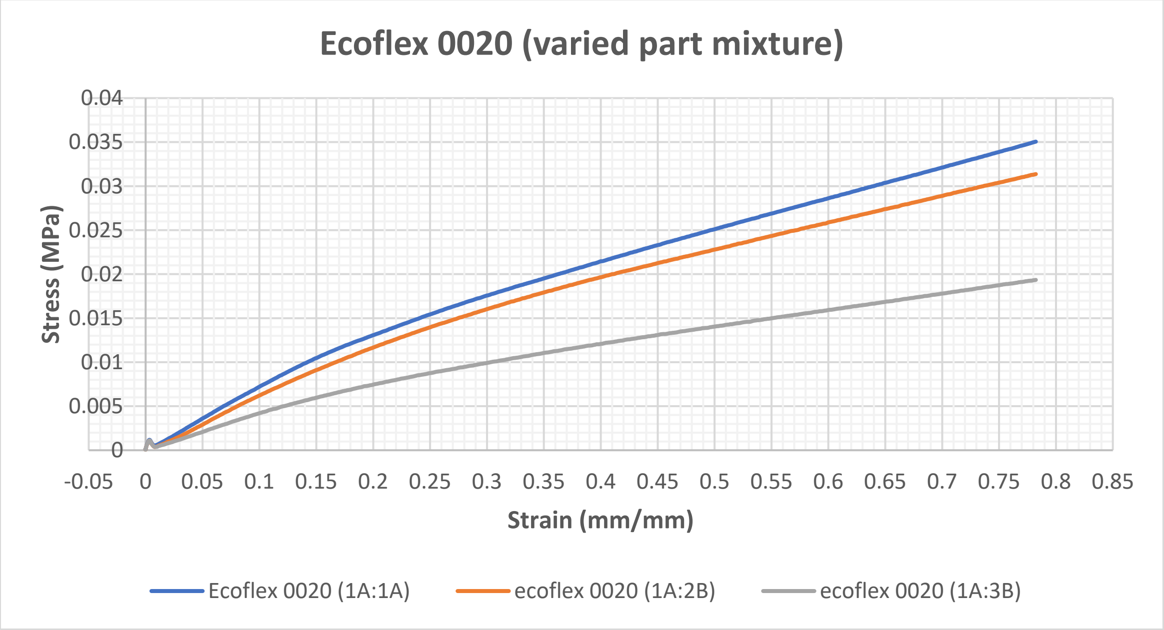

Figure 77 Stress vs Strain relationship of Ecoflex-0020 (1A:1B), Ecoflex-0020 (1A:2B), Ecoflex-0020 (1A:3B) for working strain range under tensile loading

Following the linear approximation, Young's modulus of Ecoflex-0020 (1A:1B), Ecoflex-0020 (1A:2B), Ecoflex-0020 (1A:3B) for tensile loading was inferred to be 49 KPa, 44.3 KPa, 27.3 KPa, respectively.

5.3.1 Discussion

As analysed in Chapter 4, the upper arm phantom is expected to experience deformations due to compression rather than tensile loading. Therefore, it is critical to test the mechanical properties of Ecoflex using compression tests along with tensile tests. To summarise:

a) The mechanical properties of Ecoflex are required to be characterised using uniaxial compression tests.

b) It is required to establish a reference point of mechanical properties under uniaxial loading for Ecoflex's range of materials.

5.4 Compression tests

Compression tests conforming to ISO 7743:2017 (2017) were conducted on the selected materials as illustrated in Figure 78. The test involves compressing a sample piece at a constant strain rate between two plates until a pre-determined strain is achieved. The cast test samples were a cylinder of diameter 29 mm and height 13 mm. The machine was calibrated using the protocols mentioned in Section 5.2. The strain rate used to perform the experiments was 1mm/sec. Three samples of each Ecoflex mixture were tested in the same setting of the machine to achieve consistency in the results. The Force vs Distance data of the compression tests is shown in Figure 79.

Figure 78 Compression test set up on Texture Analyser

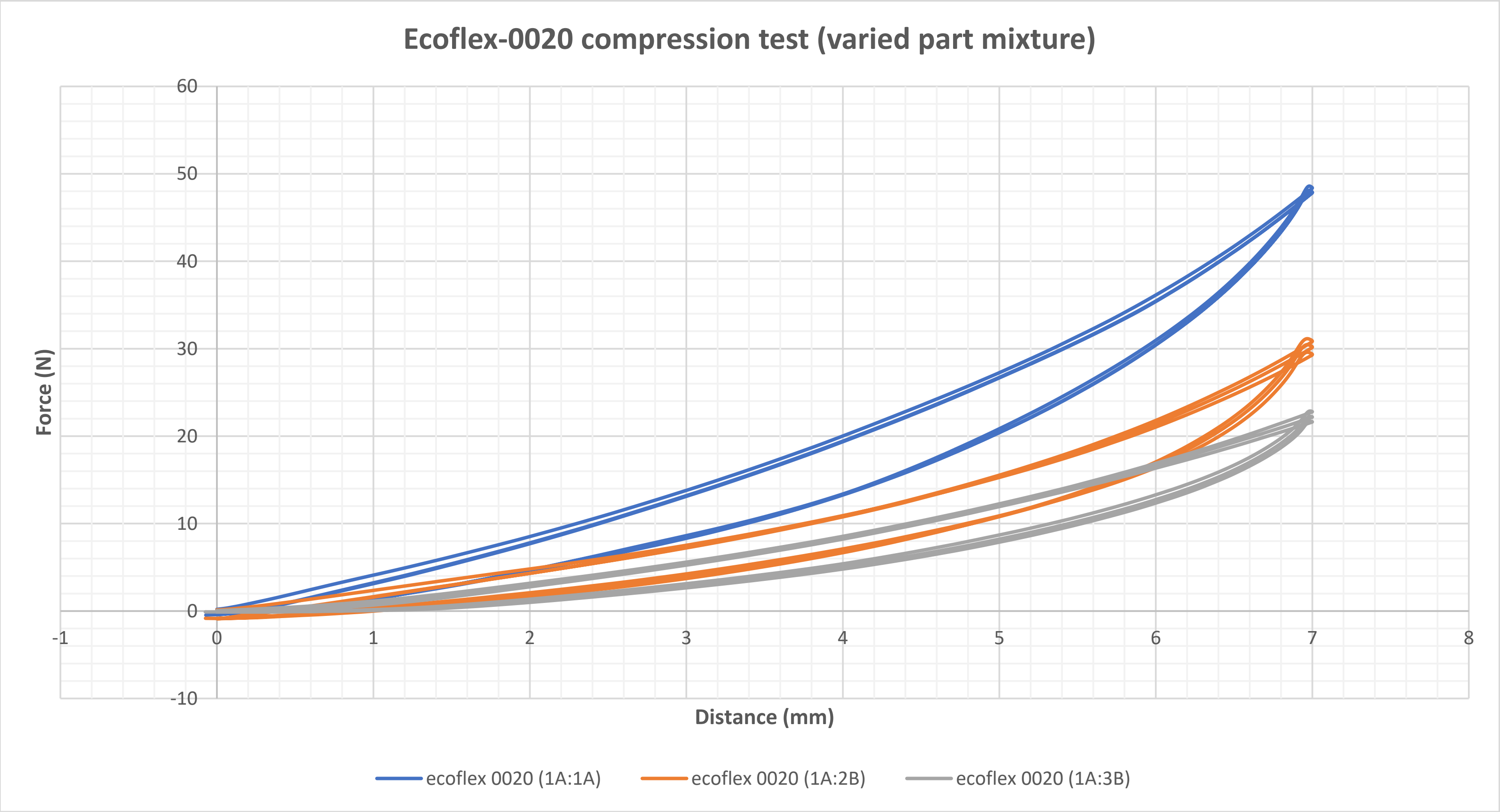

Figure 79 Force vs Distance curves of Ecoflex-0020 (1A:1B), Ecoflex-0020 (1A:2B), Ecoflex-0020 (1A:3B) under compressive loading

The Force vs Distance data was converted into a Stress vs Strain relationship using the following formulae outlined in the (7743:2017, 2017). The tensile stress $\delta_y\,(MPa)$ is calculated using the equation:

$$\boldsymbol{\delta_y = \frac{F_y}{\pi r^2}} \quad (5.4)$$

Here, F_y is the force, r is the radius of the cross-sectional area of the sample.

The elongation ε_y, which is essentially the strain (%) is calculated using:

$$\boldsymbol{\varepsilon_y = \frac{\Delta L}{L}} \quad (5.5)$$

The stress-strain relationship obtained is illustrated in Figure 80.

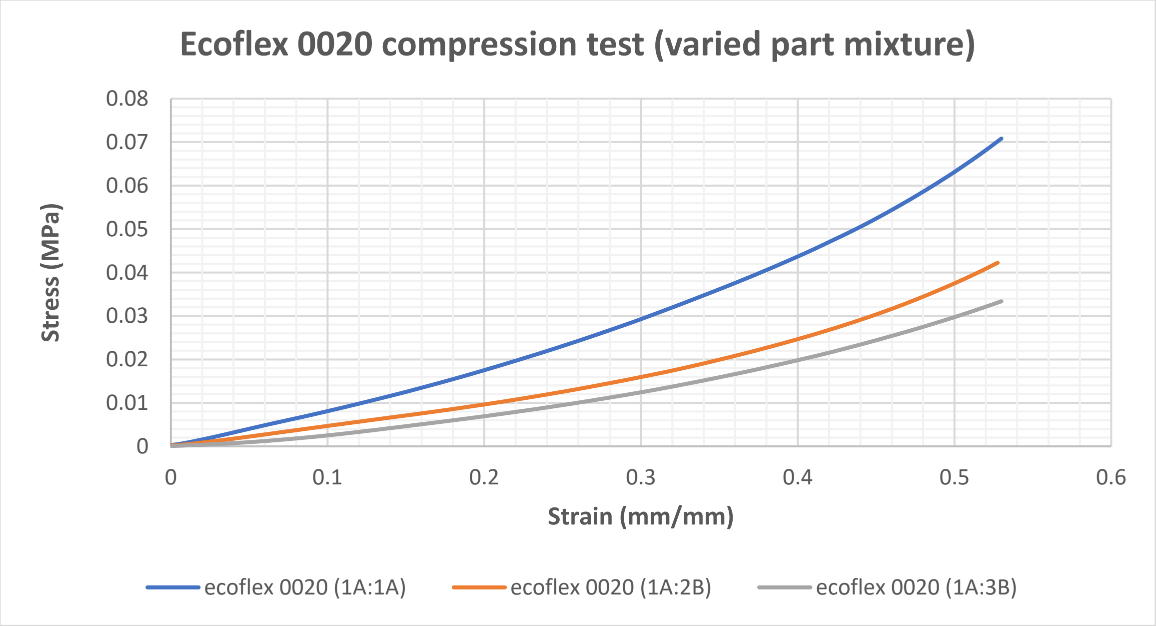

Figure 80 Stress vs Strain relationship of Ecoflex-0020 (1A:1B), Ecoflex-0020 (1A:2B), Ecoflex-0020 (1A:3B) for working strain range under compression loading

From the formulations derived in Chapter 3, it is inferred that the model experiences compressive strains ranging up to 40%. Considering this working range and assuming a linear stress-stress relationship, the obtained Young's modulus was:

E = 88 KPa (Ecoflex-0020 1A:1B), E = 63.6 KPa (Ecoflex-0020 1A:2B), E = 51.7 KPa (Ecoflex-0020 1A:3B).

5.5 Discussion

The tuning of the part mixture of Ecolfex-0020 led to materials that exhibit different mechanical responses than that of the supplier’s recommended mixture. It is demonstrated from the tensile and compression tests that the proportion of part B Ecoflex mixture increases or decreases its elastic modulus as desired. From the numerical formulations, the upper arm is expected to experience deformation due to compression. Therefore, the material's elastic modulus during compression loading is set as the parameter for modelling and fabricating the upper arm phantom.

Ecoflex-0020 (1A:3B) exhibits the mechanical characteristics as desired for this study. The test samples of this mixture demonstrated no signs of incomplete curing or potential discrepancies. However, the size of the upper arm phantom is expected to be much larger than the examined samples. It is a potential risk that the material does not cure when desired to be used in larger applications. The risk of wastage of resources and interruption in the timeline of this study is increased.

The Young’s modulus of Ecoflex-0020 (1A:3B) is observed to be lower than that of Ecoflex-0020 (1A:1B). Ecoflex of lower shore hardness is expected to exhibit a similar mechanical response as Ecoflex-0020 (1A:3B). Abiding by the supplier’s recommended ratio of the mixture reduces potential risks. Hence, the mechanical characterisation of Ecoflex-0010 using tensile and compression tests were undertaken.

5.6 Characterisation of Ecoflex-0010

Tensile and Compression tests were conducted on Ecoflex-0010 using the same protocols mentioned in Section 5.2 and Section 5.4. The force-distance data of the tensile and compression tests were converted into stress-strain relationships using equations (5.1 – 5.5). The tensile test results are illustrated and compared with the previous tests in Figure 81. The compression test results are illustrated and compared with the previous tests in Figure 82.

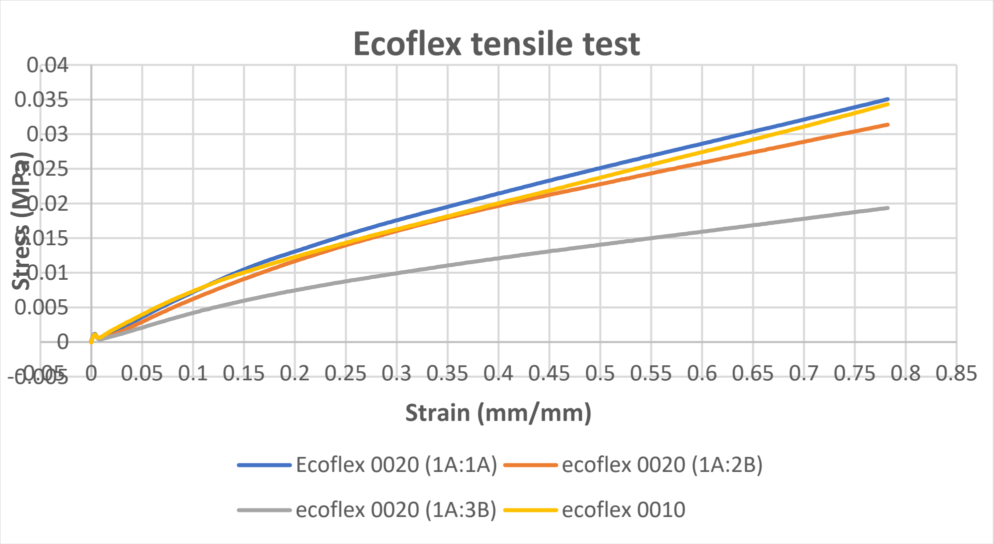

Figure 81 Stress vs Strain curves comparison of Ecoflex-0020 and Ecoflex-0010 under tensile loading

From the Fig and Fig, it can be inferred that the stress-strain response of Ecoflex-0010 is similar to that of Ecoflex-0020 (1A:3B) under compression loading as opposed to tensile loading. Using the linear assumption, Young's modulus of Ecoflex-0010 obtained under tension and compression was 40.5 KPa and 53.9 KPa, respectively.

The determination of Young's modulus was obtained using a linear approximation of the stress-strain curve at the expected working range of the material. For hyperelastic materials, the stress-strain relationship is not linear. Thus, Young's modulus is not constant across the operating strain range. The mechanical response of the materials is further analysed in Section 5.7.

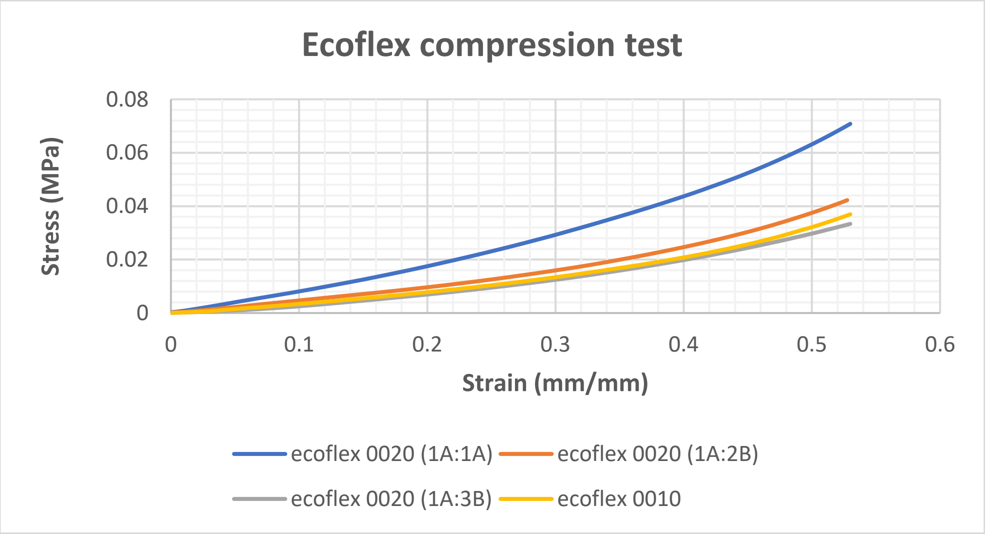

Figure 82 Stress vs Strain curves comparison of Ecoflex-0020 and Ecoflex-0010 under compression loading

5.7 Analysis and conclusion

In this section, the tensile and compression tests of Ecoflex materials are analysed to determine their Young's modulus over the strain range. The stress-strain data were analysed using the central finite difference coefficient method. The method allows for an approximation of the derivative to an order of accuracy that seemed likely to eliminate the noise in the data. The central finite difference is given by:

$$f'(x_i) = \frac{f(x_i+1)-f(x_i-1)}{2\Delta x}$$

Where, x_i is the point of interest, $\Delta\mathbf{x}$ is the step size, $x_i + 1$ is the point of interest plus step size. The accuracy of order 4 was used to analyse the stress-strain curves. The Fig demonstrates the results obtained in terms of Young's modulus vs strain for tensile and compression tests. It was thought that using multiple points helps in eliminating the noise in the data. However, the method did not work. In another approach, the tensile test stress-strain data was analysed using a fourth-order polynomial function using MATLAB. The results are illustrated in Figure 83.

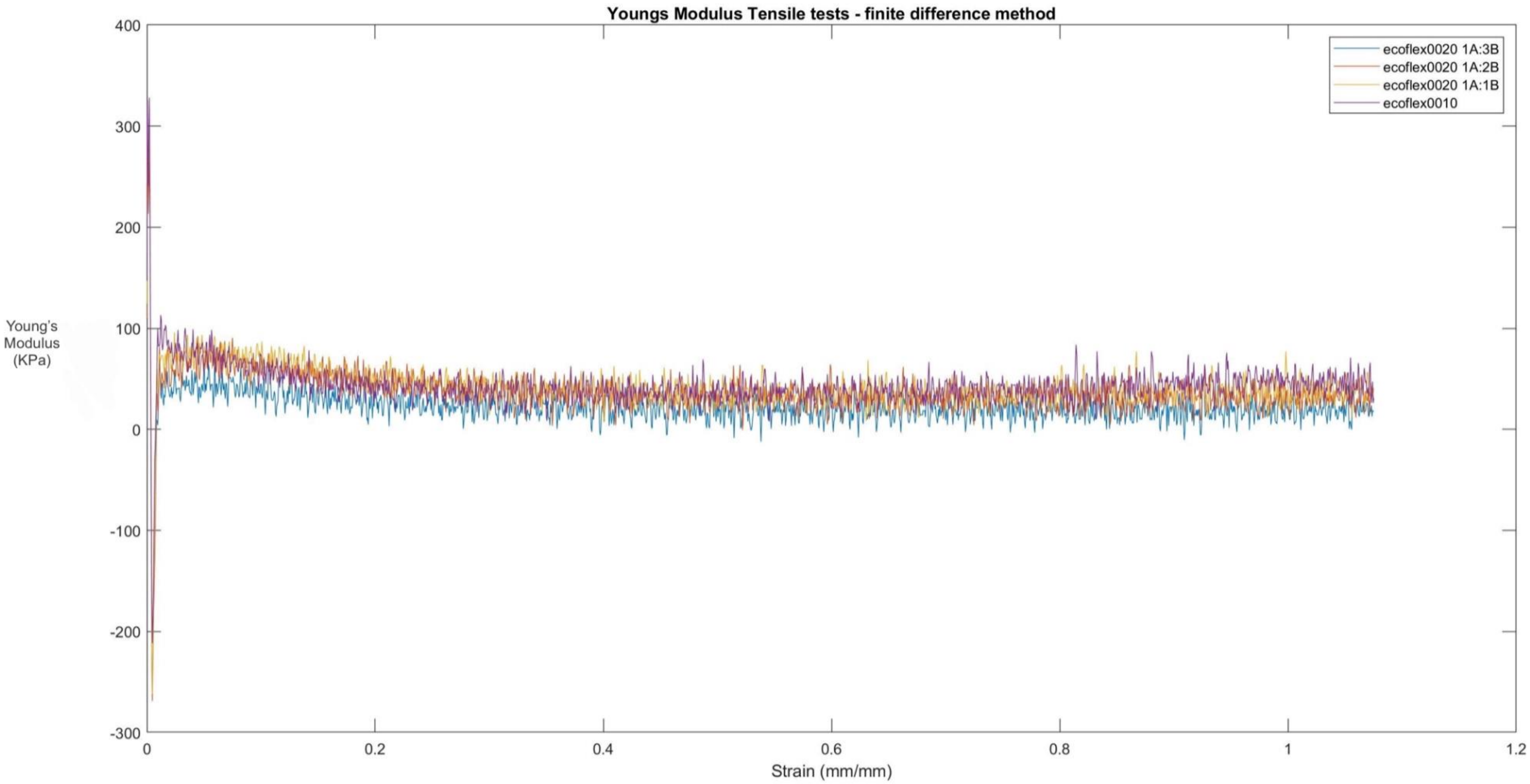

Figure 83 Young's Modulus vs Strain of tensile tests using central finite difference method

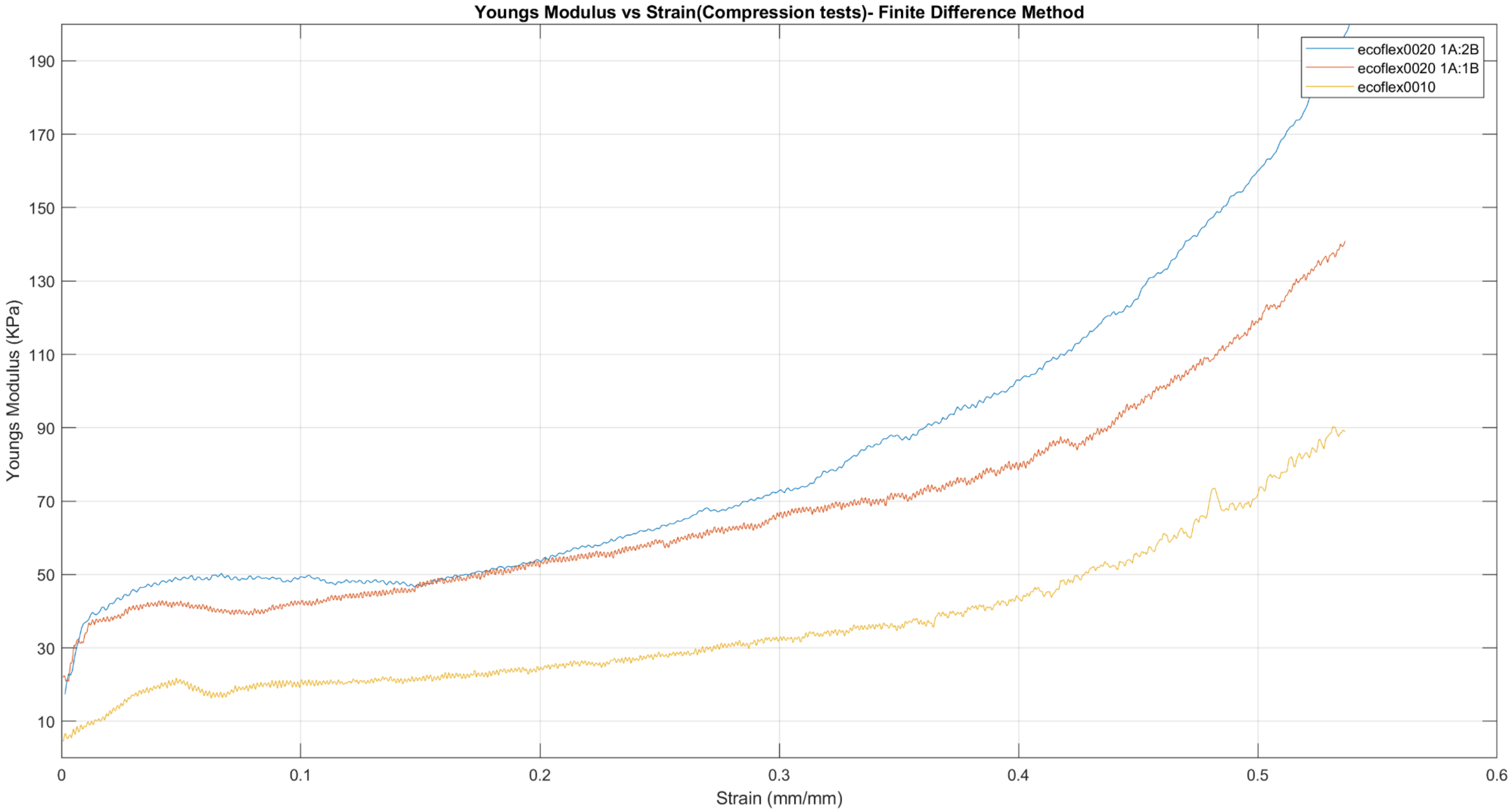

Figure 84 Young's modulus vs Strain of compression tests using central finite difference method

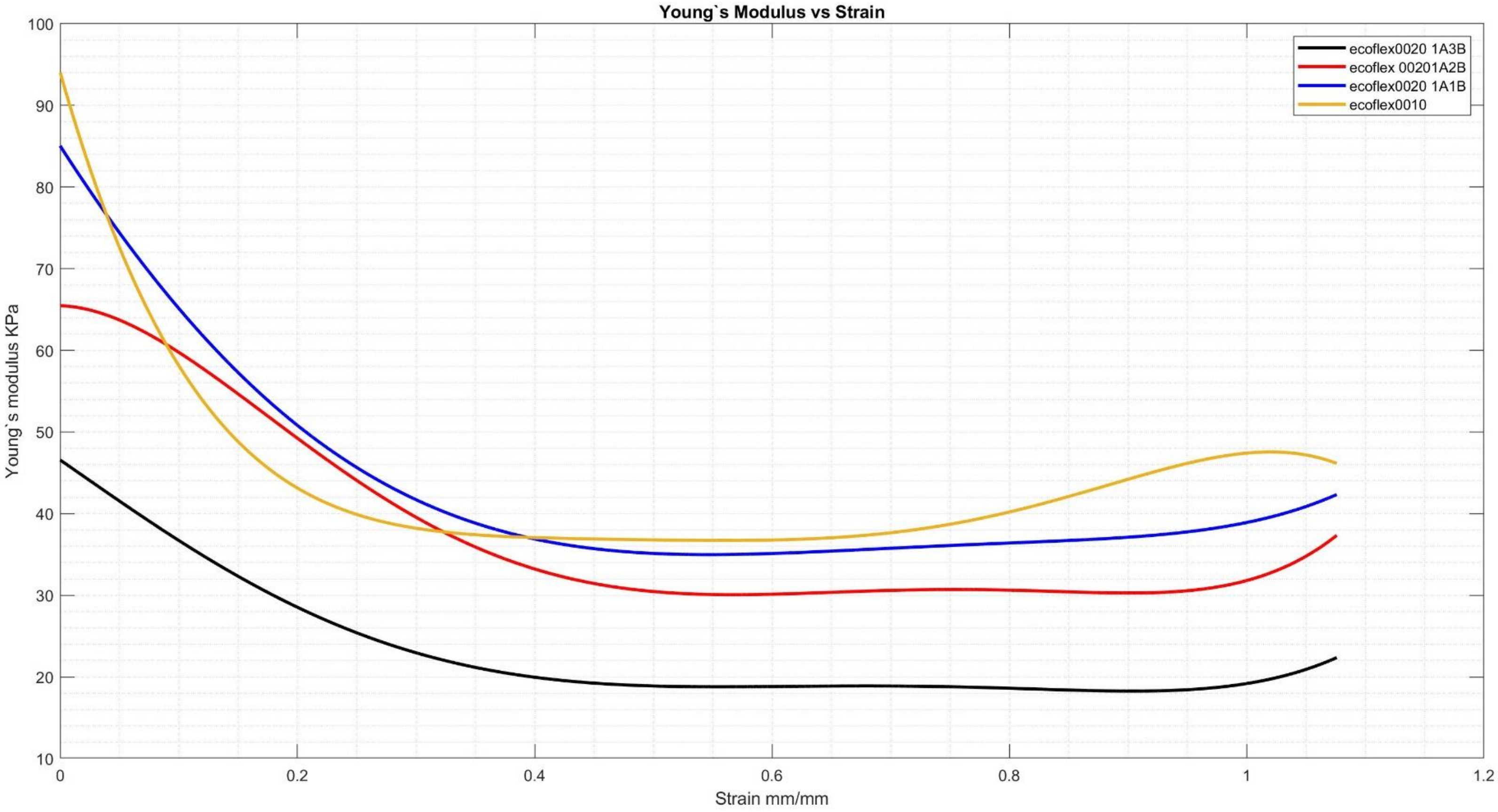

Figure 85 Young's Modulus vs Strain of tensile tests using fourth order polynomial

Figure 83 illustrates that the central difference method did not filter out the noisy data from the tensile tests, making it difficult to quantify the material's Young's modulus over a strain range. However, it works well for the data of compression tests (Figure 84), for which the raw data are less noisy. Consequently, the method of polynomial fitting did work to eliminate the noisy data from the tensile tests. The noisy data were corrected using the polynomial function of order 4 using MATLAB, as illustrated in Figure 85.

5.7.1 Conclusion

The tests were conducted conforming to ISO 7743:2017 (2017) and ISO 37:2017 (2017) standards. It was observed that the mechanical response of Ecoflex materials differs during tensile loading and compression loading. The material was characterised using Young's modulus over the expected working strain range. From the test data, it was observed that materials with lower Young's modulus exhibited larger hysteresis in the loading-unloading curves. This loss of energy can be related to the viscoelastic characteristics of the material. It was observed that the materials with lower Young's modulus were tackier than their counterparts. The mechanical characterisation of various materials adds an advantage of having insights into the material responses and their composition.

From Figure 84 and Figure 85, it can be inferred that all the tested materials exhibit a similar trend during compression and tension but operates at a different elastic modulus. Ecolfex-0010 under compressive loading and tensile loading exhibits Young's modulus in a range of 30 – 50 KPa over the strain that the model is expected to experience during pressure loading. Hence, Ecoflex-0010 was selected for the fabrication of the upper arm phantom. These uniaxial (compression and tension) stress-strain characteristics are used to create a hyperelastic material model for use in the FEA.

Chapter 6 Phantom Fabrication and Test rig

Following the characterisation and selection of material in the previous chapter, this chapter delves into the procedure of developing an upper arm phantom. The aim is to develop an anatomical upper arm phantom and a physical test rig for simulation. The process commences with the design, moulding and casting of the phantom. A test rig is a setup followed by fabrication of the phantom. The design of the test rig is evaluated by boundary conditions of the model, availability of equipment, and desired outcomes of the experimentation. The upper arm phantom test-rig is designed to meet the following objectives: a) Emulate the BP measurement process, b) Investigate the relationship between BP, CP and the corresponding volume changes in the brachial artery and the soft tissue, c) Validation of the anatomical FEA model.

6.1 Geometry of the anatomical model

The models used for FEA in Chapter 4 were simple cylindrical models. Though these models simulate the NIBP measurement procedure, they do not account for the potential deformations on the soft tissue likely to develop from complex geometry. Moreover, the tissue contact conditions are not formulated in the cylindrical models. Therefore, an anatomically accurate model is required to study the mechanical effects on the soft tissue during NIBP measurement.

The geometry of the anatomical model developed is used in the fabrication of the upper arm phantom. This anatomical model is further used to develop a computational model.

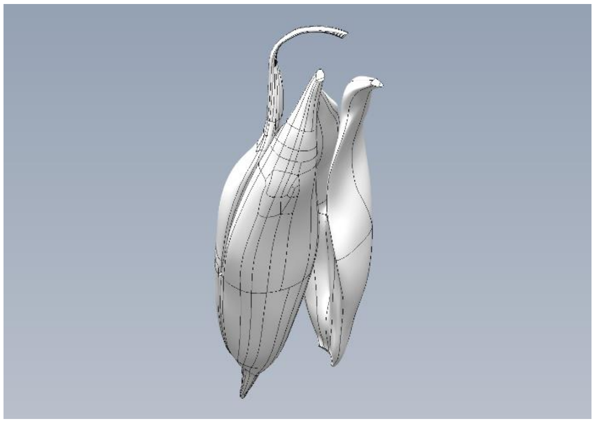

Figure 86 3D CAD model of Biceps brachii and Triceps brachii (Zygote, 2020)

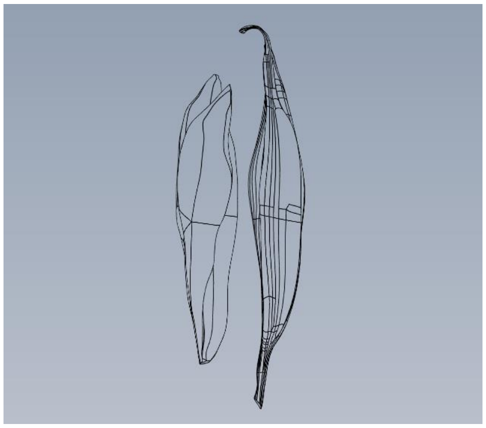

Figure 87 Wireframe of Biceps brachii and Triceps brachii (Zygote, 2020)

The model was developed as a culmination of data from various resources summarised in section 2.1.2 and section 2.2.1. The model is a composed of muscles, SAT layer, the brachial artery and the humerus bone. The geometrical data of the muscles, SAT layer, and the humerus bone was obtained using the dataset from Zygote (2020), which is a CAD model developed from MR images as shown in Figure 86 and Figure 87. The two major muscle groups in the upper arm are the Biceps brachii and Triceps brachii. The CAD model is available publicly as a set of interactive drawings as illustrated in Figure and Figure. The upper arm was sliced midway to obtain the cross-sectional image of the SAT layer, muscle groups, and the humerus bone. The images were delineated using SolidWorks to form a CAD model. Based on the previous study (Bonso et al., 2010), the length of the arm was assumed 223 mm. The location of the brachial artery was determined by the dataset obtained from Zygote (2020). The brachial artery is located in the SAT layer. The diameter of the brachial artery was assumed 4.4 mm Dammers et al. (2015). The anatomical model was developed in the SolidWorks CAD software package.

Figure 88 and Figure 89 illustrates the geometry of the developed anatomical model.

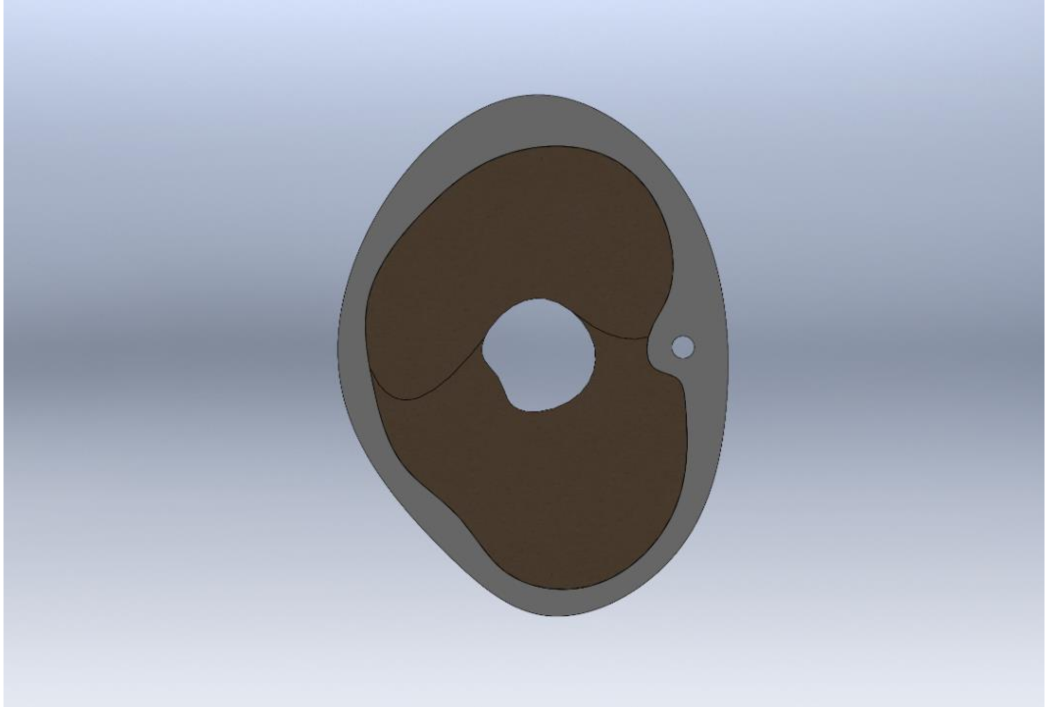

Figure 88 Cross-sectional view of the developed 3D anatomical model. The muscle layer is composed as Biceps brachii and Triceps brachii.

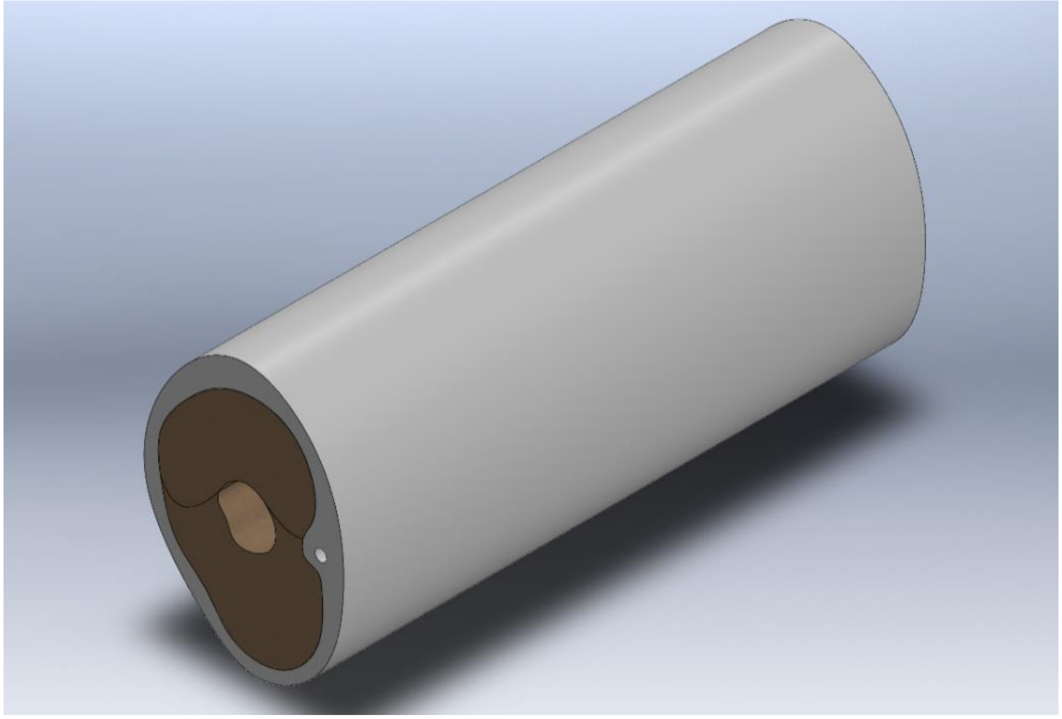

Figure 89 Isometric view of the developed 3D anatomical model. The muscle layer is composed as Biceps brachii and Triceps brachii.

6.1.1 Discussion

a) In the developed anatomical model, the brachial artery is treated as a cylindrical void in the SAT layer. It means that the wall of the brachial artery is excluded from the model. This aids in reducing the complexity of the model since the mechanical properties of the brachial artery wall are different from those of the soft tissues. The elastic modulus of the brachial artery (Messas et al., 2013) is greater than that of the soft tissues (Levinson et al., 1995). Thus, the brachial artery and soft tissues are required to be fabricated from silicone materials of different elastic modulus. In terms of fabrication of the upper arm phantom, the exclusion of the brachial artery wall reduces the potential risk of its separation from the SAT layer due to the ineffectiveness of adhesives. Hence, the brachial artery is assumed to be a cylindrical void in the SAT layer.

b) The muscle component in the developed model is composed of two muscle groups: Biceps brachii and Triceps brachii. Even though this is an accurate anthropometric representation of the muscle groups, it increases the complexity of the model by inducing weak sections in regions where it meets the bone and SAT layer (refer to Figure 88). These vulnerable sections heighten the risk of silicone breakage during the casting of the phantom. In the FEA model, these intricate sections make the meshing process complex. The chose element size of the mesh leads to element distortion errors. A more refined and complex mesh setting is likely to solve this error, but it significantly increases computational time and resources. To avoid these potential risks, the muscle component is modified to be made of a single muscle group. The updated geometry is illustrated in Figure 90 and Figure 91.

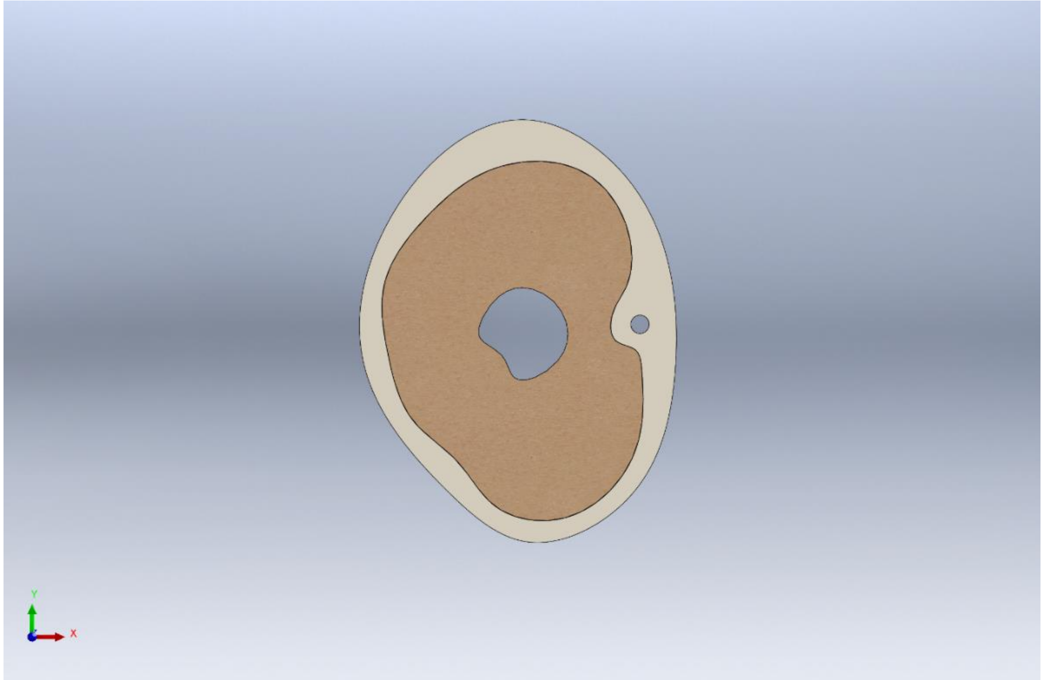

Figure 90 Cross-sectional view of the updated 3D anatomical model. The muscle layer modelled as a single component.

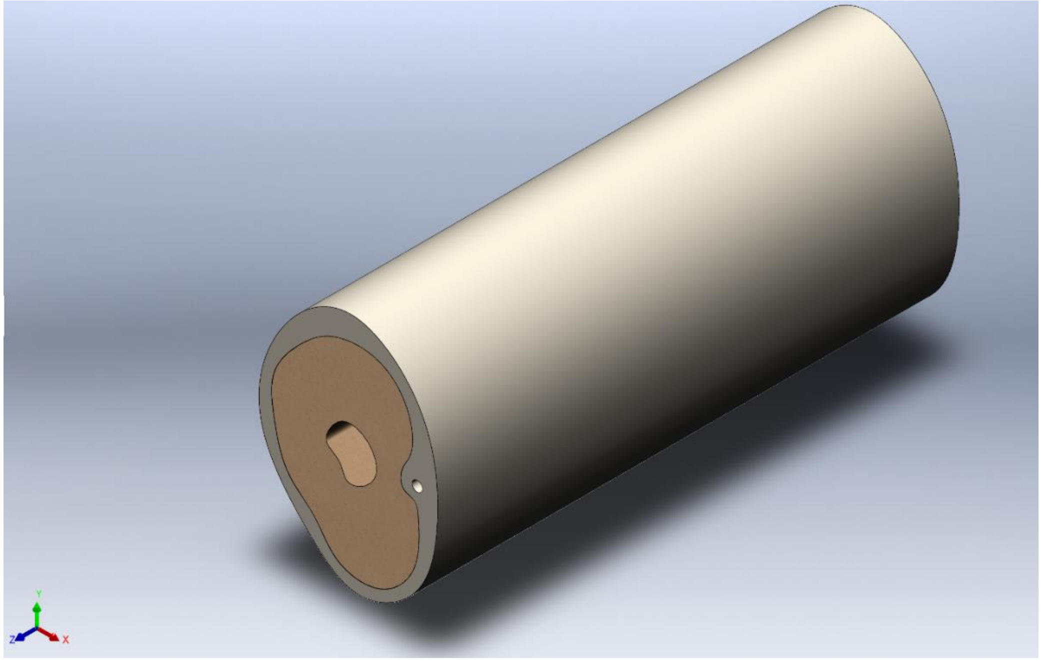

Figure 91 Isometric view of the updated 3D anatomical model. The muscle layer modelled as a single component.

6.2 Upper arm phantom moulding

The anatomical model developed is divided into the SAT layer, muscle layer, and humerus bone. The geometry of the model is such that the layers are perfectly engulfed in one another. Thus, the layers must be cast accurately to their true dimensions. Upper arm phantoms fabricated in the previous studies incorporated a simple cylindrical geometry for which the moulds were developed using rigid and hollow cylinder-shaped material (Anderson-Jackson, 2016), (Lan, 2012), (Subburaj, 2020).

The tissue layers of the model developed in this study exhibit a complex geometry. Hence, the moulds were developed using the 3D printing technique. The material used for the moulds was Polylactic Acid (PLA). It exhibits higher stiffness and higher resistance to heat than ABS. The moulds were designed as assemblies made of various parts to facilitate the ease of removal upon curing the material. The moulding process of each layer is explained in the following sections.

6.2.1 SAT layer moulding

The SAT layer engulfs the muscle and forms the outermost part of the anatomical model. The brachial artery is placed as a cylindrical void in this layer. Since the SAT layer is considerably thin, and Ecoflex-0010 material is soft and tacky, improper removal creates a potential risk of surface damage or other anomalies. To ensure the safe removal of the cured layer, the mould comprises various carefully designed parts to be assembled. The design of the mould was created using SolidWorks. Figure 92 demonstrates the exploded view of the first iteration of the mould. The mould assembly comprises four parts: a base part, a middle part, and two side mates. This first iteration aided in establishing the mechanism for the mould assembly. It was inferred that the mould is bulky in terms of its size. The bulkiness leads to unnecessary material consumption and an increase in the time required to 3D print the parts.

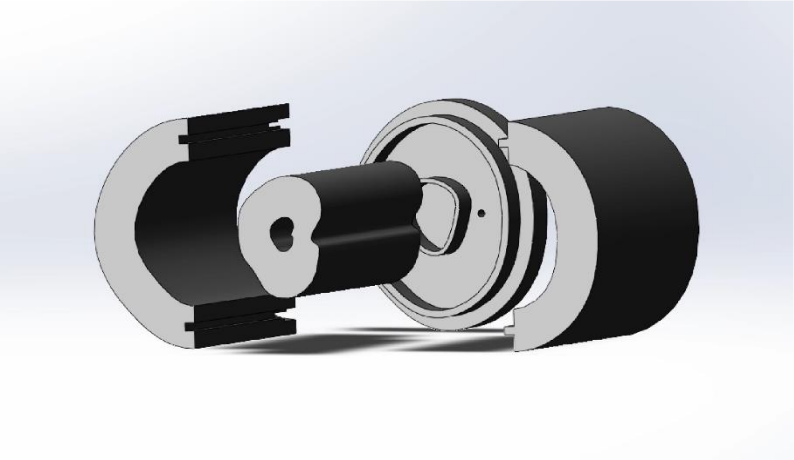

Figure 92 Primary mould design to cast SAT layer.

The refined mould is illustrated in Figure 93. The mould parts are comprised of male and female slots. A tolerance of 0.3 mm was set to the mating slots to ensure ease of removal. On the base mould part, a circular void measuring 4.4 mm in diameter was created. A circular aluminium rod was put in the mould assembly to obtain a cylindrical void for the brachial artery. Ecoflex-0010 was cast around the aluminium rod to create a cylindrical void that represents the brachial artery.

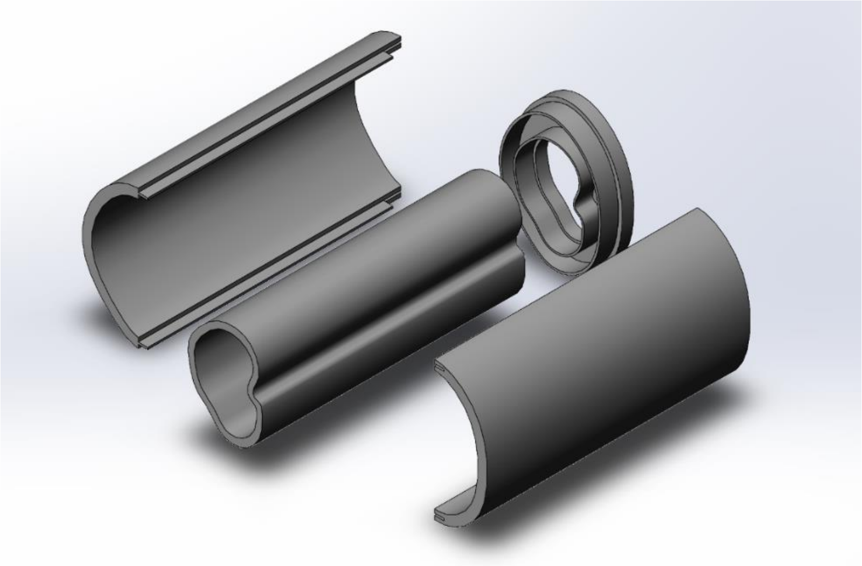

Figure 93 Finalised mould design to cast SAT layer.

6.2.1.1 Mould assembly test

Upon finalising the mould design for the SAT layer, the assembly was tested using a scaled-down model (1:2) for potential discrepancies. The time required to print this model was short, and it allowed for detailed insights of improvement. The printed model is shown in Figure 94.

It was observed that the bottom-most layer of the 3D printed model tends to soften due to the heat of the 3D printer's bed. The bottom-most layer of the parts also included the mating slots. Due to softening, the set tolerance limits were distorted, because of which the parts could not be mated with ease. A solution to eliminate this discrepancy was to print the parts upside down. It meant that the surface that consists of the slot now forms the topmost layer during 3D printing.

Figure 94 1:2 3D printed mould assembly for testing.

6.2.2 SAT layer casting

The discrepancies associated with printing the mould parts were identified from the 1:2 scaled-down model. The procedure was modified to eliminate unwanted errors. The final mould was printed using PLA. Cumulatively, 1012 grams of PLA was required to print the mould assembly. The total time is taken to 3D print the assembly was 49 hours. Figure 95 illustrates a schematic of the placement of mould parts on a 3D printer bed.

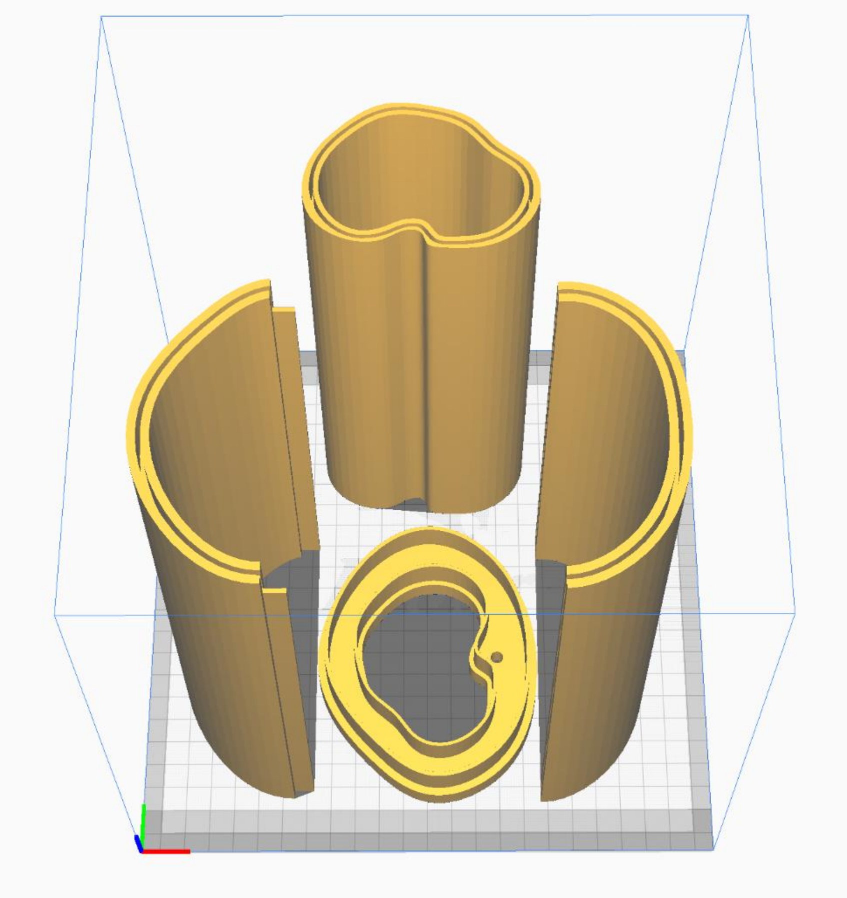

Figure 95 Schematic of placement of mould parts on the 3D printer bed

The printed mould parts were assembled. An aluminium rod of the diameter of the brachial artery was fixed in its created void on the base part.

The mould was poured in two batches. According to the supplier’s specifications, the curing time of time Ecoflex-0010 is 4 hours. The working time of Ecoflex-0010 is 20 minutes. The 1:1 mixture of Part A and Part B was vacuumed for 7 minutes (refer to Figure

96) to eliminate air entrapments. The pouring of mould in two batches allowed for effective vacuuming before the end of working time.

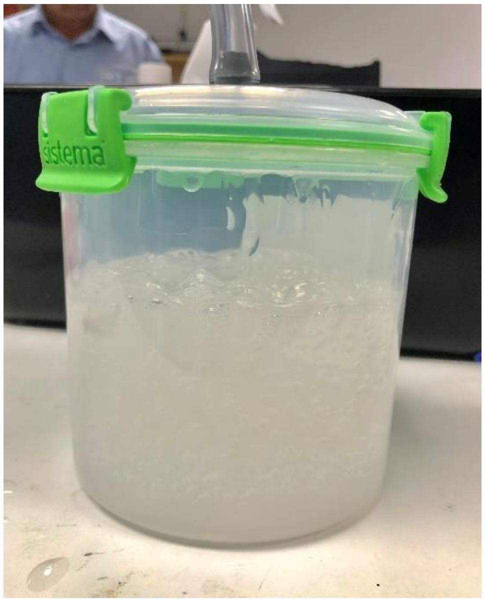

Figure 96 Vacuuming of Ecoflex-0010

Upon pouring, the mould was allowed to cure for 24 hours. Upon curing, the mould was removed part-by-part carefully.

Figure 97 and Figure 98 shows the cast SAT layer. The cast layer exhibited no air entrapments, surface irregularities, and non-homogenously cured portions.

Figure 97 Cross sectional view of the cast SAT layer

Figure 98 Lateral view of the cast SAT layer

6.2.3 Humerus bone fabrication

The muscle layer engulfs the humerus, and it supports the entire upper arm phantom. The elastic modulus of the humerus bone ranges from 14099 – 22445 MPa (Rahmoun et al., 2020). From the elastic modulus, it can be inferred that the humerus bone is rigid. The humerus bone in the developed anatomical geometry is a complex-shaped structure.

Since it is a rigid component, it was 3D printed using PLA filament. Young's modulus of the PLA filament was reported to be 2004 MPa (Kamthai & Magaraphan, 2015), significantly higher than Ecoflex-0010. The density of the filament during printing was set to 40 %. This meant that the additive layers were closely spaced to each other. Increasing the density of the print increases the stiffness of the 3D printed component. The length of the bone was kept at 250 mm. The length was increased by 30 mm to further provide room for developing boundary conditions for testing the arm phantom. Figure 99 illustrates the schematic model of the humerus on the 3D printer bed.

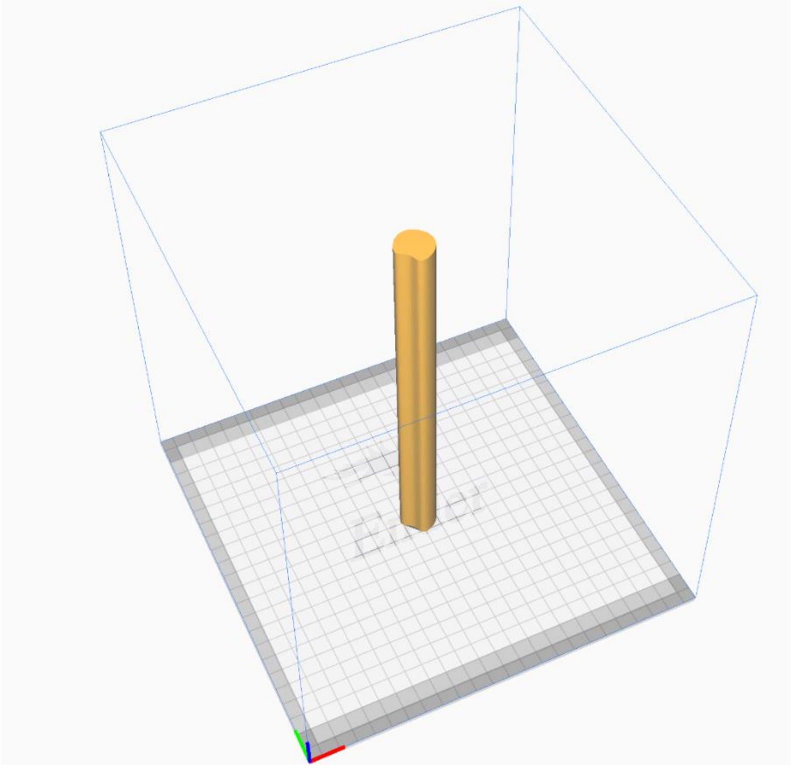

Figure 99 Illustration of the humerus bone on 3D printer bed

6.2.4 Muscle layer moulding

The muscle mould assembly is comprised of three parts. The 3D printed humerus bone was placed in the middle of the mould assembly, as illustrated in Figure 100. The muscle layer was cast around the bone. Ecoflex-0010 was vacuumed and poured in two batches. It allowed for effective vacuuming of the material before it started to cure.

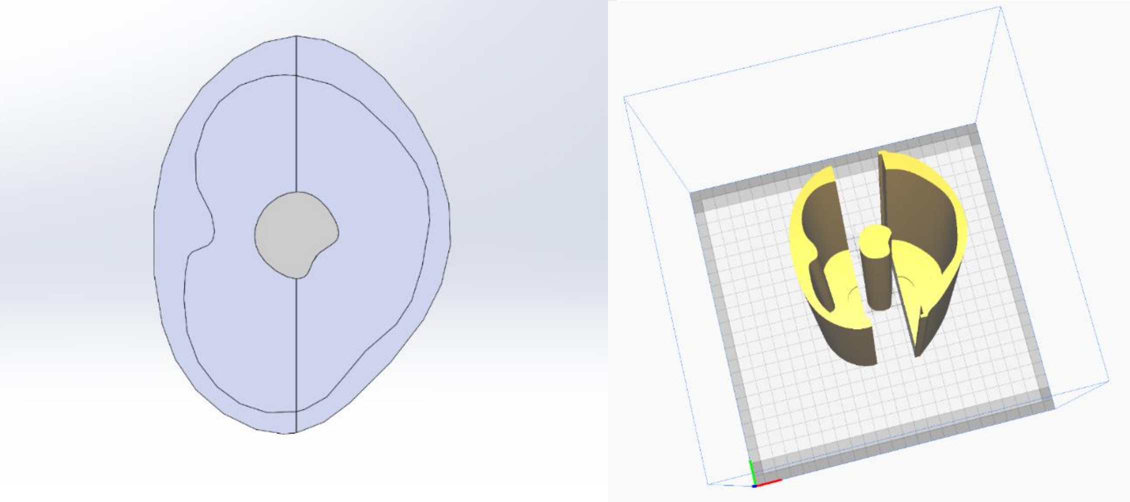

Figure 100 A top view of the designed mould components to cast the muscle layer.

The poured material was allowed to cure for 24 hours before it was removed from the mould. An isometric and a lateral view of the cast muscle layer is illustrated in Figure 101.

Figure 101 Isometric (left) and a lateral (right) view of the cast muscle layer

The cast muscle layer did not exhibit air entrapments, surface irregularities, and uncured portions. It was put on top of the muscle layer using silicone grease. The assembled upper arm phantom is illustrated in Figure 102.

Figure 102 The assembled anatomical upper arm phantom

6.2.5 Discussion

The upper arm phantom was fabricated using additive manufacturing and lost core moulding techniques. For the anatomical geometry, these techniques proved effective, and the desired outcomes were obtained. It was inferred that due to the tackiness of Ecoflex-0010, the mould was challenging to remove after curing. However, the phantom was not damaged during the removal. A possible solution to tackle this issue is the use of a mould-release agent. The tackiness of Ecoflex-0010 results in increased friction when the SAT layer was assembled on the muscle layer. This increased friction led to the stretching of SAT layer. To overcome this, a silicone gel was applied on the top of the muscle layer, which aided in reducing the friction between the two layers. As a result, the SAT layer was assembled on the muscle layer without being stretched. The silicone gel used dries up after some time upon application. Upon drying the silicone gel, the tackiness of Ecoflex-0010 develops a bonded contact status between the SAT and muscle layers.

Since the upper arm phantom testing requires the brachial artery to be internally pressurised, a small external tube cast from Ecoflex-0020 was glued at one end of the brachial artery. This tube has the same internal diameter as that of the brachial artery but has a greater thickness—the tube aids in transmitting pressure to the brachial artery without hindering its length. The tube was made thicker and cast from a material of higher elastic modulus to prevent pressure losses during transmission. A Y-connector was used to connect the brachial artery to a sphygmomanometer and a hand pump, as seen in Figure 103.

Figure 103 Attachment of sphygmomanometer and a hand pump with the brachial artery

6.3 Test-rig setup

The fabricated upper arm phantom was tested underwater bath for breakages and irregularities, as shown in Figure 104. The brachial artery was pressurised to $100\ mmHg$ using a hand pump and a sphygmomanometer. The test demonstrated no pressure loss at the connections during the transmission of air pressure (refer to Figure 105). During this testing, the brachial artery was manually occluded from one end to prevent loss of pressure.

Figure 104 Brachial artery pressure test for leakages

Figure 105 Stable reading on sphygmomanometer suggesting pressure loss.

The upper arm phantom testing aims to measure the volume changes of the brachial artery and the soft tissue for the subjected internal and external pressure loads. During testing, the pressure subjected to the brachial artery emulates blood pressure. The pressure subjected to the outer surface of the phantom emulates the cuff pressure during BP measurement. The boundary conditions established in chapter 4 are required to be imposed on the upper arm phantom. The aim is to constrain the ends of the phantom in a manner that does not allow it to deform axially during loading. The experimentation aims at determining the volume changes against the known pressure loads for two cases. It is assumed that contact between the SAT layer and muscle layer is bonded in the first case. In the second case, the contact between the SAT and muscle layers is assumed to be frictionless, abiding by the theory mentioned in Section 2.2.3.1.

6.3.1 Test-rig design

The upper arm phantom is subjected to arterial pressure and cuff pressure. Initially, the cuff pressure was applied using a clear cuff filled with water. The clear cuff makes it feasible for an ultrasound probe to be used on the phantom. The proposition was to calculate the volume change in the artery derived from the displacement due to applied pressure. A pressure-volume catheter was used to monitor the pressure inside the clear cuff, as shown in Figure 106.

Figure 106 Preliminary test rig setup check using a clear cuff and a catheter

The cuff pressure boundary condition on the external surface of the arm is such that it covers the entire surface of the upper arm. A custom-sized clear cuff required to fulfil this criterion could not be procured. Using this system, the volume change in the soft tissue was difficult to quantify. Therefore, the use of a clear cuff to impose the pressure boundary condition was ruled out.

To overcome the limitations of this setup, a new test rig was designed. An acrylic cylinder of diameter $40\ mm$ was cut using a hack saw (see Figure 107) to match the length of the arm.

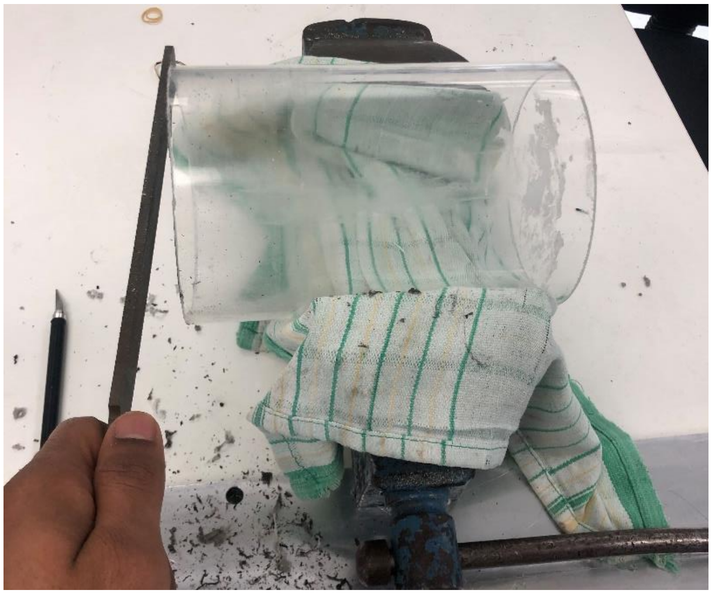

Figure 107 Fabrication of an acrylic cylinder to develop a test rig for the upper arm phantom

The lids for this acrylic cylinder were 3D printed using PLA filament. The lids were designed to make the cylinder airtight, as shown in Figure 109. Rubber gaskets were used

Figure 108 Openable 3D printed lid on the test rig

Figure 109 The upper arm phantom enclosed inside the test rig

to make the chamber airtight. The lids incorporated grooves of the shape of the humerus bone. The grooves aided in locating and placing the phantom inside the cylindrical chamber. The lid on one end of the cylinder was kept openable (refer to Figure 108). This flexibility allowed to fix any potential discrepancies. It also allowed changing the contact condition between the SAT and muscle layer. A hose was provided at the end of both lids. The hose on one end allowed pressurising the artery. It emulates the blood pressure during a cardiac cycle. The hose on the other end of the lid was allowed to pressurise the outer surface of the soft tissue emulating the cuff pressure during NIBP measurement. Water was used to emulate the pressure loads on the upper arm phantom system, as shown in Figure 110. This setup has the added advantage of exhibiting the CP and BP uniformly across the length of the arm as opposed to a clear cuff.

Figure 110 Test rig filled with water to emulate CP on the outer surface of the arm phantom

The experiments from the test rig aimed to obtain the volumetric changes in the brachial artery and the soft tissue. To measure the volumetric changes due to pressure loads, pipettes were incorporated on both ends of the lids, as shown in Figure 112 and Figure 111.

Figure 111 Pipette connected at the end of the brachial artery to measure volume change

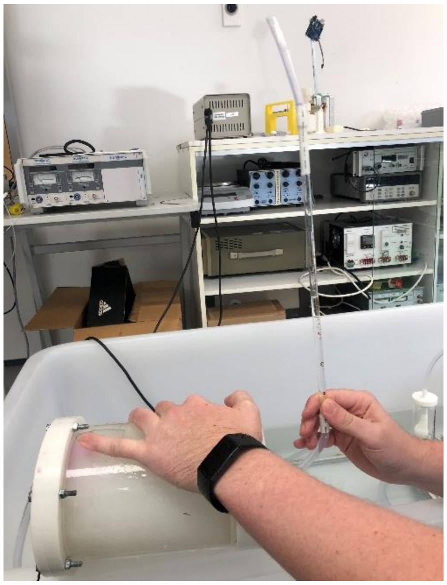

Figure 112 Pipette connected at the outer surface of the phantom to measure volume change

The pipettes were further connected to hand pumps to apply pressure loads. The emulated pressures were monitored using a sphygmomanometer.

During the initial testing, it was observed that changing the cuff pressure directly changed the arterial pressure and vice versa. To achieve independent control over these pressures, it was essential to de-couple them. Air reservoirs were added between the hand pump and the pipette on both ends.

The test rig setup is illustrated in Figure 113. In Figure 113, it should be noted that a little water spilled near the test rig does not represent leakages in the setup. The picture was clicked immediately when the test rig was taken out of the water bath for documentation purposes.

Figure 113 Test rig setup to obtain the pressure-volume change relationship in the upper arm phantom during NIBP measurement.

6.3.1.2 Discussion

The aim of constructing the test rig was to obtain the pressure-volume change relationship of the upper arm during the NIBP measurement. The use of ultrasound imaging was predicted to determine the pressure-displacement relationship in the brachial artery and thus the pressure-volume relationship. Ultrasound imaging requires a clear cuff to obtain images of the phantom under loading. However, a water-filled clear cuff that covers the entire length of the arm to emulate the CP could not be procured.

The construction of an airtight cylindrical chamber with custom 3D-printed lids allowed to impose the desired boundary conditions. The provision of hoses on both ends of the lids allowed to emulate cuff pressure on soft tissue and blood pressure on the brachial artery independently. These pressures were created using water as a medium. Pipettes were used to measure the volumetric changes on the upper arm phantom system for given pressure loads. The use of pipettes allowed for a precise measurement of volumes. It was observed that the test-rig setup coupled the cuff pressure and the arterial pressure. Changing one pressure would change the other. The addition of air reservoirs in the test rig eliminated this effect. An independent control was achieved on each of the emulated pressures.

The removable lid on the cylindrical chamber allowed to change the contact condition between the SAT layer and muscle layer. However, the test rig could not produce viable and reproducible results for the sliding contact condition upon reopening the lid. The discrepancy can be attributed to the minor pressure losses created between the lid and the acrylic cylinder. The accuracy of the imposed boundary conditions was difficult to determine due to the presence of end-effects created due to the cylindrical chamber. As a result, the test rig could not be filled up with water entirely. The air bubble present in the chamber increased in size upon application of CP and BP.

Consequently, the water volume in the pipettes remained unstable. However, the test-rig setup satisfied the aims of the experiment considering the project's limited timeline. The results obtained from the experiment are presented in the following section.

6.4 Results

The test was conducted for a range of CP and BP, keeping the TP constant. The contact condition between the soft tissue layers of the phantom was kept bonded. The resultant volume change in the soft tissue and the brachial artery for a given set of pressures is shown in Table 7. The trend of the volume change over the given pressure range is illustrated in Figure 114.

Blood pressure (BP) mmHg	Cuff pressure (CP) mmHg	Transmural pressure (TP) mmHg	Volume change mL	
			Brachial artery	Soft tissue
10	40	30	0.10	0.3
20	50	30	0.20	1.2
30	60	30	0.35	2.2
40	70	30	0.45	3.2
50	89	30	0.55	4.2

Table 7 Volume change in soft tissue and the brachial artery

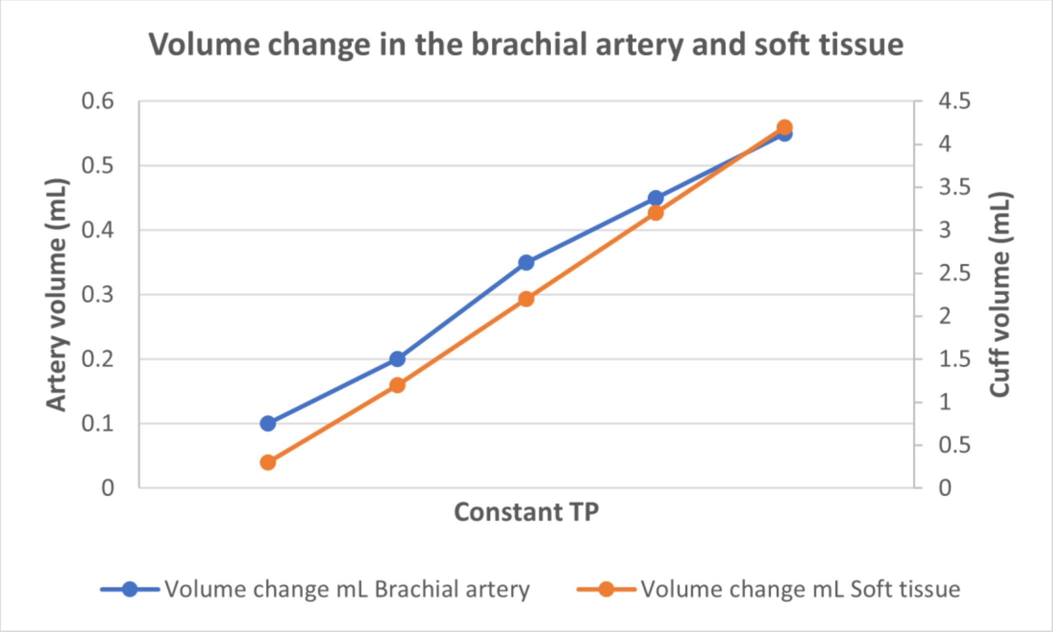

Figure 114 Volume change vs Constant TP

The brachial artery undergoes expansion as BP and CP are increased whereas, the soft tissues undergo compression. It can be inferred from Figure 114 that the compression of the soft tissue is linear in magnitude. The linearity in volume change can be attributed to the constant TP. In contrast, the expansion of the brachial artery is not linear in magnitude.

As mentioned in Section 6.3.1.2, the phantom could not be tested for a varied set of pressure ranges due to pressure losses and inconsistent readings from air entrapments in the test rig. The results of this experiment are validated with the anatomical FE model (refer to Section 7.4).

Chapter 7 Anatomical model Results and Discussion

This chapter explains the process of solving the developed anatomical geometry using the FEM in ANSYS. The development of anatomically accurate geometry is explained in Section 6.1. In this analysis, the muscle and the SAT layer are assumed to be the same material, termed soft tissue. The brachial artery is treated as a cylindrical void with no wall thickness. The model is simulated for the given CP and BP with bonded and frictionless contact conditions between the muscle and SAT layers. The model setup is explained in the following sections.

7.1 Material model

As mentioned in Section 5.7.1, Ecoflex-0010 was concluded to emulate the soft tissues (muscle and SAT). The stress-strain relationship of Ecoflex-0010 under uniaxial tensile and compression loading was used to develop a hyperelastic constitutive material model in ANSYS. A hyperelastic material is a constitutive model for which the stress-strain relationship is derived from a strain energy density function of a material (Gründemann, 1985).

A Mooney-Rivlin constitutive model was used to characterise the mechanical properties of Ecoflex-0010. It is a unique form of the Polynomial model. Based on the order of level, there are four types of Mooney-Rivlin models: 2-parameter, 3-parameter, 5-parameter, and 9-parameter strain energy models (Mooney, 1940). The higher-order models characterise the complex stress-strain constitutive relations with an expense of computational efforts, extensive experimental data, and parameter fitting. In this study, the stress-strain relationship of the material in compression and tension generates a single inflexion point under uniaxial loading. Here the point of inflexion occurs at a point where the stress-strain curve transitions from compression to tension, as seen in Figure 115.

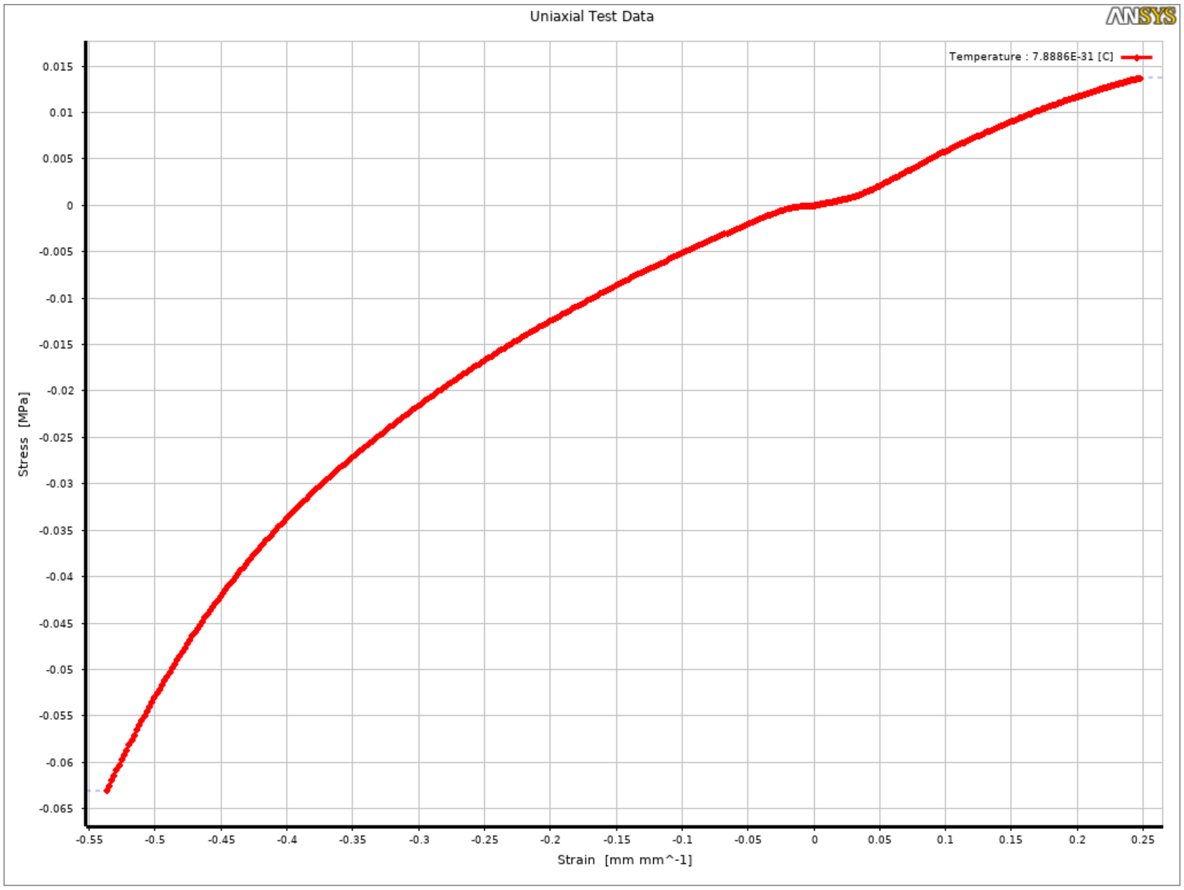

Figure 115 Stress vs Strain curve of Ecoflex-0010 under uniaxial loading (compression and tension).

A 3-parameter Mooney-Rivlin constitutive model was found suitable to characterise the uniaxial stress-strain relationship of the given material. The strain energy density function of the 3-parameter Mooney-Rivlin constitutive model is given by:

$$\boldsymbol{W = C_{10}\,(I_1 - 3) + C_{01}\,(I_2 - 3) + C_{11}\,(I_1 - 3)\,(I_2 - 3) + \frac{1}{D_1}\,(J - 1)^2}$$ (Mooney, 1940)

Here, $\boldsymbol{W}$ = Strain energy density, $\boldsymbol{I_1, I_2}$ = Strain invariants, $\boldsymbol{C_{10}, C_{01}, C_{11}}$ = Material constants

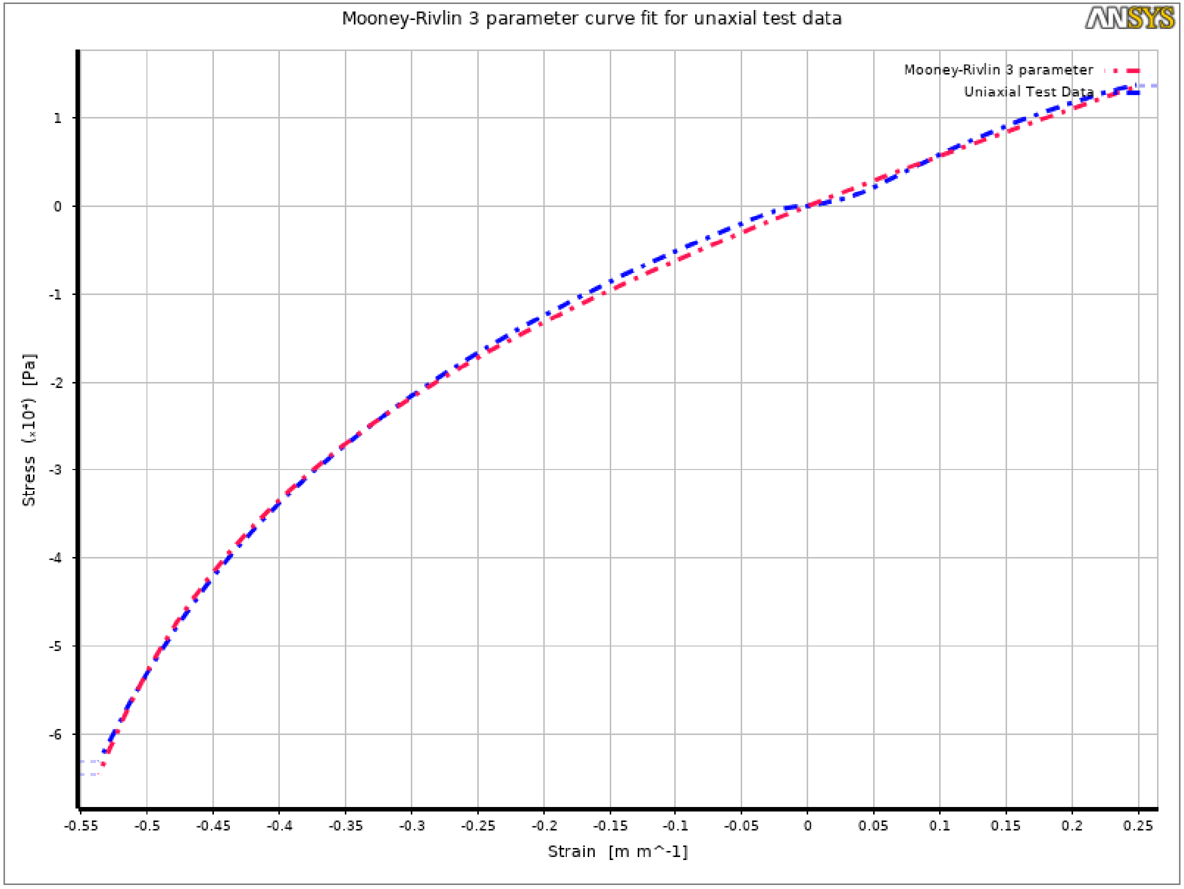

Figure 116 Curve fit for uniaxial test data with a Mooney-Rivlin 3 parameter constitutive model

Figure 116 shows the Mooney-Rivlin 3 parameter curve fit for the uniaxial test data. The Mooney-Rivlin 3 parameter constitutive model formulated using the uniaxial experimental data was used to verify the tensile and compression tests using ANSYS.

7.1.1 Compression test verification

As mentioned in Section 5.4, the compression test conducted experimentally was simulated in ANSYS (refer to Figure 117) to verify the material model. The Engineering stress-strain relationship was obtained from the simulation. Figure 118 illustrates the numerical verification of the stress-strain relationship of the material.

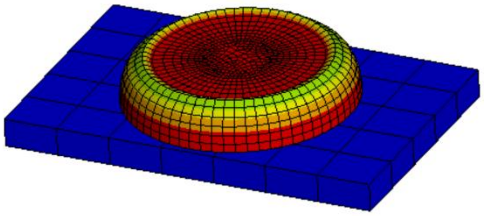

Figure 117 Deformed test specimen in the compression test simulation

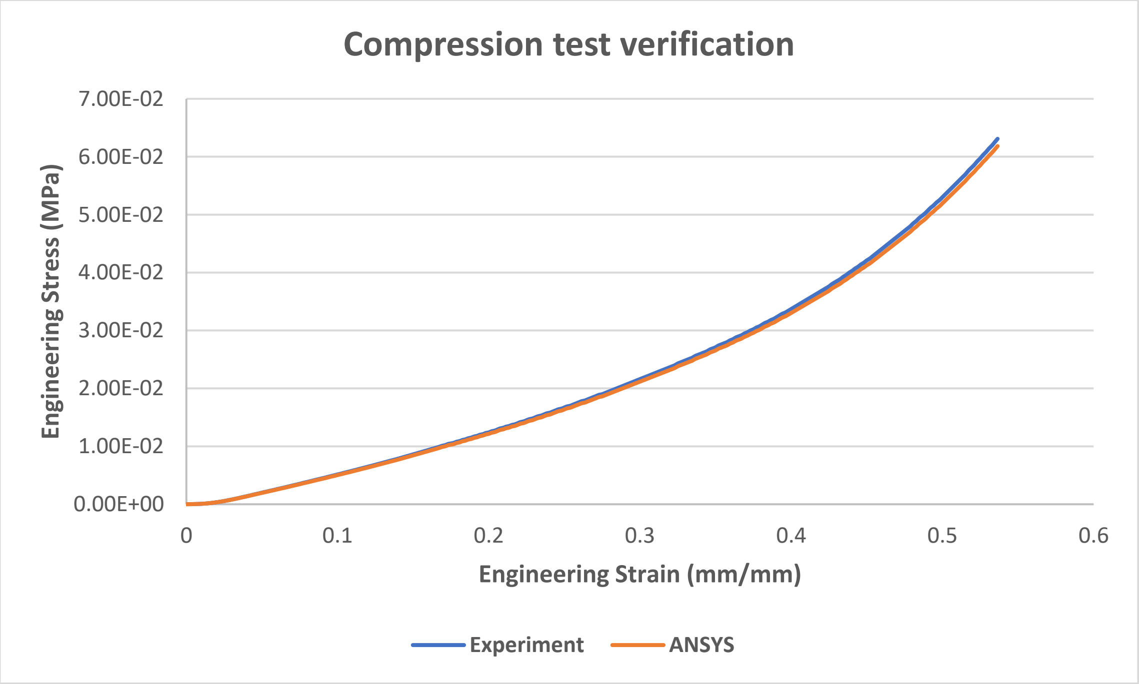

Figure 118 Compression test verification using the formulated constitutive material model

The results obtained from the simulation were within 2% accuracy of those obtained from the experiments.

7.1.2 Tensile test verification

Similarly, the tensile test conducted as mentioned in Section 5.2 was simulated in ANSYS to verify the material model. A simple model consisting of a base plate and a rectangular

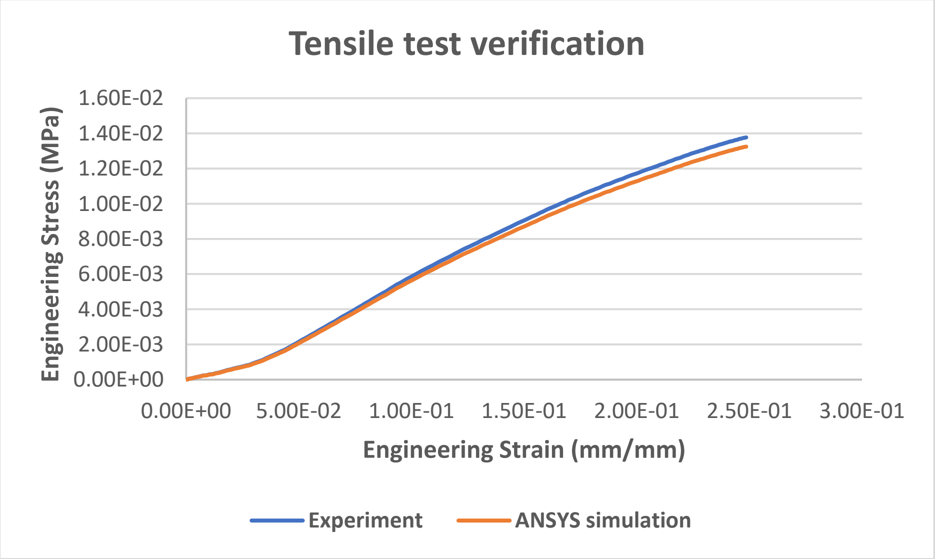

Figure 119 Tensile test verification using the formulated constitutive model

specimen of the same size as the experimental specimen was set up for the given displacement. Figure 119 illustrates the stress-strain curve comparison of the experimental and simulation results. The results obtained from the simulation were within 3.8 % accuracy of those obtained from the experiments.

7.1.3 Simple shear test

The 3-parameter Mooney-Rivlin model was formulated using the uniaxial tests. The material constants C_{10}, C_{01}, C_{11} and thus, the strain energy density function is derived from the provided test data. The stress-strain relationship data of the material under biaxial tension and planar tension (pure shear) was not characterised as per the project's timeline. However, the material constants change when the stress-strain relationship of the entire test data (uniaxial, biaxial, planar tension) is provided. For the model where the contact condition between the SAT and muscle layer is assumed frictionless, the soft tissue is expected to experience deformation due to shear forces. To verify the behaviour of the material model under shear loading, a simple shear test was conducted on Ecoflex-0010.

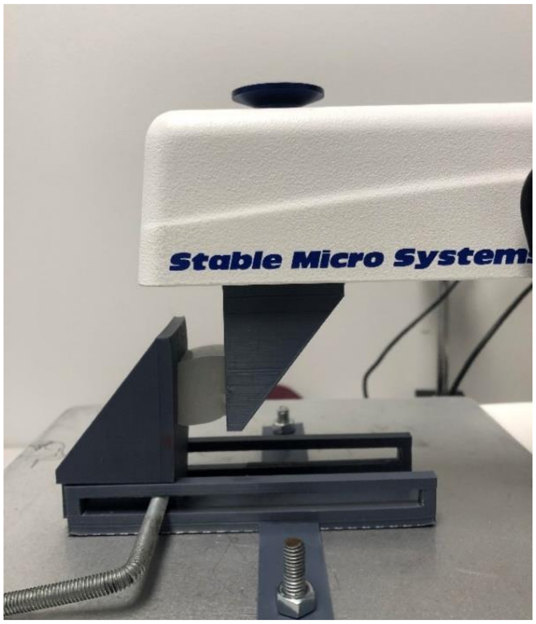

Figure 120 Simple shear test rig set up on Texture Analyser

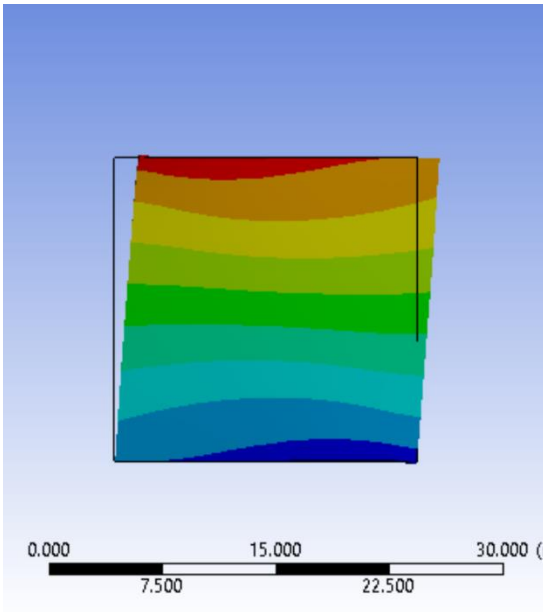

Figure 121 Deformation of the test specimen as a result of the simple shear test simulation in ANSYS

The apparatus illustrated in Figure 120 was 3D printed with PLA such that it can be adjusted to hold the test specimen without compressing it. The specimen was displaced for 3 mm using the 'Texture Analyser TA + XT'. The force-displacement relationship was converted into the stress-strain relationship. The experiment results were verified by setting up the test with the applied boundary conditions in ANSYS (see Figure 121). The comparison of the results is illustrated in Figure 122.

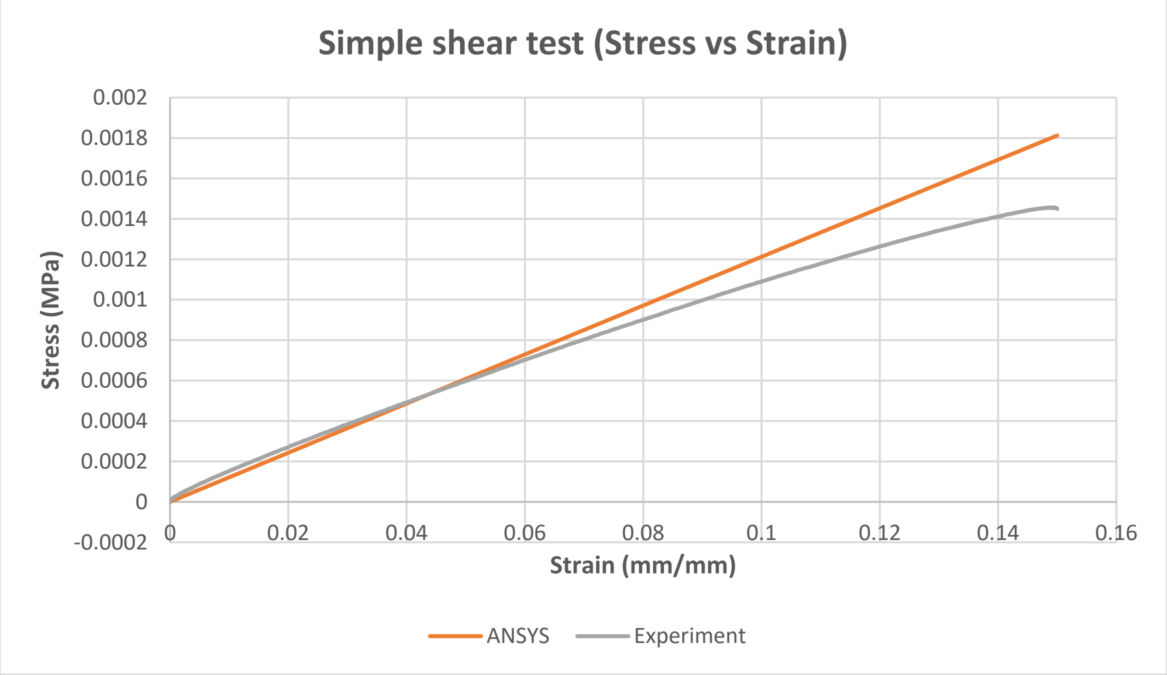

Figure 122 Numerical verification of the simple shear test

It can be inferred from Figure 122 that the experiment results and the simulation results do not match. The boundary conditions in the simulation were changed. The 'displacement' component in boundary conditions was replaced with the 'remote displacement' component. It allows the surface on which the boundary condition is applied to deform. Similarly, the 'fixed support' component was replaced with the 'remote displacement' component. The bottom surface of the specimen on which it was applied was allowed to deform, keeping the coordinates of the surface constant. Upon replacing the components in the boundary condition, the simulation results and the experimental results converged within an accuracy of 5 %. The results are illustrated in Figure 123.

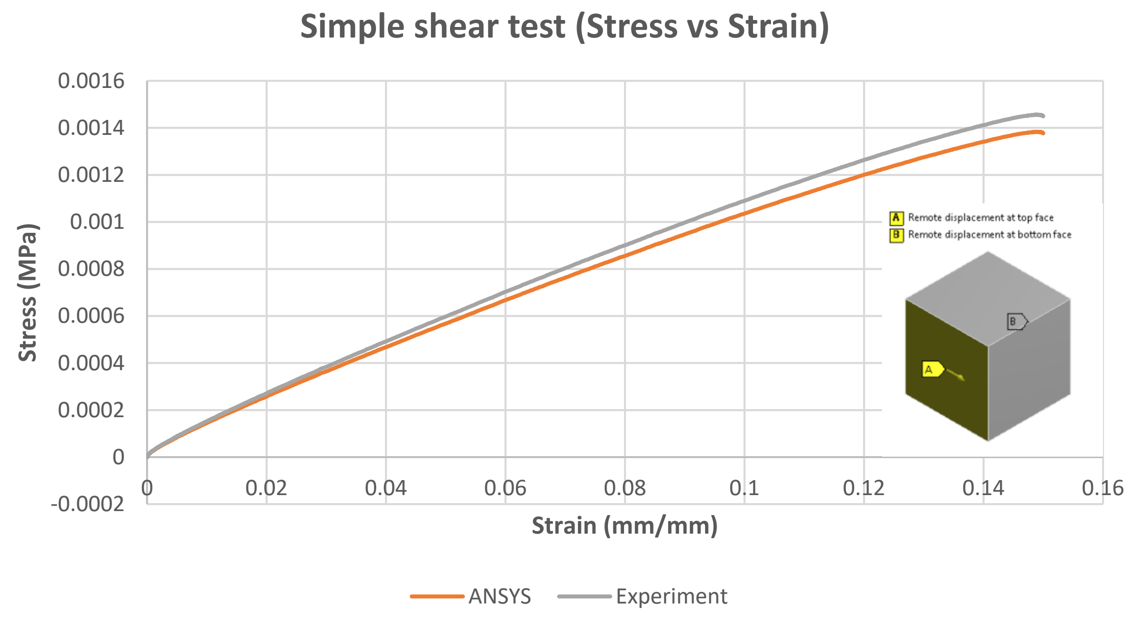

Figure 123 Numerical verification of the simple shear with changed boundary conditions

was conducted. The stress-strain relationship of Ecoflex-0010 obtained from the simple shear test was verified with the simulation of the test in ANSYS. The boundary conditions in the simulation were set up assuming that the test specimen is under simple shear loading, meaning the absence of compressive or tensile forces during the testing. However, the simulation results and the results obtained from the experiment did not converge. To analyse this non-convergence, the boundary conditions in the simulation were changed. The ‘fixed support’ component in the boundary condition was replaced with ‘remote displacement’. Using this component, the surface was allowed to deform while still keeping its coordinates constant.

Similarly, the ‘displacement’ component was replaced with ‘remote displacement’ as well. With these components in boundary conditions, the results from the simulation converged within an accuracy of 5 % to those of experimental results. From these results, it can be inferred that the assumption of the absence of other forces in the simple shear test is invalid. In the experimental setup, the top and bottom faces of the test specimen were not glued to the test rig. It is likely that these faces were deformed as the specimen was displaced during the test. Thus, it is likely that the imposed boundary conditions in the experiment did not produce a simple shear test, However, the established 3-parameter Mooney-Rivlin hyperelastic model was used to simulate the soft tissues in the model with anatomical geometry.

7.2 Boundary conditions

The following boundary conditions are applied to the anatomical model (see Figure 124):

1) The humerus bone acts as a rigid component in the upper arm assembly because of its higher elastic modulus. Thus, during BP measurement, the deformation exhibited by the bone is negligible. The muscles are bonded to the humerus bone making their contact surface the same. A ‘fixed support’ boundary condition is applied on the internal surface of the muscle layer. With this boundary applied, the bone is excluded from the simulation. The exclusion of the bone lowers the computational time of the simulation.

2) It is assumed that there is no relative motion between the cuff and the outer surface of the soft tissue during the BP measurement. Thus, the CP is exerted radially across the surface of the upper arm.

3) During the BP measurement, the position of the arm is fixed in space. The upper arm terminates at the shoulder and elbow at the proximal and distal end, respectively. Thus, the soft tissue is allowed to deform in the radial and circumferential plane ($r - \theta$) only. A ‘frictionless support’ boundary condition is applied on both ends of the upper arm model.

7.2.1 Interactive conditions

The interactive tissue conditions assumed in this model are:

1) The brachial artery is assumed bonded to the surrounding soft tissue layer, meaning there is no relative movement between the two.

2) Two cases are assumed while setting up the contact status between the SAT and muscle layers. As per the theory mentioned in section 2.2.3.1, the contact status between the muscle layer and the SAT layer is assumed frictionless as shown in Figure 124

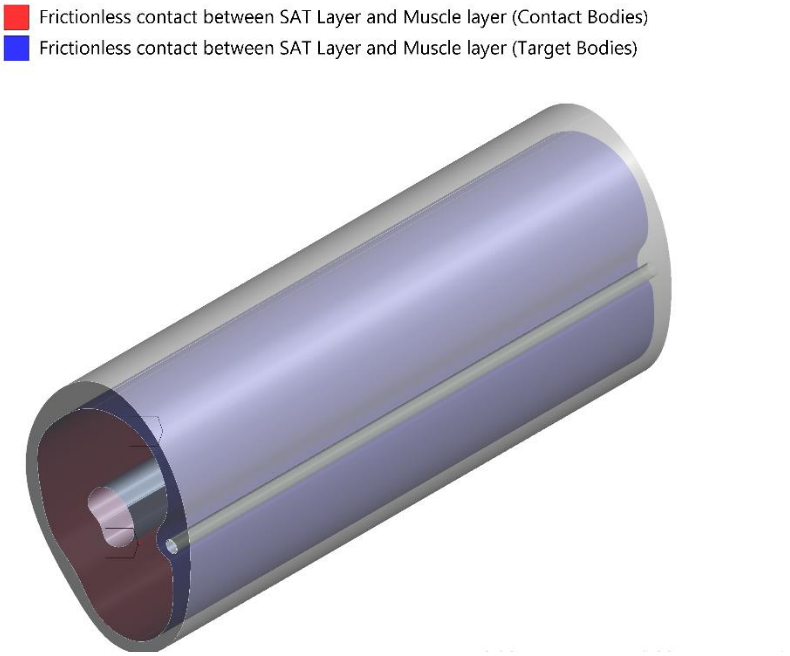

Figure 124 Frictionless contact between SAT and Muscle layers. Humerus bone and brachial artery is bonded. Frictionless support at ends. Fixed support at the bone.

A model where the contact status between these layers is assumed bonded, as shown in Figure 125 is also solved.

3) The contact status between the humerus bone and the muscle layer is assumed bonded in both the cases.

4) The complex anatomical geometry results in minor penetrations and gaps among the sharing surfaces. To amend this problem, a trim tolerance of 0.64 mm was set between the contacting layer surfaces. This setting eliminates additional elements created outside of the trim tolerance to improve solution accuracy and reduce the computational expense.

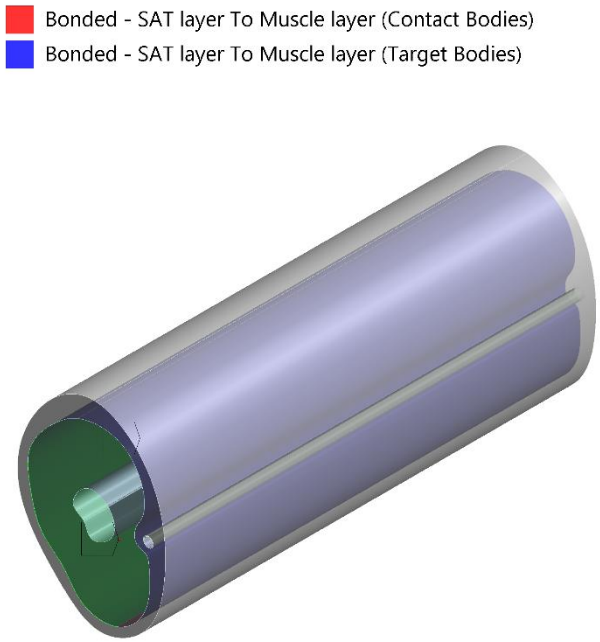

Figure 125 Bonded contact between SAT and Muscle layers. Humerus bone and brachial artery is bonded. Frictionless support at ends

7.3 Model mesh and convergence

A hex (HEX20 SOLID186) element in ANSYS was used to mesh the brachial artery and the soft tissues. In order to scope the results with ease, the thickness of the brachial artery was assumed to be 0.4 mm (Dammers et al., 2015). A mesh convergence study was conducted on the given anatomical model to achieve a balance between accuracy and computational expense. The results from the solution were analysed for increasing number of meshed elements in the model. The model was simulated for a slip interactive condition between the SAT and muscle layers with cuff pressure $P_O = 80\ mmHg$ and $P_I = 50\ mmHg$. The maximum displacement u_r induced in the mode across the radial plane was analysed for the convergence study as shown in Figure 126. A maximum displacement of 0.215 mm was observed when the number of elements were 306632. However, this configuration was computationally expensive and would result in longer simulation times. In order to improve the efficiency of the solver time and still achieve accuracy, the mesh was refined in the brachial artery region as shown in Figure. Using this configuration, the maximum displacement u_r in the soft tissue is 0.21 which is within 5% of the previous configuration with a large number of elements. The convergence trend with respect to the number of elements can be seen in Figure 126. The element size used to mesh the brachial artery was 0.5 mm. The element size used to mesh the muscle layer, and the SAT layer was 2 mm, as illustrated in Figure 127. This mesh configuration resulted in a total of 145965 elements.

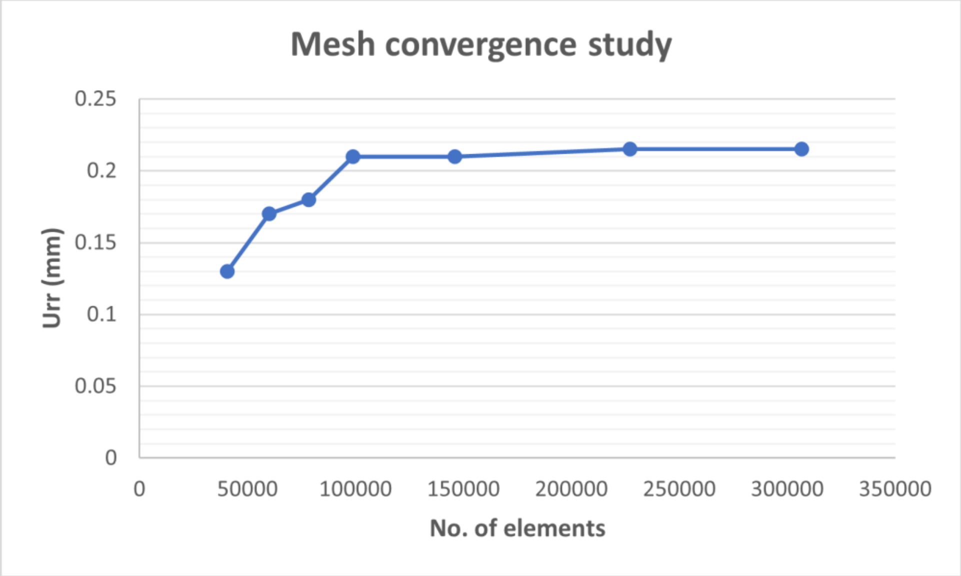

Figure 126 Mesh convergence study for anatomical model

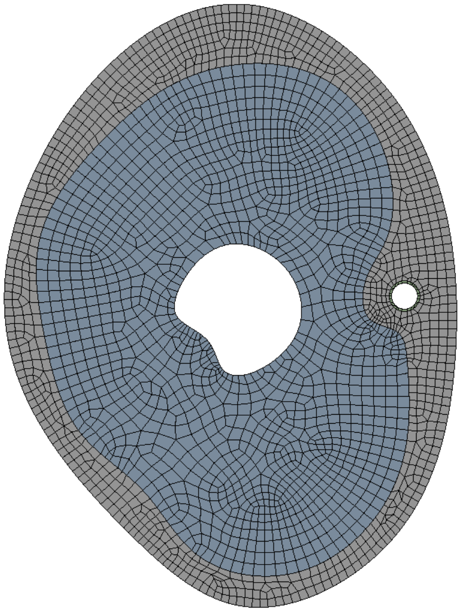

Figure 127 Meshed anatomical model

7.4 Results and analysis

The anatomical model was validated against the fabricated upper arm phantom. The model was simulated for the same pressure loads as the experiment (refer to Section 6.4). The TP was kept constant $30\ mmHg$. The contact status between the SAT and muscle layer was kept bonded. The volume changes in the brachial artery and soft tissue were compared with the results of the experiment. The comparison is shown in Table 8.

BP – CP (mmHg)	TP (mmHg)	Brachial artery volume change (mL)		Soft tissue volume change (mL)	
		Experiment	Simulation	Experiment	Simulation
10 – 40	30	0.10	0.161	0.3	0.522
20 – 50	30	0.20	0.246	1.2	1.764
30 – 60	30	0.35	0.313	2.2	2.921
40 – 70	30	0.45	0.427	3.2	3.772
50 – 80	30	0.55	0.498	4.2	4.510

Table 8 Volume changes: Experiment vs Simulation

The results from Table 8 are graphically illustrated in Figure 128 and Figure 129.

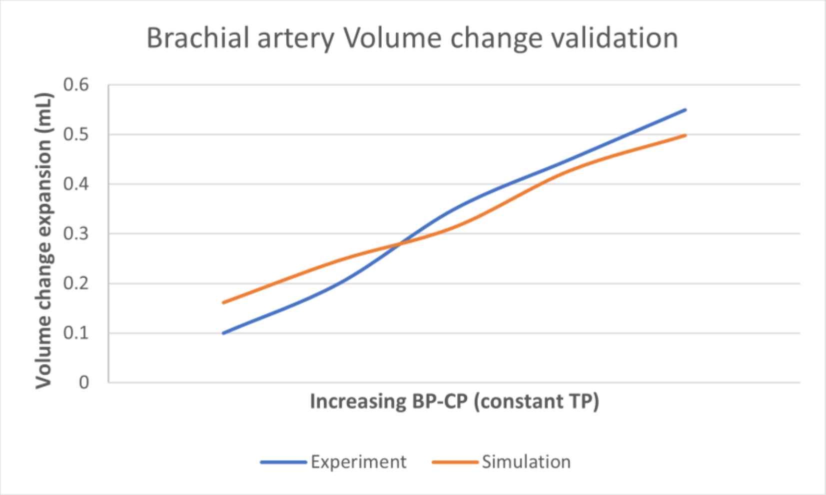

Figure 128 Brachial artery volume change. Experiment vs Simulation

It can be inferred from the Figure 128 that the trend of volumetric expansion in simulation is similar to experimental results. The difference between the magnitude of volume change ranges from 10% to 40%. In the experimental testing, it is observed that the artery expands more than the simulation tests. It is likely that the boundary conditions in the simulation and the experiment do not match. The presence of other anomalies like air entrapments, pressure losses can lead potentially lead to inaccurate results. However, the volume changes in the simulation are not significantly different from the test results.

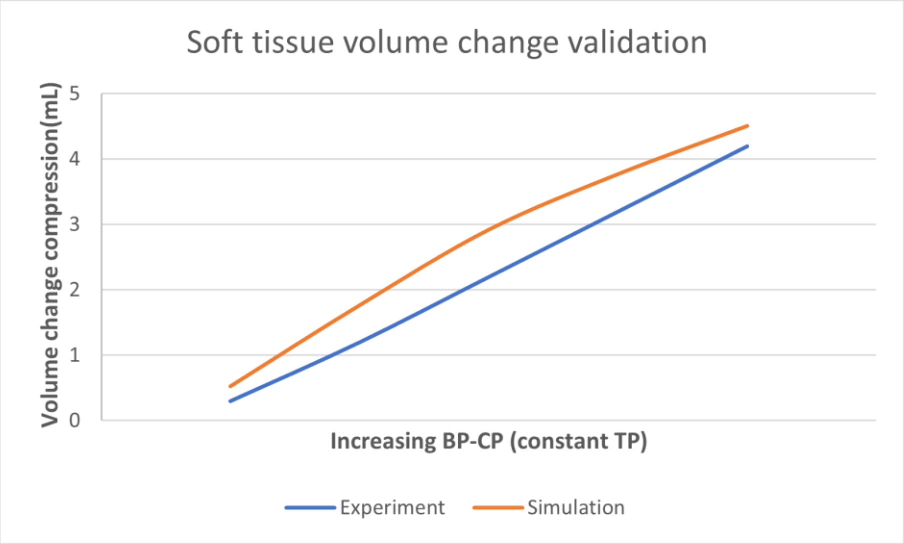

Figure 129 Soft tissue volume change. Experiment vs Simulation.

The soft tissue experiences volume changes due to compression. From Figure 129, it can be inferred that the soft tissue volume change is linear with increasing pressure, similar to the simulation results. The volume changes between the experimental and simulation results do not vary significantly and show a similar compression trend. The errors in the experiment are likely to cause this difference.

The phantom test-rig requires refinement but, the experimental outcomes do not vary significantly to reject the validation of the model. The anatomical model is further analysed for displacements, stress and strains with bonded and sliding contact conditions between SAT and muscle layers.

Keeping the TP constant, the anatomical model was simulated using pressures loading as used above (BP ranging from 10 – 50 mmHg, CP ranging from 40 to 80 mmHg). The results found in the bonded and sliding contact conditions are compared and discussed.

1) The maximum displacement Urr in the radial plane is shown in Figure 130. Evidently, the displacements induced in the upper arm are much higher in magnitude when a sliding contact is assumed between the SAT and muscle layers. Moreover, as the pressure increases, the displacements increase linearly for the case where the contact is assumed to be bonded. The location of the maximum displacements induced in the upper arm with bonded sliding contact is shown in Figure 131.

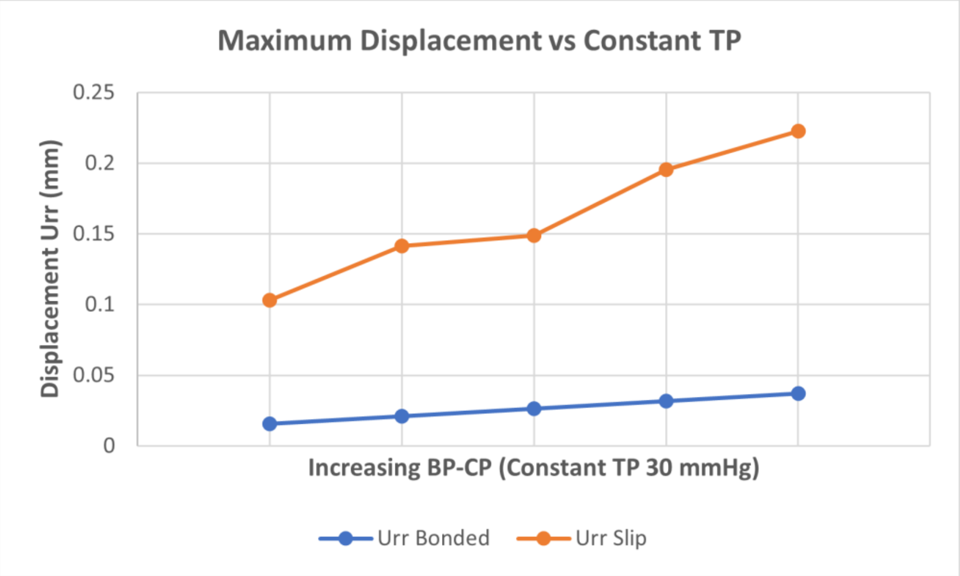

Figure 130 Maximum displacement (Urr) vs Pressure comparison

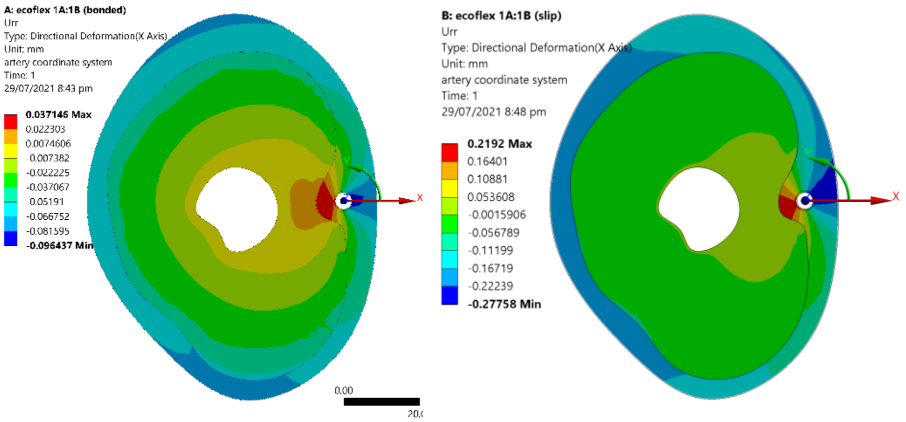

Figure 131 2D displacement (Urr) field plots for bonded and sliding contact conditions. (CP = 80 mmHg, BP = 50 mmHg)

From Figure 131, it is evident that the distribution of displacements varies significantly between the two contact conditions. In the sliding contact condition, the displacement is distributed around the brachial artery and the SAT layer. In the bonded contact condition, the displacements propagate towards the muscle layer because the magnitude of displacement around the brachial artery reduces significantly during BP measurement. The uneven distribution of displacements in these conditions suggests that the artery does not experience the same amount of compression, and thus, the strain and stress fields are likely to vary.

2) The maximum strain (Err) for the given pressure ranges is shown in Figure 132. The strain in the radial plane exhibits a similar distribution as the displacements. Strains of higher magnitude are induced in the sliding contact condition than the bonded. A non-linear distribution along the pressure ranges can be seen from Figure 129 instead of a linear trend in the bonded condition. The 2D strain field plots are illustrated in Figure 133.

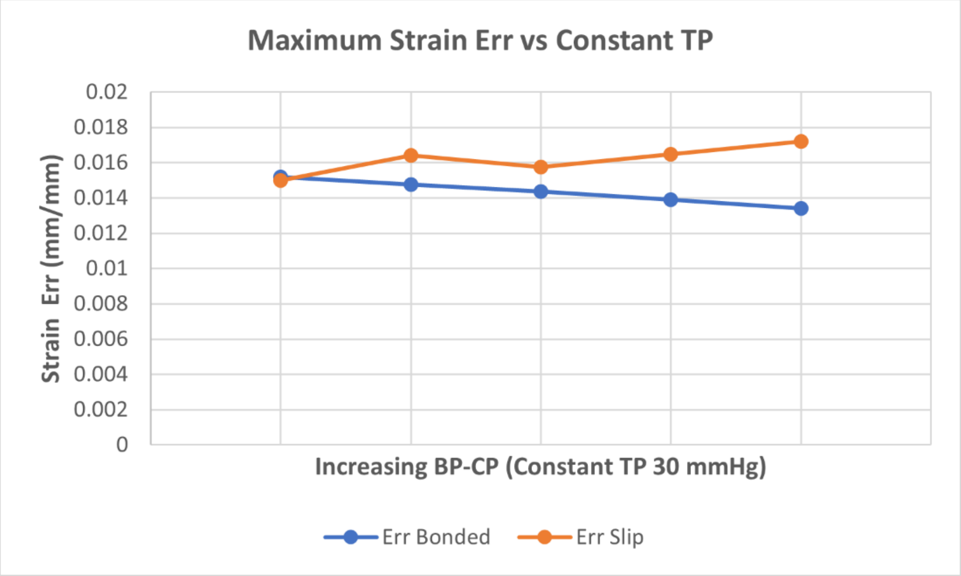

Figure 132 Maximum strain (Err) vs Pressure comparison

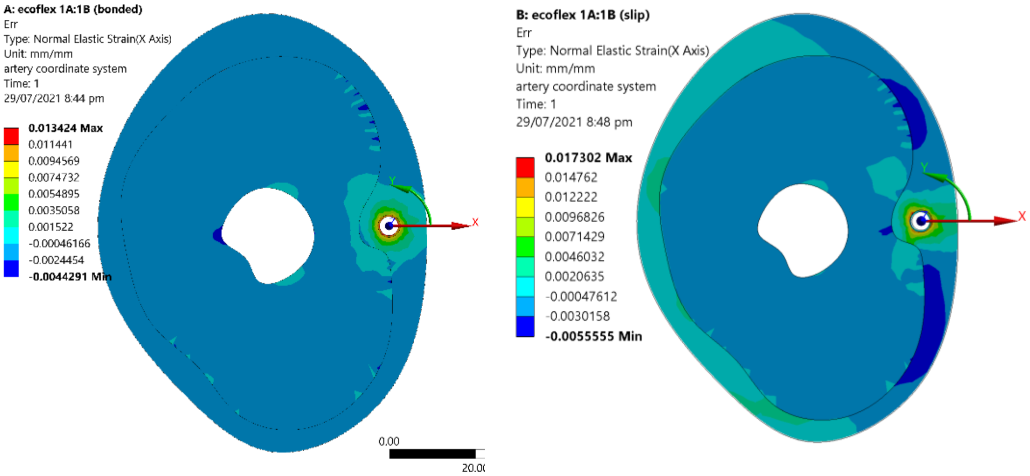

Figure 133 2D strain (Err) field plots for bonded and sliding contact conditions. (CP = 80 mmHg, BP = 50 mmHg)

It is evident from Figure 133 that the strain distributions vary greatly for the same pressure loads upon changing the contact condition between the soft tissue layers. In sliding contact conditions, strains are induced at different regions along the cross-section of the upper arm. In contrast, the strains in the bonded contact condition are concentrated around the brachial artery.

3) The maximum stress (Trr) in the radial plane for the given pressure ranges for sliding and bonded contact conditions is illustrated in Figure 134.

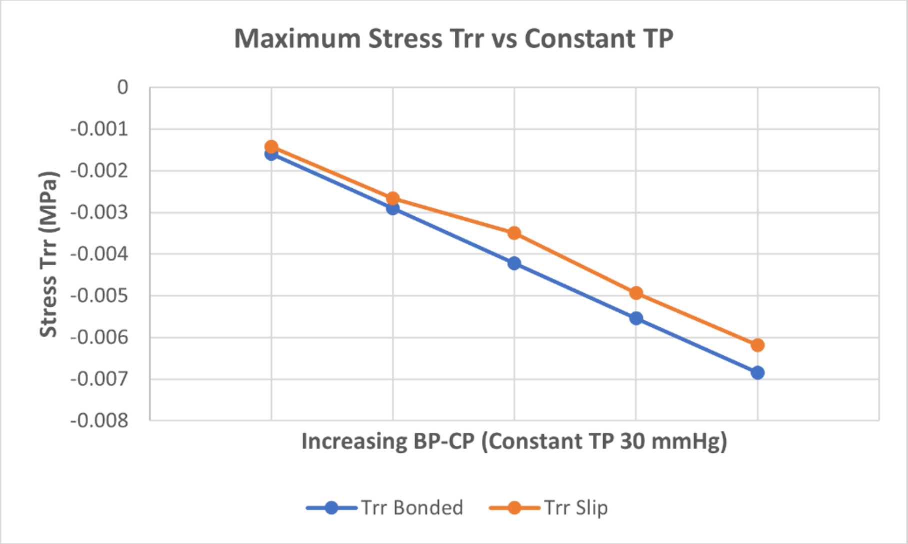

Figure 134 Maximum stress (Trr) vs Pressure comparison.

The maximum stress in the radial plane (Trr) induced in the soft tissue for the given conditions shows a similar trend. The negative magnitude of the stress suggests compression of the soft tissue for given pressure loads. In the sliding contact condition, the compressive stresses induced in the soft tissue are lower, suggesting that the forces are not conserved to produce the same magnitude in bonded contact. The 2D stress field plots in a radial plane are illustrated in Figure 135.

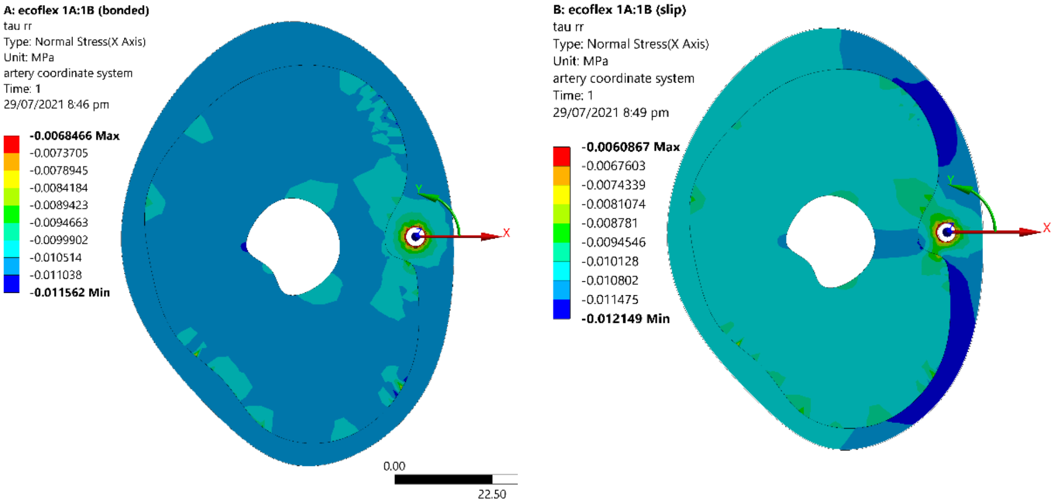

Figure 135 2D stress (Trr) field plots for bonded and sliding contact conditions. (CP = 80 mmHg, BP = 50 mmHg)

It is evident from Figure 135 that the distribution of stress varies significantly between these contact conditions. In the sliding contact condition, the CP is distributed to move the SAT layer. In contrast, the stress distribution in the bonded contact condition is more uniform than the bonded contact condition. This suggests that CP is not evenly distributed during the NIBP measurement process

4) The strain energy distribution for the simulated contact conditions over a range of given pressures is illustrated in the Figure 136.

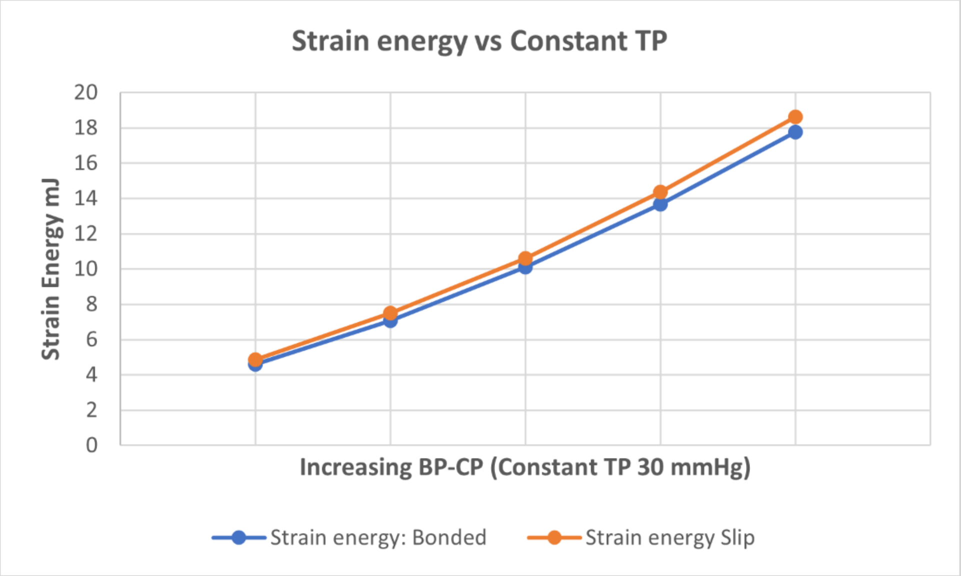

Figure 136 Strain energy vs CP-BP at constant TP = 80 mmHg

The distribution of strain energy in both contact conditions is similar. The magnitude of the strain energy between the given contact conditions differs by 4.6% for the given element mesh size. It can be inferred from this result that the energy is conserved as opposed to the forces that are transferred in the sliding contact. Thus, the strain energy remains unaffected by the change of contact condition between the soft tissue layers.

7.5 Summary

The anatomical model was validated with the fabricated upper arm phantom using pressure-volume change relationship at a constant TP of $30\ mmHg$. The pressure losses and potentially incorrect boundary conditions in the test rig did not allow the investigation of the pressure-volume relationship in detail for the project's timeline. However, some results obtained from the experiments and simulations were within 12% accuracy. The anatomical FE model was solved for sliding and bonded contact conditions between the SAT and muscle layers. It was observed that the displacements and strains vary significantly between the two contact conditions for a given range of pressures. However, the strain energy was found to match both cases, suggesting that it remains conserved irrespective of the change in contact conditions.

Chapter 8 Conclusion and Future scope

8.1 Conclusion

This study aimed to investigate the deformations, stresses, strains, volume changes in the soft tissue of the upper arm during NIBP measurement. The investigation was achieved by formulating analytical models, finite element models, and experimental investigation on a fabricated anatomical arm phantom. The study of these simulations and experiments found that the material properties, geometry, and tissue contact conditions of the upper arm play a vital role in determining the BP using NIBP measurement devices.

8.1.1 Material properties

The simple concentric upper arm models were simulated to investigate the BP simulation with linear and non-linear material models. The linear models were defined by Poisson’s ratio and Young’s modulus. The non-linear material models were formulated using a hyperelastic constitutive model derived from the tested material's stress-strain relationship. The linear and non-linear analyses of the concentric models led to the following outcomes:

1. The distribution and magnitudes of displacements, stresses, and strains vary significantly as the material model is changed from linear isotropic to hyperelastic in the same geometry. The variance occurs due to a change in the mechanical properties of the material.

2. It was inferred that the brachial artery and soft tissue volume changes are significantly affected due to the Poisson’s ratio of the soft tissue. The linear isotropic material allows the material to be compressible, whereas the hyperelastic material is nearly incompressible. The obtained strain energy distribution is significantly different for these material models. The NIBP measurement devices make gross assumptions about the compressibility of the soft tissues, which contributes to errors in the accurate estimation of BP.

8.1.2 Geometry and tissue contact conditions

The anatomical model was validated and simulated for a range of pressure keeping the TP constant. A 3 parameter Mooney-Rivlin constitutive model was formulated to simulate the FE model. The tissue contact condition between the SAT and muscle layers was frictionless to simulate the physiological phenomenon. The comparison of the models with bonded and sliding contact conditions led to the following outcomes:

1. The displacements and strains in the soft tissue vary significantly between the models with bonded and sliding contact conditions. The displacements and strains in the sliding contact condition are concentrated in the region of the brachial artery. In a model with bonded contact, the displacements rising from BP and CP propagates to the muscle layer, which decreases the displacements and stresses exerted on the artery.

2. In the anatomical model, it is observed that the cuff pressure is not exerted uniformly across the soft tissue. Moreover, in the sliding contact model, the cuff pressure exerted on the brachial artery is significantly lower. Thus, the estimation of BP assuming uniform cuff pressure around the upper arm leads to errors.

3. Although the displacements, strains vary greatly, the same magnitude and distribution of strain energy were obtained in these models. The strain energy is conserved irrespective of the contact conditions and pressure loads. Accounting strain energy as one of the factors of BP estimation could potentially improve the accuracy of these devices.

8.2 Future scope

The following areas could be improved from this study:

8.2.1 Material testing

In this study, the hyperelastic material models were formulated using the uniaxial stress-strain relationship. Although it was sufficient to model the expected stresses and strains, a complete characterisation using the biaxial and planar tests is likely to improve the stability of the material model when solving for an FEA.

The compression and tensile tests were conducted separately, which led to undesirable spikes in the data at smaller working strains. A uniaxial test that induces compression and tension on the specimen in the same loading cycle is desirable.

8.2.2 Phantom test rig

The design of the fabricated phantom test rig worked well, but it is sensitive to air entrapments that are likely to arise from the joineries. A robust phantom test rig that is not sensitive to air entrapments is likely to give reproducible and repeatable results for a range of transmural pressures without inducing air entrapments in the chamber. The boundary conditions to match the simulation were challenging to implement. A phantom test rig that emulates the ideal boundary conditions is likely to give accurate volume changes.

REFERENCES

37:2017, I. (2017). Rubber, vulcanized or thermoplastic — Determination of tensile stress-strain properties. (6), 30.

7743:2017, B. I. (2017). Rubber, vulcanized or thermoplastic — Determination of compression stress-strain properties.

Al-Jumaily, A. M., Lan H Fau - Stergiopulos, N., & Stergiopulos, N. (2013). Brachial artery waveforms for automatic blood pressure measurement. (1873-2380 (Electronic)).

Anderson-Jackson, L. D. (2016). *Development of an Arm Phantom for Testing Non-Invasive Blood Pressure Monitors* https://ui.adsabs.harvard.edu/abs/2016MsT.........30A

Blank, S. G., James, G. D., & Roman, M. J. (2018). Wideband External Pulse Recorded During Cuff Blood Pressure Measurement: A New Technique for Cardiovascular Assessment. (1179-1985 (Electronic)).

Bonso, E., Saladini, F., Zanier, A., Benetti, E., Dorigatti, F., & Palatini, P. (2010, 11/01). Accuracy of a single rigid conical cuff with standard-size bladder coupled to an automatic oscillometric device over a wide range of arm circumferences. *Hypertension research : official journal of the Japanese Society of Hypertension, 33*, 1186-1191. https://doi.org/10.1038/hr.2010.146

Brunette, J., Mongrain, R., Ranga, A., & Tardif, J.-C. (2004). An atherosclerotic coronary artery phantom for particle image velocimetry. *Proceedings of the Canadian Engineering Education Association (CEEA)*.

Cao, P., Duhamel, Y., Olympe, G., Ramond, B., & Langevin, F. (2013). A new production method of elastic silicone carotid phantom based on MRI acquisition using rapid prototyping technique. *Annu Int Conf IEEE Eng Med Biol Soc, 2013*, 5331-5334. https://doi.org/10.1109/embc.2013.6610753

Castleman, K. R. (1979). *Digital image processing / Kenneth R. Castleman*. Prentice-Hall.

Charalambos Vlachopoulos, Michael O'Rourke, & Nichols, W. W. (2012). *McDonald's Blood Flow in Arteries*

Theoretical, Experimental and Clinical Principles. CRC Press. https://doi.org/https://doi.org/10.1201/b13568

Chen, R. K., & Shih, A. J. (2013). Multi-modality gellan gum-based tissue-mimicking phantom with targeted mechanical, electrical, and thermal properties. (1361-6560 (Electronic)).

Chen, S., Fatemi M Fau - Greenleaf, J. F., & Greenleaf, J. F. (2004). Quantifying elasticity and viscosity from measurement of shear wave speed dispersion. (0001-4966 (Print)).

Chikkaveeraiah, B. V., Liu, H., Mani, V., Papadimitrakopoulos, F., & Rusling, J. F. (2009). A microfluidic electrochemical device for high sensitivity biosensing: detection of nanomolar hydrogen peroxide. *Electrochemistry communications, 11*(4), 819-822. https://doi.org/10.1016/j.elecom.2009.02.002

Ciszkiewicz, A., & Milewski, G. (2019). Structural and Material Optimization for Automatic Synthesis of Spine-Segment Mechanisms for Humanoid Robots with Custom Stiffness Profiles. *Materials (Basel, Switzerland), 12*(12), 1982. https://doi.org/10.3390/ma12121982

Cristalli, C., Mancini, P., & Ursino, M. (1992, 29 Oct.-1 Nov. 1992). An experimental and mathematical study of non-invasive blood pressure measurement. 1992 14th Annual International Conference of the IEEE Engineering in Medicine and Biology Society,

Dąbrowska, A. K., Rotaru, G.-M., Derler, S., Spano, F., Camenzind, M., Annaheim, S., Stämpfli, R., Schmid, M., & Rossi, R. M. (2016). Materials used to simulate physical properties of human skin. *Skin Research and Technology, 22*(1), 3-14. https://doi.org/https://doi.org/10.1111/srt.12235

Dammers, R., Tordoir Jh Fau - Kooman, J. P., Kooman Jp Fau - Welten, R. J. T. J., Welten Rj Fau - Hameleers, J. M. M., Hameleers Jm Fau - Kitslaar, P. J. E. H. M., Kitslaar Pj Fau - Hoeks, A. P. G., & Hoeks, A. P. (2015). The effect of flow changes on the arterial system proximal to an arteriovenous fistula for hemodialysis. (0301-5629 (Print)).

Deng, Z., & Liang, F. (2016, 2016/10/01). Numerical analysis of stress distribution in the upper arm tissues under an inflatable cuff: Implications for noninvasive blood pressure measurement. *Acta Mechanica Sinica, 32*(5), 959-969. https://doi.org/10.1007/s10409-016-0587-x

Douglas Mann, D. Z., Peter Libby, Robert Bonow. (2014). *Braunwald's Heart Disease: A Textbook of Cardiovascular Medicine* (10th ed.). Elsevier.

Drzewiecki, G., & Pilla, J. J. (1998, 1998/11/01). Noninvasive Measurement of the Human Brachial Artery Pressure–Area Relation in Collapse and Hypertension. *Annals of Biomedical Engineering, 26*(6), 965-974. https://doi.org/10.1114/1.130

Dwek, J. R. (2010). The periosteum: what is it, where is it, and what mimics it in its absence? *Skeletal radiology, 39*(4), 319-323. https://doi.org/10.1007/s00256-009-0849-9

Fernandez, J. W., Mithraratne P Fau - Thrupp, S. F., Thrupp Sf Fau - Tawhai, M. H., Tawhai Mh Fau - Hunter, P. J., & Hunter, P. J. (2004). Anatomically based geometric modelling of the musculo-skeletal system and other organs. (1617-7959 (Print)).

Frech, T. M., Penrod J Fau - Battistone, M. J., Battistone Mj Fau - Sawitzke, A. D., Sawitzke Ad Fau - Stults, B. M., & Stults, B. M. (2012). The prevalence and clinical correlates of an auscultatory gap in systemic sclerosis patients. (1687-9279 (Electronic)).

Fung, Y. C. (1993). *Biomechanics: Mechanical Properties of Living Tissues*. Springer-Verlag.

Gateno, J., Teichgraeber Jf Fau - Xia, J. J., & Xia, J. J. (2003). Three-dimensional surgical planning for maxillary and midface distraction osteogenesis. (1049-2275 (Print)).

Geoghegan, P. H., Buchmann, N. A., Spence, C. J. T., Moore, S., & Jermy, M. (2012, 2012/05/01). Fabrication of rigid and flexible refractive-index-matched flow phantoms for flow visualisation and optical flow measurements. *Experiments in Fluids, 52*(5), 1331-1347. https://doi.org/10.1007/s00348-011-1258-0

Gründemann, H. (1985). Ogden, R. W., Non-Linear Elastic Deformations. Ellis Horwood Ltd. 1984. Chichester, Distributors: John Wiley & Sons Ltd., XV, 532 S., £ 35.00. ISBN 0-85 312-273-3. *ZAMM - Journal of Applied Mathematics and Mechanics / Zeitschrift für Angewandte Mathematik und Mechanik, 65*(9), 404-404. https://doi.org/https://doi.org/10.1002/zamm.19850650903

Hasgall, P., Neufeld, E., Gosselin, M.-C., Klingenböck, A., & Kuster, N. (2018, 01/01). ITIS Database for thermal and electromagnetic parameters of biological tissues, Version 4.0. *May 15th*.

Heagerty, A. M., Aalkjaer C Fau - Bund, S. J., Bund Sj Fau - Korsgaard, N., Korsgaard N Fau - Mulvany, M. J., & Mulvany, M. J. (1993). Small artery structure in hypertension. Dual processes of remodeling and growth. (0194-911X (Print)).

Henry Black, W. E. (2012). *Hypertension: a companion to Braunwald's* *heart disease: Elsevier Health Sciences* (2nd ed.). Elsevier.

Heo, S.-H., Kim, C., Kim, T. S., & Park, H. S. (2020, 06/01). Artificial Skin: Human-Palm-Inspired Artificial Skin Material Enhances Operational Functionality of Hand Manipulation (Adv. Funct. Mater. 25/2020). *Advanced Functional Materials, 30*. https://doi.org/10.1002/adfm.202070161

Hjelmstad, K. (1996). Fundamentals of Structural Mechanics.

Hoi, Y., Woodward, S. H., Kim, M., Taulbee, D. B., & Meng, H. (2006, Dec). Validation of CFD simulations of cerebral aneurysms with implication of geometric variations. *J Biomech Eng, 128*(6), 844-851. https://doi.org/10.1115/1.2354209

Ishijima, A., Doi, T., Sakurada, K., & Yanagida, T. (1991, 1991/07/01). Sub-piconewton force fluctuations of actomyosin in vitro. *Nature, 352*(6333), 301-306. https://doi.org/10.1038/352301a0

Johansson, T., Meier, P., & Blickhan, R. (2000, 2000/09/07/). A Finite-Element Model for the Mechanical Analysis of Skeletal Muscles. *Journal of Theoretical Biology, 206*(1), 131-149. https://doi.org/https://doi.org/10.1006/jtbi.2000.2109

Jones, D. W., Appel Lj Fau - Sheps, S. G., Sheps Sg Fau - Roccella, E. J., Roccella Ej Fau - Lenfant, C., & Lenfant, C. (2003). Measuring blood pressure accurately: new and persistent challenges. (0098-7484 (Print)).

Kamthai, S., & Magaraphan, R. (2015, 2015/05/22). Thermal and mechanical properties of polylactic acid (PLA) and bagasse carboxymethyl cellulose (CMCB) composite by adding isosorbide diesters. *AIP Conference Proceedings, 1664*(1), 060006. https://doi.org/10.1063/1.4918424

Kesteloot H Fau - Van Houte, O., & Van Houte, O. (1973). The epidemiology of arterial blood pressure. (0068-3027 (Print)).

Khurana. (2014). *Khurana, I. (2014). Textbook of human physiology for dental students: Elsevier*

Health Sciences.

Kiarashi, N., Nolte, A. C., Sturgeon, G. M., Segars, W. P., Ghate, S. V., Nolte, L. W., Samei, E., & Lo, J. Y. (2015). Development of realistic physical breast phantoms matched to virtual breast phantoms based on human subject data. (2473-4209 (Electronic)).

Kulkarni, N. V. (2007). *Clinical Anatomy for Students: Problem Solving Approach* (J. B. M. P. Limited, Ed.).

Lakhal, K., Ehrmann, S., & Boulain, T. (2018, 2018/04/01/). Noninvasive BP Monitoring in the Critically Ill: Time to Abandon the Arterial Catheter? *Chest, 153*(4), 1023-1039. https://doi.org/https://doi.org/10.1016/j.chest.2017.10.030

Lan, H. (2012). *An investigation into ambulatory blood pressure measurement* [Doctoral Thesis, Auckland University of Technology].

Lan, H., Al-Jumaily Am Fau - Lowe, A., Lowe A Fau - Hing, W., & Hing, W. (2011). Effect of tissue mechanical properties on cuff-based blood pressure measurements. (1873-4030 (Electronic)).

Levinson, S. F., Shinagawa M Fau - Sato, T., & Sato, T. (1995). Sonoelastic determination of human skeletal muscle elasticity. (0021-9290 (Print)).

Lewis, P. S., Chapman, N., Chowienczyk, P., Clark, C., Denver, E., Lacy, P., Martin, U., McManus, R., Neary, A., Sheppard, J., on behalf of the, B., & Irish Hypertension Society's Blood Pressure Measurement Working, P. (2019, 2019/05/01). Oscillometric measurement of blood pressure: a simplified explanation. A technical note on behalf of the British and Irish Hypertension Society. *Journal of Human Hypertension, 33*(5), 349-351. https://doi.org/10.1038/s41371-019-0196-9

Liechty, W. B., Kryscio, D. R., Slaughter, B. V., & Peppas, N. A. (2010). Polymers for drug delivery systems. *Annual review of chemical and biomolecular engineering, 1*, 149-173. https://doi.org/10.1146/annurev-chembioeng-073009-100847

Ma, S. P., & Zahalak, G. I. (1991). A distribution-moment model of energetics in skeletal muscle. (0021-9290 (Print)).

Marieb, E. N., & Keller, S. M. (2017). *Essentials of human anatomy & physiology*.

Maurel, W., Thalmann, D., Hoffmeyer, P., Beylot, P., Gingins, P., Kalra, P., & Thalmann, N. (2002). *A Biomechanical Musculoskeletal Model of Human Upper Limb for Dynamic Simulation*. https://doi.org/10.1109/SSBI.2002.1233995

Mendoza-Muñoz, I., González-Angeles, A., Siqueiros, M., & Montoya, M. (2017, 12/08). Biomechanical Principles Used in Finite Element Analysis for Proximal Humeral Fractures with Locking Plates. *Medical Science and Technology, 58*, 128-136. https://doi.org/10.12659/MST.907350

Messas, E., Pernot M Fau - Couade, M., & Couade, M. (2013). Arterial wall elasticity: state of the art and future prospects. (2211-5684 (Electronic)).

Mihai, L. A., Chin, L., Janmey, P. A., & Goriely, A. (2015). A comparison of hyperelastic constitutive models applicable to brain and fat tissues. (1742-5662 (Electronic)).

Mille, M., Griffin, K., Maass-Moreno, R., & Lee, C. (2020, 10/19). Fabrication of a pediatric torso phantom with multiple tissues represented using a dual nozzle thermoplastic 3D printer. *Journal of Applied Clinical Medical Physics, 21*. https://doi.org/10.1002/acm2.13064

Mooney, M. (1940). A Theory of Large Elastic Deformation. *Journal of Applied Physics, 11*(9), 582-592. https://doi.org/10.1063/1.1712836

Nayak, S. R., Krishnamurthy A Fau - Kumar, M., Kumar M Fau - Prabhu, L. V., Prabhu Lv Fau - Saralaya, V., Saralaya V Fau - Thomas, M. M., & Thomas, M. M. (2008). Four-headed biceps and triceps brachii muscles, with neurovascular variation. (1447-6959 (Print)).

Oudry, J., Bastard C Fau - Miette, V., Miette V Fau - Willinger, R., Willinger R Fau - Sandrin, L., & Sandrin, L. (2009). Copolymer-in-oil phantom materials for elastography. (1879-291X (Electronic)).

Pailler-Mattei, C., Bec S Fau - Zahouani, H., & Zahouani, H. (2008). In vivo measurements of the elastic mechanical properties of human skin by indentation tests. (1350-4533 (Print)).

Palatini, P., & Asmar, R. (2018, 07/01). Cuff challenges in blood pressure measurement. *The Journal of Clinical Hypertension, 20*, 1100-1103. https://doi.org/10.1111/jch.13301

Patil, D., Aravindan, S., Perumal, V., & Paruchuri, V. R. (2016). *Nano-structure Formation by Annealing Ultrathin Polystyrene Film*.

Pavan, T. Z., Madsen El Fau - Frank, G. R., Frank Gr Fau - Adilton O Carneiro, A., Adilton O Carneiro A Fau - Hall, T. J., & Hall, T. J. (2010). Nonlinear elastic behavior of phantom materials for elastography. (1361-6560 (Electronic)).

Pickering Tg Fau - Hall, J. E., Hall Je Fau - Appel, L. J., Appel Lj Fau - Falkner, B. E., Falkner Be Fau - Graves, J., Graves J Fau - Hill, M. N., Hill Mn Fau - Jones, D. W., Jones Dw Fau - Kurtz, T., Kurtz T Fau - Sheps, S. G., Sheps Sg Fau - Roccella, E. J., & Roccella, E. J. (2005). Recommendations for blood pressure measurement in humans and experimental animals: part 1: blood pressure measurement in humans: a statement for professionals from the Subcommittee of Professional and Public Education of the American Heart Association Council on High Blood Pressure Research. (1524-4539 (Electronic)).

Picone, D. S., Climie Re Fau - Ahuja, K. D. K., Ahuja Kd Fau - Keske, M. A., Keske Ma Fau - Sharman, J. E., & Sharman, J. E. (2015). Brachial-to-radial SBP amplification: implications of age and estimated central blood pressure from radial tonometry. (1473-5598 (Electronic)).

Picone, D. S., Schultz, M. G., Otahal, P., Aakhus, S., Al-Jumaily, A. M., Black, J. A., Bos, W. J., Chambers, J. B., Chen, C. H., Cheng, H. M., Cremer, A., Davies, J. E., Dwyer, N., Gould, B. A., Hughes, A. D., Lacy, P. S., Laugesen, E., Liang, F., Melamed, R., Muecke, S., Ohte, N., Okada, S., Omboni, S., Ott, C., Peng, X., Pereira, T., Pucci, G., Rajani, R., Roberts-Thomson, P., Rossen, N. B., Sueta, D., Sinha, M. D., Schmieder, R. E., Smulyan, H., Srikanth, V. K., Stewart, R., Stouffer, G. A., Takazawa, K., Wang, J., Westerhof, B. E., Weber, F., Weber, T., Williams, B., Yamada, H., Yamamoto, E., & Sharman, J. E. (2017). Accuracy of Cuff-Measured Blood Pressure: Systematic Reviews and Meta-Analyses. (1558-3597 (Electronic)).

Rahmoun, J., Naceur, H., Morvan, H., Drazetic, P., Fontaine, C., & Mazeran, P. E. (2020, 2020/12/01/). Experimental characterization and micromechanical modeling of the elastic response of the human humerus under bending impact. *Materials Science and Engineering: C, 117*, 111276. https://doi.org/https://doi.org/10.1016/j.msec.2020.111276

Reinertsen, I., & Collins, D. L. (2006). A realistic phantom for brain-shift simulations. (0094-2405 (Print)).

Robles, N. A.-O., Fici, F., & Grassi, G. (2019). J-shaped curve for cardiovascular mortality: systolic or diastolic blood pressure? (1724-6059 (Electronic)).

Sahu, N., Parija, B., & Panigrahi, S. (2009, 2009/04/01). Fundamental understanding and modeling of spin coating process: A review. *Indian Journal of Physics, 83*(4), 493-502. https://doi.org/10.1007/s12648-009-0009-z

Schmedlen, R. H., Masters Ks Fau - West, J. L., & West, J. L. (2002). Photocrosslinkable polyvinyl alcohol hydrogels that can be modified with cell adhesion peptides for use in tissue engineering. (0142-9612 (Print)).

Smith, R. F., Rutt, B. K., & Holdsworth, D. W. (1999, Oct). Anthropomorphic carotid bifurcation phantom for MRI applications. *J Magn Reson Imaging, 10*(4), 533-544. https://doi.org/10.1002/(sici)1522-2586(199910)10:4<533::aid-jmri6>3.0.co;2-z

Sotiropoulou, P. A., & Blanpain, C. (2012). Development and homeostasis of the skin epidermis. (1943-0264 (Electronic)).

Sparks, J. L., Vavalle, N. A., Kasting, K. E., Long, B., Tanaka, M. L., Sanger, P. A., Schnell, K., & Conner-Kerr, T. A. (2015, Feb). Use of silicone materials to simulate tissue biomechanics as related to deep tissue injury. *Adv Skin Wound Care, 28*(2), 59-68. https://doi.org/10.1097/01.ASW.0000460127.47415.6e

Spitzer, V. M., & Whitlock, D. G. (1998). The Visible Human Dataset: the anatomical platform for human simulation. (0003-276X (Print)).

Spross, C., Kaestle N Fau - Benninger, E., Benninger E Fau - Fornaro, J., Fornaro J Fau - Erhardt, J., Erhardt J Fau - Zdravkovic, V., Zdravkovic V Fau - Jost, B., & Jost, B. (2015). Deltoid Tuberosity Index: A Simple Radiographic Tool to Assess Local Bone Quality in Proximal Humerus Fractures. (1528-1132 (Electronic)).

Standring, S. (2015). *Gray's Anatomy*

41st Edition. Elsevier.

Subburaj, R. (2020). *Developing an arm phantom* Auckland University of Technology]. Auckland.

Surry, K. J., Austin Hj Fau - Fenster, A., Fenster A Fau - Peters, T. M., & Peters, T. M. (2004). Poly(vinyl alcohol) cryogel phantoms for use in ultrasound and MR imaging. (0031-9155 (Print)).

Sutera, S. P., Pierre Pr Fau - Zahalak, G. I., & Zahalak, G. I. (1989). Deduction of intrinsic mechanical properties of the erythrocyte membrane from observations of tank-treading in the rheoscope. (0006-355X (Print)).

Teaford, M. (2009, 07/01). A.D.A.M. Student Atlas of Anatomy by Todd R. Olson and Wojciech Pawlina. *Clinical Anatomy - CLIN ANATOM, 22*, 634-634. https://doi.org/10.1002/ca.20817

Teran, J., Sifakis, E., Ng-Thow-Hing, V., Lau, C., Fedkiw, R., & Blemker, S. (2005, 05/01). Creating and Simulating Skeletal Muscle from the Visible Human Data Set. *IEEE transactions on visualization and computer graphics, 11*, 317-328. https://doi.org/10.1109/TVCG.2005.42

Tözeren, A. (1985). Continuum rheology of muscle contraction and its application to cardiac contractility. *Biophysical journal, 47*(3), 303-309. https://doi.org/10.1016/S0006-3495(85)83920-5

Ursino, M., & Cristalli, C. (1995). Mathematical modeling of noninvasive blood pressure estimation techniques--Part I: Pressure transmission across the arm tissue. (0148-0731 (Print)).

Ursino, M., & Cristalli, C. (1996). A mathematical study of some biomechanical factors affecting the oscillometric blood pressure measurement. *IEEE Transactions on Biomedical Engineering, 43*(8), 761-778. https://doi.org/10.1109/10.508540

Van Montfrans, G. A. (2001). Oscillometric blood pressure measurement: progress and problems. (1359-5237 (Print)).

Vannah, W. M., & Childress, D. S. (1993). Modelling the mechanics of narrowly contained soft tissues: the effects of specification of Poisson's ratio. (0748-7711 (Print)).

Whelton Pk Fau - Carey, R. M., Carey Rm Fau - Aronow, W. S., Aronow Ws Fau - Casey, D. E., Jr., Casey De Jr Fau - Collins, K. J., Collins Kj Fau - Dennison Himmelfarb, C., Dennison Himmelfarb C Fau - DePalma, S. M., DePalma Sm Fau - Gidding, S., Gidding S Fau - Jamerson, K. A., Jamerson Ka Fau - Jones, D. W., Jones Dw Fau - MacLaughlin, E. J., MacLaughlin Ej Fau - Muntner, P., Muntner P Fau - Ovbiagele, B., Ovbiagele B Fau - Smith, S. C., Jr., Smith Sc Jr Fau - Spencer, C. C., Spencer Cc Fau - Stafford, R. S., Stafford Rs Fau - Taler, S. J., Taler Sj Fau - Thomas, R. J., Thomas Rj Fau - Williams, K. A., Sr., Williams Ka Sr Fau - Williamson, J. D., Williamson Jd Fau - Wright, J. T., Jr., & Wright, J. T., Jr. (2017). 2017 ACC/AHA/AAPA/ABC/ACPM/AGS/APhA/ASH/ASPC/NMA/PCNA Guideline for the Prevention, Detection, Evaluation, and Management of High Blood Pressure in Adults: Executive Summary: A Report of the American College of Cardiology/American Heart Association Task Force on Clinical Practice Guidelines. (1524-4563 (Electronic)).

Yazdi, S. G., Geoghegan, P. H., Docherty, P. D., Jermy, M., & Khanafer, A. (2018, 2018/11/01). A Review of Arterial Phantom Fabrication Methods for Flow Measurement Using PIV Techniques. *Ann Biomed Eng, 46*(11), 1697-1721. https://doi.org/10.1007/s10439-018-2085-8

Yip, R., Mongrain, R., Ranga, A., Brunette, J., & Cartier, R. (2011, 08/17). DEVELOPMENT OF ANATOMICALLY CORRECT MOCK-UPS OF THE AORTA FOR PIV INVESTIGATIONS. *Proceedings of the Canadian Engineering Education Association*. https://doi.org/10.24908/pceea.v0i0.3984

Závodszky, G. (2015). *Hemodynamic investigation of arteries using the lattice Boltzmann method*

Zhang, B., Dong, Q., Korman, C. E., Li, Z., & Zaghloul, M. E. (2013, 2013/01/22). Flexible packaging of solid-state integrated circuit chips with elastomeric microfluidics. *Scientific Reports, 3*(1), 1098. https://doi.org/10.1038/srep01098

Zygote. (2020). *Solid 3D CAD Models Collection*. https://www.zygote.com/cad-models

APPENDIX

MATLAB code for solving the non-linear annular model.

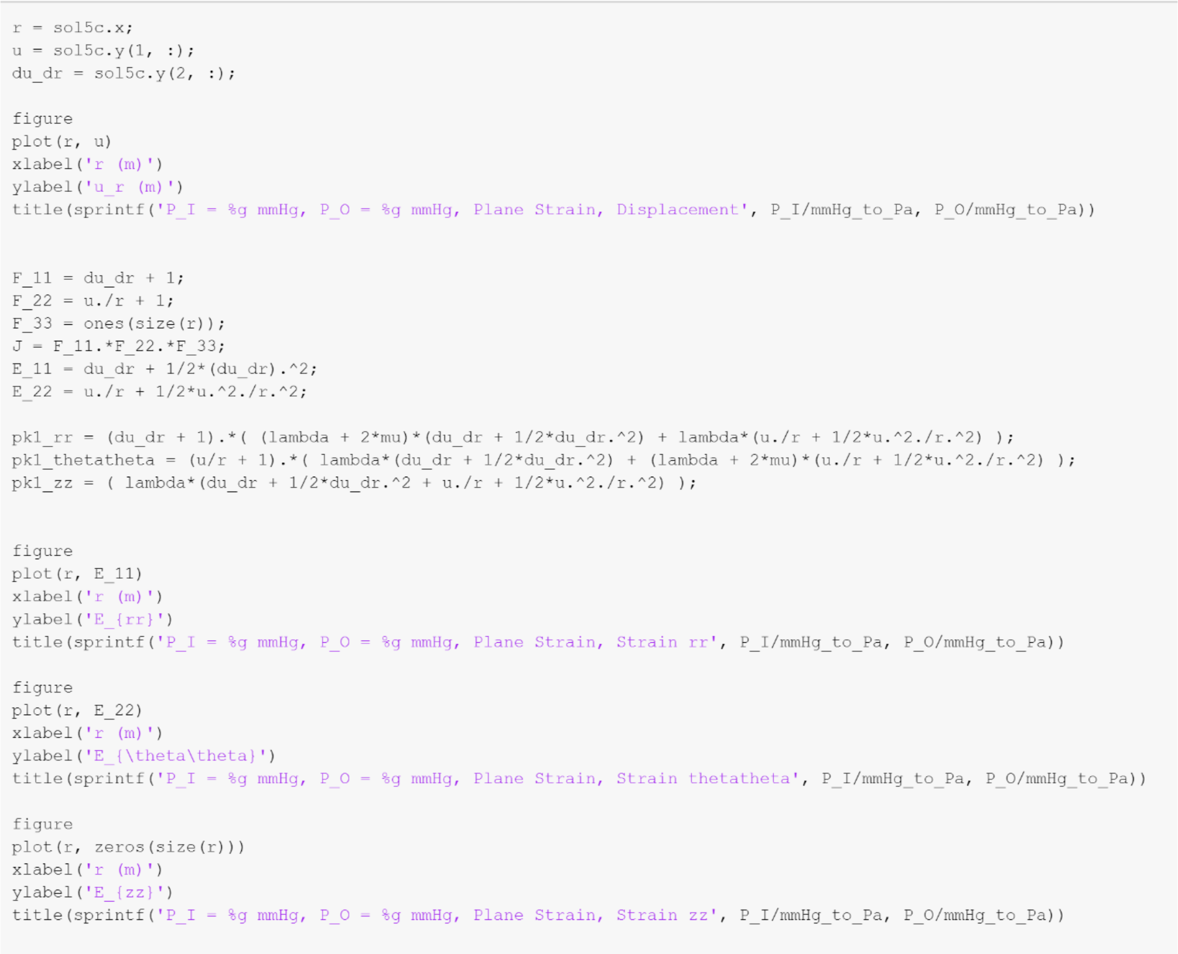

```
r = sol5c.x;
u = sol5c.y(1, :);
du_dr = sol5c.y(2, :);

figure
plot(r, u)
xlabel('r (m)')
ylabel('u_r (m)')
title(sprintf('P_I = %g mmHg, P_O = %g mmHg, Plane Strain, Displacement', P_I/mmHg_to_Pa, P_O/mmHg_to_Pa))


F_11 = du_dr + 1;
F_22 = u./r + 1;
F_33 = ones(size(r));
J = F_11.*F_22.*F_33;
E_11 = du_dr + 1/2*(du_dr).^2;
E_22 = u./r + 1/2*u.^2./r.^2;

pk1_rr = (du_dr + 1).*( (lambda + 2*mu)*(du_dr + 1/2*du_dr.^2) + lambda*(u./r + 1/2*u.^2./r.^2) );
pk1_thetatheta = (u/r + 1).*( lambda*(du_dr + 1/2*du_dr.^2) + (lambda + 2*mu)*(u./r + 1/2*u.^2./r.^2) );
pk1_zz = ( lambda*(du_dr + 1/2*du_dr.^2 + u./r + 1/2*u.^2./r.^2) );


figure
plot(r, E_11)
xlabel('r (m)')
ylabel('E_{rr}')
title(sprintf('P_I = %g mmHg, P_O = %g mmHg, Plane Strain, Strain rr', P_I/mmHg_to_Pa, P_O/mmHg_to_Pa))

figure
plot(r, E_22)
xlabel('r (m)')
ylabel('E_{\theta\theta}')
title(sprintf('P_I = %g mmHg, P_O = %g mmHg, Plane Strain, Strain thetatheta', P_I/mmHg_to_Pa, P_O/mmHg_to_Pa))

figure
plot(r, zeros(size(r)))
xlabel('r (m)')
ylabel('E_{zz}')
title(sprintf('P_I = %g mmHg, P_O = %g mmHg, Plane Strain, Strain zz', P_I/mmHg_to_Pa, P_O/mmHg_to_Pa))
```

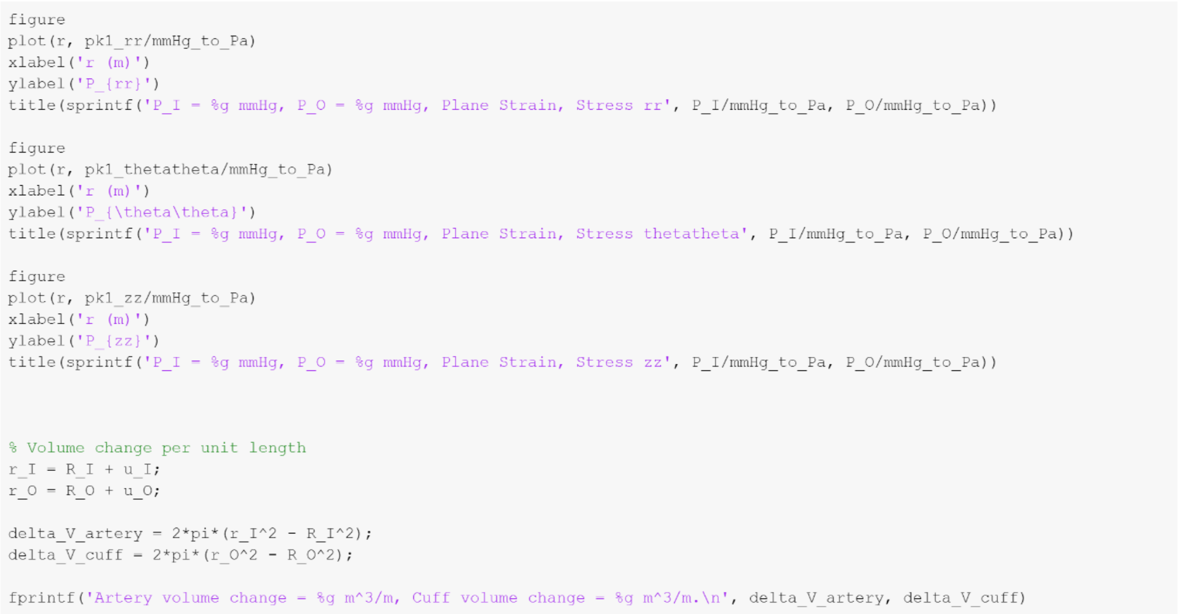

```
figure
plot(r, pk1_rr/mmHg_to_Pa)
xlabel('r (m)')
ylabel('P_{rr}')
title(sprintf('P_I = %g mmHg, P_O = %g mmHg, Plane Strain, Stress rr', P_I/mmHg_to_Pa, P_O/mmHg_to_Pa))

figure
plot(r, pk1_thetatheta/mmHg_to_Pa)
xlabel('r (m)')
ylabel('P_{\theta\theta}')
title(sprintf('P_I = %g mmHg, P_O = %g mmHg, Plane Strain, Stress thetatheta', P_I/mmHg_to_Pa, P_O/mmHg_to_Pa))

figure
plot(r, pk1_zz/mmHg_to_Pa)
xlabel('r (m)')
ylabel('P_{zz}')
title(sprintf('P_I = %g mmHg, P_O = %g mmHg, Plane Strain, Stress zz', P_I/mmHg_to_Pa, P_O/mmHg_to_Pa))



% Volume change per unit length
r_I = R_I + u_I;
r_O = R_O + u_O;

delta_V_artery = 2*pi*(r_I^2 - R_I^2);
delta_V_cuff = 2*pi*(r_O^2 - R_O^2);

fprintf('Artery volume change = %g m^3/m, Cuff volume change = %g m^3/m.\n', delta_V_artery, delta_V_cuff)
```